The Dissertation Committee for Alexander Stewart Hannah Certifies that this is the approved version of the following dissertation:

Optically-Triggered Nanodroplets for Enhanced Ultrasound and Photoacoustic Imaging

Committee:

Stanislav Emelianov, Supervisor

Laura Suggs

Andrew Dunn

Preston Wilson

Konstantin Sokolov

Kimberly Homan

Optically-Triggered Nanodroplets for Enhanced Ultrasound and Photoacoustic Imaging

by

Alexander Stewart Hannah, B.E., M.S.E.

Dissertation

Presented to the Faculty of the Graduate School of

The University of Texas at Austin

in Partial Fulfillment

of the Requirements

for the Degree of

Doctor of Philosophy

The University of Texas at Austin

May 2015

Dedication

To my family

For their unconditional support and guidance.

Acknowledgements

First, I would like to thank my family, for their unconditional support throughout my journey, and for their confidence in my ability to succeed at my goals. They put the difficult times in perspective, making me feel grateful for my education. They shared my passion for academic study and inquisitive nature. At no time have I felt uncomfortable asking them for help or advice; this emotional safety net gave me the perseverance to bring my graduate career to fruition.

I thank my supervisor, Stas Emelianov, for his unwillingness to accept mediocre work, and for casting off disbelief in my own ability to perform it. His knowledge, creative thinking, professionalism, communication skills, and affable personality are unmatched in the field, and I hope some of it rubbed off on me. Most importantly, he has had a fundamental impact on my approach to scientific problem solving, a skill which will impact my career and a tool I will carry with me forever.

My committee members, Dr. Andrew Dunn, Dr. Laura Suggs, Dr. Preston Wilson, Dr. Konstantin Sokolov, and Dr. Kimberly Homan showed genuine interest in my research, giving valuable feedback from multiple domains. Because they took time to listen to my work and engage in scientific discussion, my breadth and depth of knowledge of my project has improved, and I feel more capable of pursuing research and communicating my work.

The members of the Ultrasound Imaging & Therapeutics Laboratory were instrumental in my education as a PhD student. Each person in the group has a unique background and thus contributed to my progress in a different way. While a large group can be intimidating, their accessibility, experience, and benevolence were invaluable resources. I directly learned many essential lab skills from my colleagues, including

culturing cells, operating electrical equipment, mechanical machining of parts, and writing algorithms to efficiently analyze data. These lessons, which can't be learned from a textbook or in many classrooms, were a result of the generosity of my colleagues. I have never been surrounded by such a talented group of people, and if I picked up just a fraction of their knowledge, I have benefited greatly.

I especially want to thank Dr. Kimberly Homan, who, as a colleague, worked by my side and gave me hands-on feedback on my experiments. She taught me much about biochemistry, and her and organizational diligence has made me a better scientist.

Dr. Geoffrey Luke was also by my side during nearly all of my graduate career. He thinks creatively and logically, helping me to solve engineering puzzles and to think in a more efficient way. Nearly every discovery I made was thanks in part to his help in conducting experiments and analyzing the data we collected. He was a joy to work with.

My undergraduate research assistant, John Jacob, showed enthusiasm for clinical lab work that is driving his study to become a medical doctor. He was a great help with experiments, and he has a contagious sense of fervor in a sometimes monotonous laboratory environment.

Lastly, my friends and colleagues at UT have given me a feeling of solidarity that has fueled the fire of graduate work over the past half-decade. I have greatly enjoyed learning about their backgrounds, graduate work, and passions outside of school. I have developed relationships with them that will last a lifetime.

Optically-Triggered Nanodroplets for Enhanced Ultrasound and Photoacoustic Imaging

Alexander Stewart Hannah, Ph.D.

The University of Texas at Austin, 2015

Supervisor: Stanislav Y. Emelianov

Medical ultrasound imaging is ubiquitous in clinics due to its safety, low cost, portability, and imaging depth. The development of technologies to assist ultrasound in the diagnosis of diseases thus have a potentially broad clinical impact. More recently, photoacoustics has emerged as a complementary, high contrast modality for imaging optical absorption. Injectable dyes and nanoparticles locally amplify ultrasound and photoacoustic signal, helping to identify disease markers and track its progression. We have constructed a dual ultrasound and photoacoustic contrast agent that can be activated using an external optical trigger. In response to pulsed laser irradiation, the particle undergoes a liquid to gas phase change, or vaporization, which emits a strong acoustic wave and results in an echogenic microbubble, simultaneously enhancing contrast for both modalities. We designed and developed several iterations of particles, altering parameters to optimize biocompatibility, cost, and image contrast enhancement, and we then characterized key traits of the particles. Next, we imaged the contrast agents in phantom, *ex vivo*, and *in vivo* models to validate the image enhancement, developing image process algorithms to maximize image quality. These optically triggered contrast agents are a valuable tool for minimally invasive, highly specific, early identification of cancer.

Table of Contents

List of Tables

List of Figures

Chapter 1. Introduction

In 2014, it was estimated that 1.67 million new cases of cancer will have arisen, and approximately 590,000 people will have died from cancer in the same year[1]. The median age at diagnosis is 66, and age at death is 72. Unlike many diseases, the time between the onset of cancer and death can be short. We are still learning much about the behavior and progression of cancer, making it difficult to prevent and even more difficult to stop once it is at the stage where it can be found. One strategy to fight the disease is to identify the characteristics of cancer early, because in these stages several treatments can be applied with high rates of remission. Diagnosing cancer at an early stage is not an easy task. It requires in-depth knowledge of biology and physiology at the macro level of the human body as well as behavior at the cellular and molecular level, where the incipient stages of neoplasms begin.

Humans have engineered tools to better understand our surroundings and communicate it more effectively, enabling us to achieve an exponentially growing body of cumulative knowledge of the universe. When this engineering mindset intersects with problem solving in the medical domain, we are capable of extending our lives and living them at the highest quality. Medical diagnostics has improved through the engineering of tools that noninvasively investigate our bodies for information using sound, light, and magnetic fields. By developing techniques, instruments, and systems to gather information, we are constantly learning more about our own physiology, giving us answers we need to address problems that plague us profoundly. When applied to cancer diagnostics and therapy, development of these systems can alter our approach to treatment and improve quality of life.

For widespread implementation of a solution to cancer's mysterious and terrifying grip, we must employ diagnostic tools that are inexpensive and easy to use. By studying the work of those who developed these useful tools in the past and by exploring new avenues, we hope to mitigate the suffering and fear caused by this disease.

1.1 Medical Imaging

The goal of any biomedical imaging modality is to interrogate the body to study anatomy, tissue function, and more recently, biochemical and even molecular processes. Obtaining this information with safe, inexpensive technology allows us to more readily study the differences in anatomy and behavior between healthy and abnormal tissues. The identification of diseased tissue states at early stages markedly improves our ability to treat patients.

The principle of any imaging modality is to probe the body with some type of energy (the type of energy used typically distinguishes imaging systems) and then to analyze the energy which has either passed through or has reflected from its surface. The differences in the input and output energy allows us to gather information about the probed system (the body).

Medical imaging has a rich history of noninvasive diagnosis, beginning with William Roentgen's discovery of X-rays in 1895[2], followed by tomographic techniques developed by Vallebona and Hounsfield using the Radon Transform[3–5], and continuing with magnetic resonance imaging[6–10], nuclear imaging (PET and SPECT)[11,12], and ultrasound imaging[13], shown in Table 1. A variety of imaging modalities is researched and used clinically today; to say that one imaging modality is the "best" is naïve. Each modality has properties ideal for detecting certain diseases. However, each also has drawbacks such as high cost or adverse health effects that can outweigh its diagnostic value.

	First developed	Type of energy used	Pros	Cons
X-ray radiography	1895	Electromagnetic radiation (X-rays), $\lambda = 0.01 – 10$ nm	High resolution, high contrast for bones	Ionizing radiation, costly
X-ray computed tomography	1960s	Electromagnetic radiation (X-rays), $\lambda = 0.01 – 10$ nm	High resolution, high contrast for bones, full body imaging	Radiation exposure, costly, contrast agents
Magnetic resonance imaging	1937	Electromagnetic radiation (RF waves), $\lambda = 1\text{-}10$ m	Full body imaging, functional brain imaging, high resolution	Costly, not widely available, not real-time
Nuclear imaging	1950s	Ingested positron-emitting radionuclides	Functional information	Low resolution, requires ingesting agent
Ultrasound imaging	1949	Ultrasound waves (frequency = 20 kHz – 400 MHz)	High resolution, non-ionizing, inexpensive, portable, widely available, real-time	Poor contrast, difficult to interpret, speckle

Table 1.1: Medical imaging modalities

Several properties of ultrasound (US) imaging make it one of the most widely used imaging tools in clinics today:

- US is safe for repeated use[14–17]
- The operational cost of US is low
- US provides high resolution images of anatomy based on tissue impedance
- US imaging can occur in real time
- US commonly images 10 cm or deeper in the body
- The imaging system is portable

- US can measure blood flow and motion through the Doppler effect[18,19]
- Many applications of US imaging do not require exogenous contrast agents

These features of US imaging, particularly its clinical ubiquity, make it a good candidate for researching novel techniques that can identify diseases such as cancer at an early stage. Conversely, US imaging has several drawbacks:

- Endogenous US contrast, which is based on tissue density and sound speed, is often low[20–22], limiting it to visualization of gross anatomy
- US cannot provide whole body imaging
- Due to poor contrast and imaging artifacts, interpretation and diagnosis can be ambiguous

Because ultrasound imaging is inexpensive, safe, and thus so widely available, improving its current limitations could bring about an immediate and broad clinical impact.

1.2 Ultrasound Imaging Principles

As with any imaging technology, US requires the transmission of energy into a patient and the analysis of that energy after it interacts with the body. As its name suggests, the technique involves the transmission of ultrasound (frequency > 20 kHz) waves into the body. In response to an electrical impulse, a piezoelectric transducer vibrates rapidly, emitting ultrasound pressure waves. The transducer transmits a short US wave (typically ~2-3 wavelengths) into the body, where the wave propagates until it encounters a tissue boundary. A boundary, as it relates to US applications, is a spatial difference in acoustic impedance (Z), defined as

$$Z = \rho * c$$

where ρ is the density of the material (kg m^{-3}), and c is its speed of sound (m s^{-1}). After encountering a boundary, a portion of the sound wave is scattered orthogonal to the boundary surface (reflected), and the rest of the wave continues to travel through the material. The percentage of the sound wave which is backscattered depends on the difference in acoustic impedance between the two materials. A boundary with a greater difference in acoustic impedance will reflect a greater portion of the incident US waves. Most soft tissues are primarily composed of water and have similar values of Z. However, some tissues, such as bone, highly reflect US waves due to a vast difference in Z from the surrounding tissue. Likewise, any gas-filled regions, such as the lungs, highly reflect US waves. For this reason, US is practically unable to image through bone or lungs.

To form an image, a transducer emits a US wave at time t = 0, which propagates through the body. Then the transducer waits and "listens" for reflections—that is, waits to receive reflected pressure waves, which it can convert to electrical signals and eventually image data. The first acoustic impedance boundary—say at distance z from the transducer—reflects a portion of the incident US wave, and the reflected pressure wave arrives back at the transducer at time $t = 2c/z$, where c is the speed of sound in tissue, z is the depth of the reflecting boundary, and the 2 accounts for the round trip travel of the sound wave from the transducer to the boundary and back. Based on this time of flight equation, the US imaging system calculates the distance between the transducer face and that boundary, as well as the intensity of the reflection. A greater difference in Z will reflect a greater portion of US waves, and this is recorded as a higher intensity reflection. Meanwhile, the portion of the US wave that was not reflected continues to propagate through the tissue until it encounters another boundary. At this point, another portion of the wave is reflected, then received by the transducer, and this distance z is calculated. This process continues until all of the originally emitted US wave is absorbed by the tissue and

can no longer be detected by the transducer. This results in a one-dimensional vector of values called an A-line; each value in the vector represents a pressure level of the reflected wave at a given depth. High pressure levels indicate boundaries, or changes in Z, at that depth. Early iterations of US systems were only able to collect one-dimensional A-line data; to form an image, several A-lines were collected by mechanically scanning the transducer. This matrix of A-lines was converted into an image intensity brightness map called a B-mode image, which is the most common form of US image data seen today.

To speed up the process of acquiring and displaying full B-mode images, transducers are no longer mechanically scanned. Instead, typical US transducers comprise a linear array of either 64 or 128 small transducers, or elements, and grouped together into one probe used for imaging. Instead of mechanically scanning one transducer over the surface to form an image, each of the elements is controlled electronically, allowing for the rapid acquisition of many A-lines which can be used to display a B-mode image in real-time.

While a US image displays the acoustic impedance boundaries present in the tissue being probed, there is additional granular appearance called "speckle" in most biological US images. This signal is usually undesirable, because it decreases the overall contrast of the image, making diagnosis difficult. Ultrasound speckle is explained by the fact that biological tissue can be modeled as a collection of scatterers so numerous that there are many within one resolution cell of the scanner. The wavelets scattered by them interfere, and speckle is explained as an interference phenomenon[23]. Speckle is arguably the greatest drawback of US imaging, and many techniques are researched to overcome this limitation.

1.3 Ultrasound Contrast Agents

One of the most commonly cited limitations of US is its poor image contrast. Because US contrast relies on differences in acoustic impedance (Z), many biological tissues (which are mostly water based) are difficult to distinguish. Additionally, the previously mentioned speckle pattern from human tissue further reducing image contrast[20–22]. It is therefore desirable to improve the image contrast to help identify target organs or disease markers. Novel materials and constructs for contrast agents are heavily researched and highly valuable to the field of medical diagnostics and image-guided therapy.

Ultrasound contrast agents are injectable solutions of particles whose acoustic impedance Z is significantly different from the background. Because gas differs greatly in speed of sound and density from all tissues, tiny "microbubbles" are employed as contrast agents because they highly reflect US waves and appear as bright spots in an image. The first reported US contrast enhancement due to bubbles is documented in work by Gramiak and Shah in 1967[24]. Additionally, gas microbubbles may oscillate in size under a diagnostic US pressure field, and this nonlinear behavior can be used to distinguish them from background tissue in "harmonic imaging[25]." Unfortunately, due to surface tension (σ), unstabilized gas bubbles do not last longer than 1-2 seconds. Therefore, various modifications have been developed to stabilize bubbles for longer circulation time. Ferrara et al have reviewed the physics of various bubble formulations[26], explaining how various constituents may improve their stability. The pressure drop across a bubble interface (ΔP) is given by the Laplace equation:

$$\Delta P = P_b - P_a = \frac{2\sigma}{r} \tag{1.1}$$

where P_b is the pressure inside the bubble, P_a is the hydrostatic pressure outside the bubble,

σ is the surface tension of the bubble, and r is the bubble radius[26]. A free bubble in water, with a small enough radius, and with the surface tension of water/air interface will either a) coalesce with other microbubbles to form a gas bolus large enough to exist at a stable Laplace pressure, or b) dissolve into the surrounding liquid within a few seconds due to water's high surface tension and thus high Laplace pressure[26]. To form stable microbubbles, an encapsulating shell may be added to the solution, which serves two purposes. First, it can act as a physical barrier to the gas dissolving in the liquid, and second, it reduces the surface tension, allowing bubbles of a smaller size to exist at a stable Laplace Pressure. The bubble radius can be modeled by the Epstein-Plesset equation:

$$-\frac{dr}{dt} = \frac{L}{\frac{r}{D_w} + R_{shell}} \left(\frac{1 + \frac{2\sigma_{shell}}{P_a r} - f}{1 + 3\sigma_{shell}/4P_a r} \right) \tag{1.2}$$

where L is Ostwald coefficient, D_w is the gas diffusivity in water, R_{shell} is the resistance of the shell to gas permeation, σ_{shell} is the surface tension of the shell, and f is the ratio of the gas concentration in the bulk medium versus that at saturation[27,28]. The Ostwald coefficient describes the velocity with which a gas will leave or enter a bubble in solution, and thus has a substantial impact on bubble dissolution[29]. The lifetime of a free air bubble is less than 1 s, and the lifetime of a free perfluorocarbon bubble is less than 1 min (Fig. 1.1)[26].

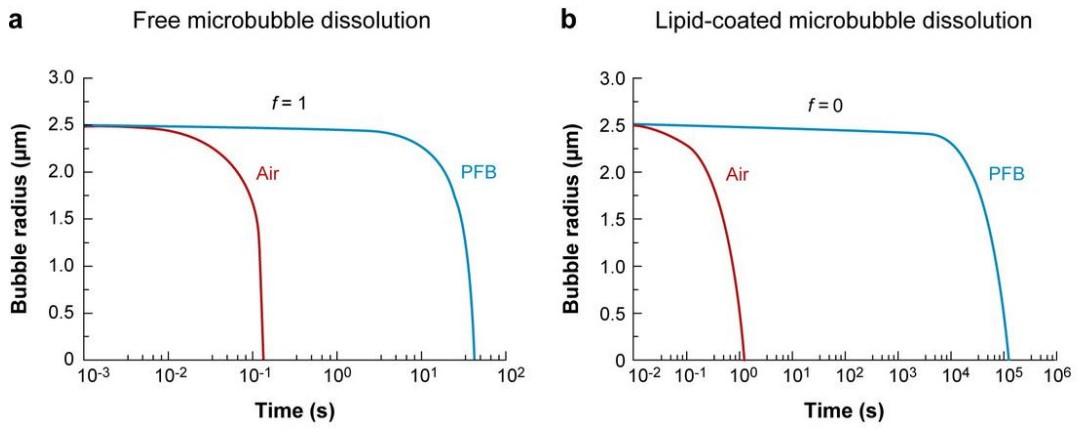

Figure 1.1: Calculated microbubble dissolution kinetics based on the modified-EP equation. (a) Radius-time curves of a free microbubble composed of air or perfluorobutane (PFB). Model parameters were σ_{shell} = 72 mN m^{-1}, R_{shell} = 0, Pa = 101.3 kPa, and f = 1 (i.e. saturation). Diffusion parameters for air were L = 0.02 and $D_w = 2 \times 10^{-5}$ cm^2 s^{-1}; those for PFB were L = 0.0002, $D_w = 0.7 \times 10^{-5}$ cm^2 s^{-1}. (b) Radius-time curves of lipid-coated microbubbles in degassed water (f = 0). Model parameters were the same as above, except $R_{shell} = 10^4$ s m^{-1} for air and 10^7 s m^{-1} for PFB and σ_{shell} = 0 mN m^{-1}. All curves were generated in MATLAB using a standard fourth-order Runga-Kutta algorithm.

Two methods have been commonly employed to increase bubble lifetime. The first is using higher molecular weight gases, which have a lower Ostwald coefficient, as shown in Table 1.2[30]. The use of perfluorocarbon (PFC) gas microbubbles as an alternative US contrast agent to air bubbles was first explored in 1984 by Mattrey et al in the imaging of myocardial infarction in dogs[31]. At the time, perfluorocarbon microbubbles were used not as an imaging agent, but as a blood substitute in anemic patients, due to the high solubility of oxygen in perfluorocarbon. It was soon realized that the lifetime of free PFC bubbles, however, was vastly improved over air bubbles, as shown by the 200x increase in lifetime (Fig. 1.1a). This has made PFC the gold standard for US contrast agents.

Another method to prevent bubble dissolution is the addition of a bubble shell, or

surfactant, to the solution. This reduces the surface tension by adsorption of an amphiphilic compound at the bubble surface. Various proteins, lipids, and polymer surfactants have been employed to improve lifetime, with profound effects (Fig. 1.1b). By adding a surfactant shell, a perfluorocarbon bubble is stabilized for several hours, rather than just a few seconds, as shown in Table 1.2[30].

	Ostwald coefficient ($x10^6$)	Disappearance time (s)
Air	23,168	0.02
Sulfur hexafluoride (SF_6)	5,950	0.1
Perfluoropropane (C_3F_8)	583	1.1
Perfluorohexane (C_6H_{14})	24	2

Table 1.2: Ostwald coefficient and disappearance time for 3 μm diameter bubbles containing different gases.

The next generation of US contrast agents reduced their diameter from several microns to hundreds of nanometers by synthesizing the particles in a liquid state, and then vaporizing them into high contrast gas bubbles using focused US energy[32–35]. This provided a few advantages over gas microbubbles. First, the circulation time of these "nanodroplets" is vastly improved over microbubbles because the liquid PFC does not diffuse from the core nearly as quickly as gaseous PFC does. Second, the small size of the nanodroplets enables them to perfuse tissue more effectively than micron sized bubbles, which are restricted to the vascular space. Specifically, nanodroplets can diffuse from tumor neovasculature via the enhanced permeability and retention (EPR) effect[36].

The liquid state of nanodroplets renders their acoustic impedance similar to the water-based tissue background, and they provide relatively little US image contrast. However, many researchers discovered that the liquid nanodroplets can be converted into gas microbubbles through triggered vaporization, or the transition of the liquid nanodroplet

into a microbubble in response to an external stimulus. The first case of triggered PFC droplet vaporization was reported by Apfel in 1998[37] and then studied by Kripfgans et al ten years later[35,38], where they used high intensity focused ultrasound (HIFU) to bring about local cyclic pressure changes in the environment around the droplets. The peak rarefactional (negative) pressure induced a liquid-to-gas phase change of the droplet, termed acoustic droplet vaporization (ADV). Triggered vaporization with HIFU confers a few advantages over simply using microbubbles. First, smaller liquid PFC droplets can be used as the contrast agent, which are more stable and perfuse tissue better than microbubbles. Second, the particles become echogenic precisely in response to a user-defined trigger, making them easy to locate using US imaging. When the droplet is externally triggered to vaporize, there is no ambiguity over whether bright spots are endogenous or due to the contrast agent. Lastly, the violent nature of the vaporization can bring about therapeutic effects.

1.4 Photoacoustic Imaging

Another imaging modality related to US imaging, termed photoacoustics (PA), uses light to induce detectable sound waves. The photoacoustic effect was first reported by Alexander Graham Bell in 1881[39], and it has been developed into an imaging technique within the past few decades, which has been thoroughly reviewed[40–47]. Photoacoustics uses pulsed laser irradiation to induce rapid thermal expansion of optical absorbers—either endogenous (melanin, hemoglobin and other porphyrins)[48] or injected—which emit broad frequency acoustic waves that are received by a US transducer to produce a high contrast image of optical absorption. Detecting optical absorption allows us to locate endogenous chromophores or injected contrast agents with high specificity. Photoacoustic signal can be produced through a number of different mechanisms, namely thermoelastic (thermal)

expansion[49,50], vaporization[51], photochemical processes[43,52], and optical breakdown[53]. While optical breakdown results in the most efficient pressure generation, it is not desirable due to its destructive nature[51]. Photochemical processes have been studied as well, but not for biomedical applications because of safety limitations[43,52]. More commonly, thermal expansion is utilized in biomedical applications. The spatial and temporal magnitude of a pressure wave that is produced is dictated by the photoacoustic wave equation[54],

$$\left(\nabla^2 - \frac{1}{v_s^2}\frac{\partial^2}{\partial t^2}\right)p = -\frac{\Gamma}{v_s^2}\frac{\partial H}{\partial t} \tag{1.3}$$

where p is pressure (Pa), v_s is the longitudinal wave speed in the medium (m s^{-1}), and Γ is the dimensionless Grüneisen coefficient,

$$\Gamma = \frac{\beta v_s^2}{C_p} \tag{1.4}$$

where β is the coefficient of thermoelastic expansion (K^{-1}) , and C_p is the heat capacity per unit mass at constant pressure (J g^{-1} K^{-1})). The left-hand side of the equation describes the wave propagation, and the right-hand side represents the source term. The heating function H is the thermal energy converted per unit volume and per unit time, and it is related to the optical power deposition. Here, time-invariant heating produces a pressure wave. Given a sufficiently short laser pulse, the chromophore absorbs all of the optical energy before any heat is lost, allowing the pressure to propagate according to Eqn. 1.3. Additionally, if the laser pulse is shorter than the stress relaxation time, all of the optical energy is absorbed before any pressure is propagated from the absorber. In this case, the PA pressure wave can be described by

$$p = \Gamma \mu_a F \tag{1.5}$$

where μ_a is the optical absorption coefficient (m^{-1}) and F is the local laser fluence (J m^{-2}).

Photoacoustic imaging systems can be integrated with existing US imaging systems, because PA imaging uses the same clinical array transducer to receive photoacoustic pressure waves. While US displays an image of acoustic impedance, PA techniques provide complementary information, namely a map of optical absorption. Anatomical information can be seen using US techniques—that is, large tissue boundaries. Photoacoustics gives information on the physiology of the underlying tissue, such as blood content and oxygenation. As with US imaging, many nanoparticle constructs have been developed to enhance PA image contrast, such as colored dyes and solutions of metal nanoparticles[55–61]. These contrast agents absorb light much more strongly than tissue chromophores, thereby emitting stronger PA waves and making them a tool for identifying tissues targeted by the particles[62–64].

To improve the signal to noise ratio and sensitivity of PA imaging, recent engineering approaches have been researched to generate PA signal from vaporization of contrast agents. It has been shown that the pressure wave from vaporization is upwards of an order of magnitude higher than the PA signal from thermal expansion, (Fig. 1.2)[43]. By combining the ability of a liquid PFC nanodroplet to vaporize with the US echogenicity of PFC microbubbles, a powerful dual US/PA contrast agent can be developed.

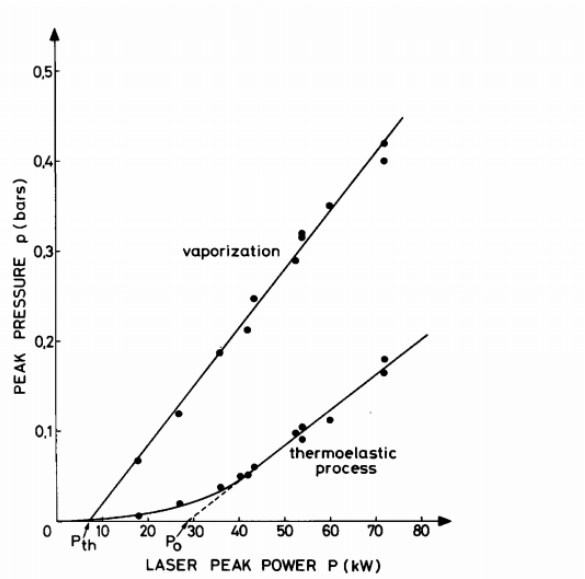

Figure 1.2: Peak pressure p in water as a function of the laser peak power P for the vaporization process and for the thermoelastic effect at a constant distance r from the impact.

The capabilities of PFC nanodroplets and PA contrast agents have recently been combined to form a new type of nanoparticle, named photoacoustic nanodroplets (PAnDs)[65,66]. These particles consist of a nano-sized (200-800 nm) liquid PFC droplet as described above, but they also incorporate an optical absorber into the PFC core or the surfactant shell. Upon pulsed laser irradiation, the region surrounding the optical absorber experiences both a temperature increase and a propagating pressure wave, causing a liquid-to-gas phase transition of the droplet and inducing a one-time, high amplitude PA signal due to bubble formation, termed optical droplet vaporization (ODV)[67]. This PA signal from vaporization is 2-10x higher than the PA signal from thermal expansion of the optical absorber by itself[65,66,68,69]. The resulting PFC bubble can provide US contrast either by acoustic impedance mismatch between the particle's gaseous core and the surrounding tissue or by utilizing the bubble resonance frequency[70,71]. Due to the relatively unexplored

nature of PAnDs, several properties may be tuned to optimize their US and PA contrast, as well as their stability, sensitivity, and targeting capabilities.

1.5 Research Goals

Photoacoustic nanodroplets are an emerging contrast agent with great potential for diagnostic imaging and therapeutic applications, but their formulations and imaging capabilities have just been explored in the last few years. The goal of this research project is 1) to expand the platform of photoacoustic nanodroplet contrast agents to include a variety of optical absorbers and perfluorocarbons, 2) to characterize the attributes and behavior of the droplets in US and PA imaging applications, and 3) to assess the improvement of their imaging qualities in an *in vivo* environment for cancer diagnostics.

1.6 References

1. Siegel, R., Naishadham, D. & Jemal, A. Cancer statistics, 2013. *CA. Cancer J. Clin.* **63,** 11–30 (2013).
2. Röntgen, W. C. On a New Kind of Rays. *Science* **3,** 227–231 (1896).
3. Hounsfield, G. N. Computerized transverse axial scanning (tomography): Part 1. Description of system. *Br. J. Radiol.,* **46**, 1016-1022 (1973).
4. Vallebona, A. & Maragliano, V. Radiography with great enlargement (microradiography) and a technical method for the radiographic dissociation of the shadow. *Radiology* **17,** 2 (1931).
5. Deans, S. R. *The Radon Transform and Some Of Its Applications*. Courier Dover Publications (2007).

6. Rabi, I. I. Space quantization in a gyrating magnetic field. *Phys. Rev.* **51,** 652–654 (1937).

7. Rabi, I. I., Millman, S., Kusch, P. & Zacharias, J. R. The molecular beam resonance method for measuring nuclear magnetic moments. The magnetic moments of Li63, Li73 and F199. *Phys. Rev.* **55,** 526–535 (1939).

8. Bloch, F. Nuclear induction. *Phys. Rev.* **70,** 460–474 (1946).

9. Carr, H. Y. & Purcell, E. M. Effects of diffusion on free precession in nuclear magnetic resonance experiments. *Phys. Rev.* **94,** 630–638 (1954).

10. Hahn, E. L. Spin echoes. *Phys. Rev.* **80,** 580–594 (1950).

11. Brownell, G. L. & Sweet, W. H. Localization of brain tumors with positron emitters. *Nucleonics* **11,** 40–45 (1953).

12. Phelps, M. E. *et al*. Application of annihilation coincidence detection to transaxial reconstruction tomography. *J. Nucl. Med. Off. Publ. Soc. Nucl. Med.* **16,** 210–224 (1975).

13. Newman, P. G. & Rozycki, G. S. The history of ultrasound. *Surg. Clin. North Am.* **78,** 179–195 (1998).

14. Miller, D. L. *et al.* Bioeffects considerations for diagnostic ultrasound contrast agents. *J. Ultrasound Med.* **27,** 611–632 (2008).

15. Barnett, S. B. *et al.* International recommendations and guidelines for the safe use of diagnostic ultrasound in medicine. *Ultrasound Med. Biol.* **26,** 355–366 (2000).

16. Church, C. C. Spontaneous homogeneous nucleation, inertial cavitation and the safety of diagnostic ultrasound. *Ultrasound Med. Biol.* **28,** 1349–1364 (2002).

17. Szabo, T. L. *Diagnostic Ultrasound Imaging: Inside Out*. Academic Press (2004).

18. Aaslid, R., Markwalder, T.-M. & Nornes, H. Noninvasive transcranial Doppler ultrasound recording of flow velocity in basal cerebral arteries. *Spec. Suppl.* **112,** 769–774 (2009).

19. Miyazaki, M. & Kato, K. Measurement of cerebral blood flow by ultrasonic Doppler technique : Theory. *Jpn. Circ. J.* **29,** 375–382 (1965).

20. Chivers, R. C. The scattering of ultrasound by human tissues—some theoretical models. *Ultrasound Med. Biol.* **3,** 1–13 (1977).

21. Senapati, N., Lele, P. P. & Woodin, A. A study of the scattering of sub-millimeter ultrasound from tissues and organs. *1972 Ultrasonics Symposium* 59–63 (1972).

22. Stakutis, V. J., Morse, R. W., Dill, M. & Beyer, R. T. Attenuation of ultrasound in aqueous suspensions. *J. Acoust. Soc. Am.* **27,** 539–546 (1955).

23. Burckhardt, C. B. Speckle in ultrasound B-mode scans. *IEEE Trans. Sonics Ultrason.* **25,** 1–6 (1978).

24. Gramiak, R. & Shah, P. M. Echocardiography of the aortic root. *Invest. Radiol.* **3,** 356–366 (1967).

25. Uhlendorf, V. & Hoffmann, C. Nonlinear acoustical response of coated microbubbles in diagnostic ultrasound. *1994 IEEE Ultrasonics Symposium, 1994. Proceedings* **3,** 1559–1562 (1994).

26. Ferrara, K., Pollard, R. & Borden, M. Ultrasound microbubble contrast agents: fundamentals and application to gene and drug delivery. *Annu. Rev. Biomed. Eng.* **9,** 415–447 (2007).

27. Epstein, P. S. & Plesset, M. S. On the stability of gas bubbles in liquid-gas solutions. *J. Chem. Phys.* **18,** 1505–1509 (1950).

28. Borden, M. A. & Longo, M. L. Dissolution behavior of lipid monolayer-coated, air-filled microbubbles: effect of lipid hydrophobic chain length. *Langmuir* **18,** 9225–9233 (2002).

29. Raisinghani, A. & DeMaria, A. N. Physical principles of microbubble ultrasound contrast agents. *Am. J. Cardiol.* **90,** 3–7 (2002).

30. De Jong, N., Emmer, M., van Wamel, A. & Versluis, M. Ultrasonic characterization of ultrasound contrast agents. *Med. Biol. Eng. Comput.* **47,** 861–873 (2009).

31. Mattrey, R. F. & Andre, M. P. Ultrasonic enhancement of myocardial infarction with perfluorocarbon compounds in dogs. *Am. J. Cardiol.* **54,** 206–210 (1984).

32. Correas, J. M. *et al*. The first phase shift ultrasound contrast agent: EchoGen. *Ultrasound Contrast Agents*. 101–120 (1997).

33. Podell, S., Golec, B. & Lohrmann, R. Measuring the effects of ultrasound on contrast agents. *1999 IEEE Ultrasonics Symposium, 1999. Proceedings* **2,** 1749–1754 (1999).

34. Forsberg, F. *et al.* Conventional and hypobaric activation of an ultrasound contrast agent. *Ultrasound Med. Biol.* **24,** 1143–1150 (1998).

35. Kripfgans, O. D., Miller, D. L., Fowlkes, J. B. & Carson, P. L. Vaporization of micrometer size droplets in simulated in vivo environments. *J. Acoust. Soc. Am.* **106,** 2191–2191 (1999).

36. Rapoport, N. *et al.* Ultrasound-mediated tumor imaging and nanotherapy using drug loaded, block copolymer stabilized perfluorocarbon nanoemulsions. *J. Controlled Release* **153,** 4–15 (2011).

37. Apfel, R. E. Activatable infusable dispersions containing drops of a superheated liquid for methods of therapy and diagnosis. U.S. Patent No. 5,840,276 filed 8 Jan. 1997, and issued 24 Nov. 1998.

38. Kripfgans, O. D., Fowlkes, J. B., Miller, D. L., Eldevik, O. P. & Carson, P. L. Acoustic droplet vaporization for therapeutic and diagnostic applications. *Ultrasound Med. Biol.* **26,** 1177–1189 (2000).

39. Bell, A. G. *Upon the Production of Sound by Radiant Energy*. Gibson Brothers, printers (1881).

40. Patel, C. K. N. & Tam, A. C. Pulsed optoacoustic spectroscopy of condensed matter. *Rev. Mod. Phys.* **53,** 517–550 (1981).

41. West, G. A., Barrett, J. J., Siebert, D. R. & Reddy, K. V. Photoacoustic spectroscopy. *Rev. Sci. Instrum.* **54,** 797–817 (1983).

42. Tam, A. C. Applications of photoacoustic sensing techniques. *Rev. Mod. Phys.* **58,** 381–431 (1986).

43. Sigrist, M. W. Laser generation of acoustic waves in liquids and gases. *J. Appl. Phys.* **60,** R83–R122 (1986).

44. Rosencwaig, A. *Photoacoustics and photoacoustic spectroscopy*. Wiley (1980).

45. Letokhov, V. S., & Zharov, V. P. Laser optoacoustic spectroscopy. *Springer Ser. Opt. Sci* **37** (1986).

46. Mandelis, A. *Principles and perspectives of photothermal and photoacoustic phenomena*. Elsevier (1992).

47. Gusev, V. E. & Karabutov, A. A. Laser optoacoustics. *Am. Inst. Phys.* 63–77 (1993).

48. Ntziachristos, V. & Razansky, D. Molecular imaging by means of multispectral optoacoustic tomography (MSOT). *Chem. Rev.* **110,** 2783–2794 (2010).

49. Wickramasinghe, H. K., Bray, R. C., Jipson, V., Quate, C. F. & Salcedo, J. R. Photoacoustics on a microscopic scale. *Appl. Phys. Lett.* **33,** 923–925 (1978).

50. Rosencwaig, A. & Gersho, A. Theory of the photoacoustic effect with solids. *J. Appl. Phys.* **47,** 64–69 (1976).

51. Park, H. K., Kim, D., Grigoropoulos, C. P. & Tam, A. C. Pressure generation and measurement in the rapid vaporization of water on a pulsed-laser-heated surface. *J. Appl. Phys.* **80,** 4072–4081 (1996).

52. Chen, H. & Diebold, G. Chemical generation of acoustic waves: a giant photoacoustic effect. *Science* **270,** 963–966 (1995).

53. Vogel, A., Busch, S. & Parlitz, U. Shock wave emission and cavitation bubble generation by picosecond and nanosecond optical breakdown in water. *J. Acoust. Soc. Am.* **100,** 148–165 (1996).

54. Diebold, G. J. & Sun, T. Properties of photoacoustic waves in one, two, and three dimensions. *Acta Acust. United Acust.* **80,** 339–351 (1994).

55. Yang, X., Stein, E. W., Ashkenazi, S. & Wang, L. V. Nanoparticles for photoacoustic imaging. *Wiley Interdiscip. Rev. Nanomed. Nanobiotechnol.* **1,** 360–368 (2009).

56. Luke, G. P., Yeager, D. & Emelianov, S. Y. Biomedical applications of photoacoustic imaging with exogenous contrast agents. *Ann. Biomed. Eng.* **40,** 422–437 (2012).

57. Kim, J.-W., Galanzha, E. I., Shashkov, E. V., Moon, H.-M. & Zharov, V. P. Golden carbon nanotubes as multimodal photoacoustic and photothermal high-contrast molecular agents. *Nat. Nanotechnol.* **4,** 688–694 (2009).

58. Shashkov, E. V., Everts, M., Galanzha, E. I. & Zharov, V. P. Quantum dots as multimodal photoacoustic and photothermal contrast agents. *Nano Lett.* **8,** 3953–3958 (2008).

59. Ku, G. *et al.* Copper sulfide nanoparticles as a new class of photoacoustic contrast agent for deep tissue imaging at 1064 nm. *ACS Nano* **6,** 7489–7496 (2012).

60. Jain, P. K., Lee, K. S., El-Sayed, I. H. & El-Sayed, M. A. Calculated absorption and scattering properties of gold nanoparticles of different size, shape, and composition: applications in biological imaging and biomedicine. *J. Phys. Chem. B* **110,** 7238–7248 (2006).

61. Mallidi, S. *et al.* Multiwavelength photoacoustic imaging and plasmon resonance coupling of gold nanoparticles for selective detection of cancer. *Nano Lett.* **9,** 2825–2831 (2009).

62. De La Zerda, A. *et al.* Carbon nanotubes as photoacoustic molecular imaging agents in living mice. *Nat. Nanotechnol.* **3,** 557–562 (2008).

63. Wang, L. V. & Hu, S. Photoacoustic tomography: in vivo imaging from organelles to organs. *Science* **335,** 1458–1462 (2012).

64. Homan, K. A. *et al.* Silver nanoplate contrast agents for in vivo molecular photoacoustic imaging. *ACS Nano* **6,** 641–650 (2012).

65. Strohm, E., Rui, M., Gorelikov, I., Matsuura, N. & Kolios, M. Vaporization of perfluorocarbon droplets using optical irradiation. *Biomed. Opt. Express* **2,** 1432–1442 (2011).

66. Wilson, K., Homan, K. & Emelianov, S. Biomedical photoacoustics beyond thermal expansion using triggered nanodroplet vaporization for contrast-enhanced imaging. *Nat. Commun.* **3,** 618 (2012).

67. Strohm, E. M., Rui, M., Kolios, M. C., Gorelikov, I. & Matsuura, N. Optical droplet vaporization (ODV): photoacoustic characterization of perfluorocarbon droplets. *2010 IEEE Ultrasonics Symposium (IUS)* 495–498 (2010).

68. Hannah, A., Luke, G., Wilson, K., Homan, K. & Emelianov, S. Indocyanine green-loaded photoacoustic nanodroplets: dual contrast nanoconstructs for enhanced photoacoustic and ultrasound imaging. *ACS Nano* **8,** 250–259 (2014).

69. Hannah, A. S., VanderLaan, D., Chen, Y.-S. & Emelianov, S. Y. Photoacoustic and ultrasound imaging using dual contrast perfluorocarbon nanodroplets triggered by laser pulses at 1064 nm. *Biomed. Opt. Express* **5,** 3042 (2014).

70. De Jong, N., Hoff, L., Skotland, T. & Bom, N. Absorption and scatter of encapsulated gas filled microspheres: Theoretical considerations and some measurements. *Ultrasonics* **30,** 95–103 (1992).

71. Leong-Poi, H. *et al.* Influence of microbubble shell properties on ultrasound signal: implications for low-power perfusion imaging. *J. Am. Soc. Echocardiogr.* **15,** 1269–1276 (2002).

Chapter 2: Design, Synthesis, and Characterization of Photoacoustic Nanodroplets

The design of the PAnDs is governed by their mechanisms of enhancing US and PA contrast. First, their echogenicity relies on an acoustic impedance (Z) mismatch between the particle and the surrounding tissue. Tissue is mostly water, so to reflect US waves, the contrast agent must differ in impedance ($Z = \rho c$). As synthesized, the contrast agent is an aqueous emulsion of liquid perfluorocarbon nanodroplets (Fig. 2.1 a1). The PFC density ranges from 1.59-1.67 g mL^{-1}, depending on the type of PFC (i.e. length of the perfluorocarbon chain). The speed of sound in PFC ranges from 400-550 m s^{-1}, yielding an acoustic impedance of 0.3-1.3 x 10^6 (kg m^{-2} s^{-1}), compared to water, whose impedance is 1.4 x 10^6 (kg m^{-2} s^{-1})[1–4]. For the particle to reflect US waves, it must convert from liquid to gas, vastly decreasing its density and speed of sound, thereby decreasing its acoustic impedance compared to the surrounding soft tissue. The mismatch leads to reflection of sound waves and a highly echogenic particle. This phase transition is traditionally induced using HIFU, where the peak rarefactional pressure induces vaporization[5]. However, in these studies, optical energy is used to induce the phase transition, which requires that an optical absorber is encapsulated in the particle, because PFC alone does not sufficiently absorb optical energy to cause vaporization (Fig. 2.1 a1). Once the droplet is synthesized, it can be activated using a pulsed laser, whereby optical energy is converted into heat and pressure that bring about the phase transition from nanodroplet to microbubble. This vaporization itself results in a massive pressure wave emission, which can be received by the US transducer as a photoacoustic emission (Fig. 2.1 a2, c2, d2). The resulting gas bubble reflects sound waves, providing US image contrast (Fig. 2.1 a3, b3, d3). Additionally, following vaporization of the droplet, the encapsulated photoabsorber can continue to absorb light from the pulsed laser and is a source of PA contrast based on thermal expansion (Fig. 2.1 a4, c4, d4).

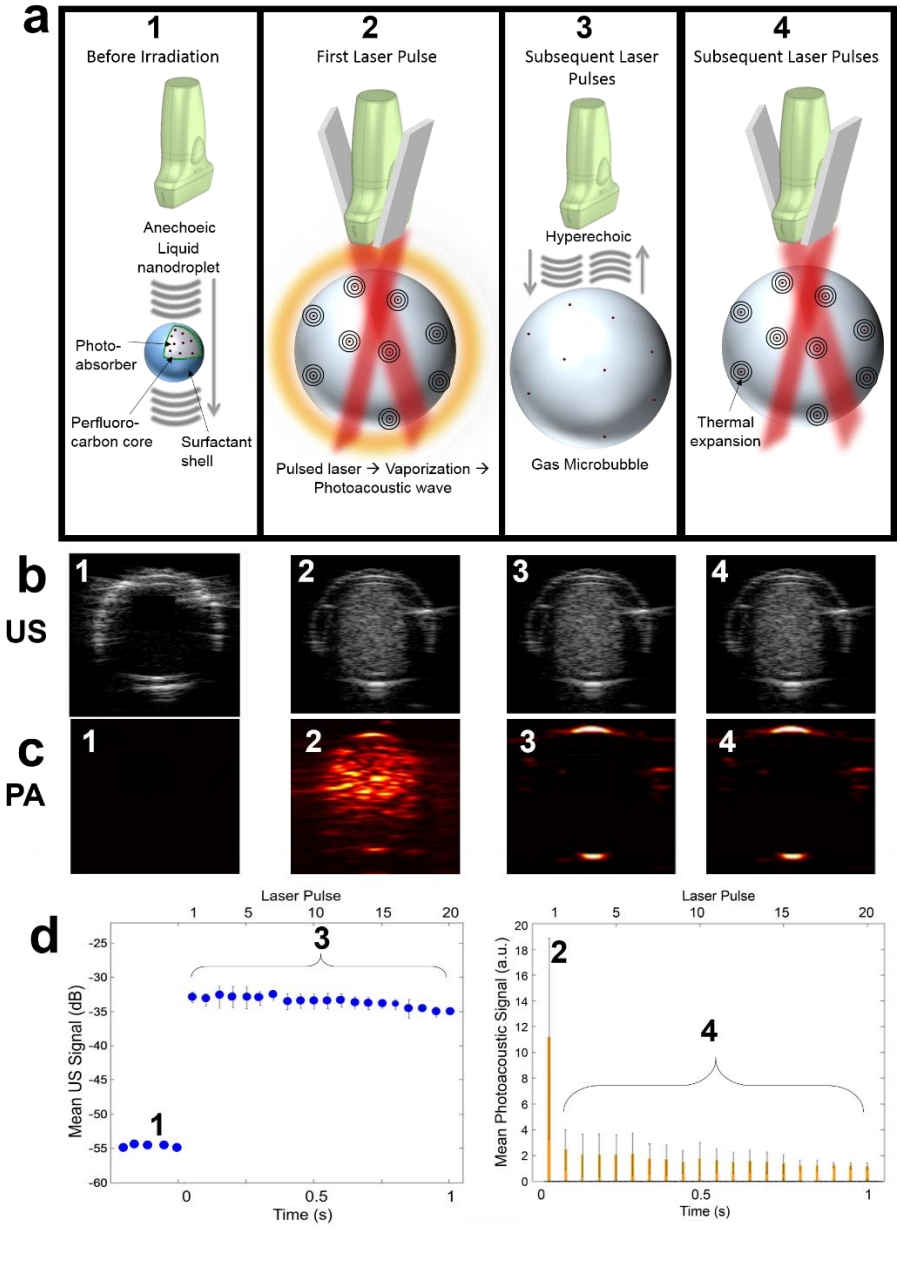

Figure 2.1: (a) Schematic of photoacoustic nanodroplets: (1) Nanodroplets in their liquid, anechoic state before activation, (2) Particles emitting strong photoacoustic signal upon pulsed laser irradiation, (3) Vaporized hyperechoic gas microbubbles, (4) Continued photoacoustic contrast from thermal expansion of the optical absorber. (b) Ultrasound and (c) photoacoustic images of the droplets during each stage of imaging, (d) Mean ultrasound and photoacoustic signal from the nanodroplets over time and corresponding laser pulses.

2.1. Benefits of Optically Triggered Nanodroplets

The triggered activation of the particles provides several advantages over traditional US and PA contrast agents. First, liquid nanodroplets are smaller than gas microbubbles[6], allowing for extravasation from leaky tumor neovasculature via the enhanced permeability and retention effect[7]. Their liquid state results in greater stability due to a lack of PFC diffusion, which gives them longer half-life *in vivo* for a longer imaging window[8,9]. While liquid nanodroplets can be triggered with HIFU and still confer the advantages mentioned, optically triggered nanodroplets provide additional advantages. First, PAnDs emit a strong, one-time PA signal upon vaporization, so they can be detected with higher contrast than microbubbles among many other endogenous optically absorbing chromophores such as blood and melanin[10]. Second, the energy required to vaporize nanodroplets using HIFU can be great and induce harmful microbubble bioeffects[11,12], so PAnDs provide a way to induce vaporization more safely.

2.2 Design Criteria

Several criteria were considered when designing the PAnDs for a biomedical imaging application. First, for a clinically relevant particle, the construct must be made entirely of safe, approved materials. A formulation of PAnDs has been synthesized entirely of approved materials—specifically FDA-approved indocyanine green dye—to meet this requirement[13]. Furthermore, the fate of the particles once injected is of concern. In addition to uptake by the tumor, perfluorocarbon emulsions show uptake by the liver, which varies depending on the shell material used[6]. This indicates that the surfactant shell—polymer, lipid, or protein—may affect the pharmacokinetics of the PAnDs. The lipid and BSA protein shells have been used in many applications and are safe for PAnD synthesis, and

the perfluorocarbon has been used in clinically available microbubble preparation. Ultimately, perfluorocarbons are eliminated through expiration[14–16].

Next, the contrast provided by the particles was considered. To maximize utility at biologically relevant imaging depths, the droplets must be sensitive to vaporization. Both the type of perfluorocarbon and photoabsorber can be modified to achieve this. Low boiling point PFCs, which have a shorter carbon chain, are more volatile, and PFC nanodroplets made from them vaporize in response to lower local laser fluence. However, if the boiling point is too low, synthesis of the particles becomes difficult, and droplets spontaneously vaporize at body temperature, eliminating their use. For a stable particle, the type of photoabsorber greatly affects the vaporization sensitivity. Although ICG dye is approved for clinical use, other encapsulated materials such as gold nanoparticles or nickel-based dyes provide stronger optical absorption and thus improved sensitivity to vaporization.

Lastly, for molecular imaging applications, the targeting strategy must be considered. For this reason, the shell material used to synthesize the droplets must be chemically compatible with a binding molecule. Previous reported formulations use lipid shells and avidin-biotin bonds[17–19] or antibody binding[20] to target PFC particles to a desired region, although many strategies have been explored[21,22].

2.3 Materials

The materials used to synthesize the droplets are as follows. First, the core of the droplet consists of a liquid perfluorocarbon. Droplets were synthesized using perfluorobutane (PFB), perfluoropentane (PFP), and perfluorohexane (PFH). Each of these differs in the length of the carbon chain, which has a drastic effect on the boiling point of the liquid and thus the properties of the droplets. The droplet is surrounded by a stabilizing shell, which yields a smaller particle due to its surfactant properties, and provides an interface for further decoration with targeting molecules. The shell material used was either

Photoabsorber	Pros	Cons
Indocyanine green	Clinically approved	Difficult to solubilize into PFC particles, absorbs relatively weakly, does not absorb strongly at 1064 nm, expensive
Gold nanorods	Absorb strongly, can be tuned to absorb at any wavelength	Requires extensive modification to encapsulate into PFC droplets, not clinically approved
Epolight™ 3072 dye	Hydrophobic, facile synthesis strong absorption at 1064 nm, enabling activation with Nd:YAG laser, inexpensive	Not clinically approved, contains Nickel
Quantum dots	Absorbs 1064 nm light, enabling activation using inexpensive Nd:YAG later	Weak absorber, difficult synthesis and incorporation into PFC
Acridine orange	Can encapsulate into PFC particles	Absorbs at 532 nm, not clinically approved
Methylene blue	Absorbs ~700 nm light	Difficult to encapsulate into PFC particles, not clinically approved

Table 2.1: Photoabsorbers used for optically triggered PFC nanodroplets

bovine serum albumin (BSA), a cocktail of lipids, or Zonyl FSO polymer. These materials may differ in resulting size of the droplets[23,24], stability[24], stiffness[25], and ability to attach targeting molecules[3].

Lastly, the PAnDs require an optical absorber; several different agents have been used to absorb light and induce vaporization. Preceding this work, gold nanorods were encapsulated in the PFC core[10]. Several options for photoabsorbers are explored and experimented with here, including indocyanine green (ICG), an FDA-approved dye commonly used for optical imaging (Fig. 2.2); high-aspect-ratio gold nanorods, which absorb light at 1064 nm; Epolight™ 3072 dye, which absorbs light at 1064 nm; Acridine Orange dye, which absorbs 430 nm light. Each absorber has its own advantages. Epolight™ is hydrophobic, soluble in PFC, and thus easy to incorporate into PAnDs, requiring no modification. Gold nanorods absorb light strongly, yielding a droplet sensitive to vaporization. Epolight™ is inexpensive, and ICG is clinically approved. A summary of the dyes can be found in Table 2.1.

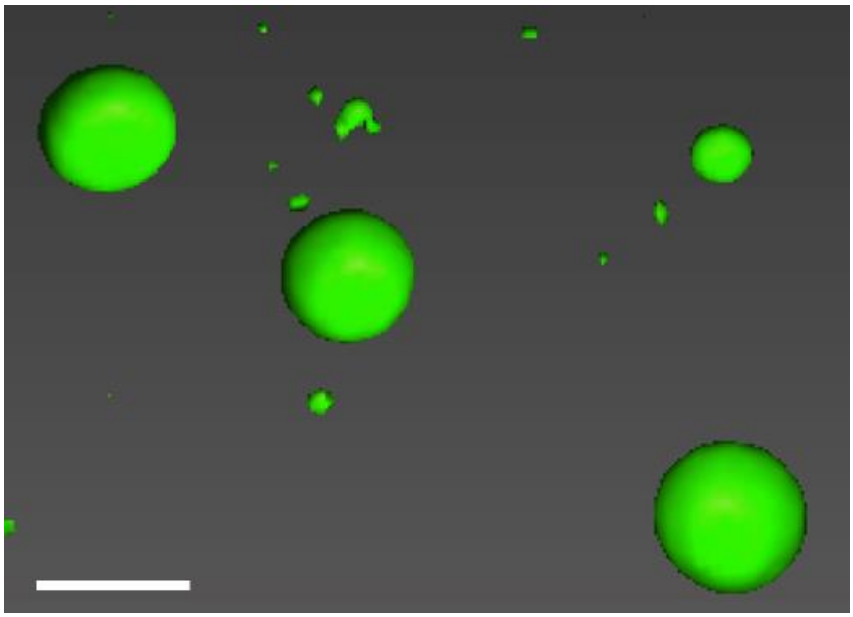

Figure 2.2: 3D rendering of larger synthesized ICG-loaded nanodroplets using confocal microscopy. Scale bar = 10 μm.

2.3.1 Synthesis of Indocyanine Green-Loaded Perfluorocarbon Nanodroplets

An emulsion of blank droplets consisting of a perfluorocarbon core surrounded by an albumin shell was first synthesized. First, 2.7 mL of 2 mg mL^{-1} bovine serum albumin (BSA) (Sigma) kept at 10 °C was added to an 8 mL glass scintillation vial. Next, 0.3 mL of perfluoropentane (Dodecafluoropentane) C_5F_{12} (FluoroMed) (PFP) was added to the vial. This solution was kept on ice to prevent evaporation of the PFP during creation of the emulsion, which has a boiling point of 29 °C. Next, the vial was shaken using a Mini Vortexer (VWR) on speed setting 10 for 10 s, to emulsify the PFP into submillimeter diameter droplets. An ultrasonic cleaner (VWR) was filled with water at 10 °C, and the vial was sonicated in the tank at 180 W for 3 min, while the vial was simultaneously shaken by hand, to emulsify the solution as much as possible and to disrupt the droplets into smaller sizes. A slight excess of PFP in the solution formed a bolus in the bottom of the vial, so ~2.5 mL of the 3 mL droplet solution was transferred to another 8 mL glass vial,

excluding the bolus of PFP. After emulsification into a nanodroplet size, the Laplace pressure increases the boiling point of the droplets to 70 °C or higher, depending on size.

Droplets can be made similarly with a shell consisting of Zonyl FSO, by mixing 1.7 mL of water with 1.0 mL of 1% v/v aqueous Zonyl FSO before adding perfluoropentane. Droplets can be made with a lipid shell in a manner similar to that reported by Marsh et al[26].

To encapsulate ICG as a photoabsorber, droplets were made with BSA as a shell. When droplets were made with Zonyl FSO as a shell, the droplets evaporated and dissolved during the process of encapsulating ICG. The ICG was encapsulated in the droplets using a modified method by Rodriguez et al[27]. A 1 mL solution of 2 mM ICG in chloroform was made by adding powdered ICG (Cardiogreen) (Sigma) to chloroform (Sigma). Depending on ICG supplier, the dissolution of ICG may require additional steps (Contact author for information). A separate 1 mL solution of 12 mM tetrabutylammonium iodide (TBAI) (Acros) in chloroform was made similarly. The 1 mL solution of TBAI was added to the ICG solution, resulting in a 1 mM ICG and 6 mM TBAI solution in chloroform. The solution was sonicated using a VWR Ultrasonic Cleaner at 180 W for 30 min.

The glass vial of blank droplets was placed on a stir plate and stirred at 1200 rpm, while 2 mL of the ICG-TBAI solution in chloroform was added dropwise. Next, a vacuum tube was attached to the top of the vial, and the chloroform was evaporated from the solution. Chloroform, whose bulk boiling point is 61 °C, evaporates more readily under vacuum than do the PFC droplets, most of which have a boiling point above 70 °C. All observable chloroform was evaporated from the emulsion, requiring approximately 30 min. A green-colored, milky solution of droplets remained. This solution was transferred to a 2.5 mL plastic centrifugation tube and centrifuged at 200 rcf for 5 min using a MiniSpin

plus centrifuge (Eppendorf). After centrifugation, a dark green pellet of droplets formed at the bottom of the tube, and the light green supernatant was discarded. The supernatant was replaced with water at 10 °C, and the droplets were resuspended by shaking in the Vortexer and sonicating in the VWR benchtop sonicator set at 180 W for 3 min. The solution was washed three times in this fashion, and the supernatant was colorless at the end of the third centrifugation. The droplet emulsion as made was diluted by 1000× in saline before experimentation, yielding a final droplet concentration of 10^6 droplets/mL and a dye payload of 0.58 μg mL^{-1} of ICG.

2.3.2 Synthesis of Nanodroplets Encapsulating Gold Nanorods

To synthesize PAnDs that encapsulate gold nanorods, first gold nanorods must be made using a seed-mediated growth method, and then the nanorods must be modified to be soluble in PFC or to adhere to the PAnD shell. First, a growth solution was made by adding 5.2 mL $AgNO_3$ (4 mM), 44 mL of water, 19.2 mL of HCl (1 M), and 8 mL of $HAuCl_4$ (10 mM) to 80 mL of CTAB (0.20 M) under gentle mixing, followed by the addition of 2.4 mL of ascorbic acid (0.0788 M). To make the seed solution, in a separate vial, 2.5 mL of CTAB solution (0.20 M) was mixed with 1.5 mL of $HAuCl_4$ solution (1 mM). Then 0.60 mL of ice-cold $NaBH_4$ solution (10 mM) was added to the mixture and vigorously stirred for 2 min at 25 °C, which resulted in the formation of a brownish yellow seed solution. To grow nanorods, 0.32 mL of the seed solution was added to the growth solution at 27–30 °C under gentle stirring for 30 seconds. The solution then aged for another 12 hours at 27–30 °C. The resulting gold nanorod solution was centrifuged at 5,000 rcf for 15 min to discard unwanted gold nanosphere side products; the nanospheres were concentrated in a pellet, while the nanorods remained in suspension. To reduce CTAB concentration, the nanorods were centrifuged twice at 18,000 rcf for 45 minutes. The CTAB-stabilized gold nanorod dispersion was added to an equal volume of aqueous mPEG-thiol (0.2 mM)

solution under vigorous stirring. The mixture was sonicated for 5 minutes and left to react for 8 hours. Excess mPEG-thiol molecules were removed by centrifugation filtration at 3,000 rcf for 10 min, and the PEGylated gold nanorods were re-suspended in water.

The surface chemistry of the PEGylated nanorods renders them hydrophilic and thus insoluble in organic PFC. To solubilize the nanorods in PFC, the surface of the nanorods was modified using an adapted method by Gorelikov et al[28]. Briefly, 15 mL of PEGylated nanorods were added to 5 mL of methanol and centrifuged at 2,500 rcf for 15 minutes. The supernatant was discarded, and the nanorods were resuspended in 15 mL of methanol. This was repeated 4 times. To fluorinate the nanorods, 300 μL of 1H,1H,2H,2H-perfluorodecyl-triethoxysilane was added to 15 mL of nanorods in methanol and stirred for 5 minutes, followed by the addition of 5 mL of a 28% ammonium hydroxide in water solution and stirred for 24 hours. The supernatant was removed by decanting and air flow, and the nanorods were resuspended in 0.3 mL of perfluoropentane by sonication. To synthesize the PAnDs, 0.3 mL of the now PFC-soluble nanorods was added to 2.2 mL of phosphate buffered saline (0.01 M) and 0.5 mL of 1% v/v Zonyl FSO fluorosurfactant, which was then vigorously shaken and sonicated using an ultrasonic cleaner. The solution was extruded through a 1.0 μm polycarbonate membrane to ensure that droplet size did not significantly exceed 1.0 μm. Previous studies of similar particles report a mean size of 600 nm diameter. The extinction spectrum of the aqueous nanorods was measured using a spectrophotometer to confirm the peak absorption wavelength. Previous formulations of optically triggered perfluorocarbon droplets show small shifts in peak optical absorption, as well as broadening of the absorption peak during nanodroplet synthesis[10,29,30]. This is consistent with modeled and measured optical properties of other composite nanoconstructs such as nanorods coated with silica of various thicknesses. The aqueous nanorods strongly absorb light around 1060 nm. While the nanorod-loaded PAnDs exhibit

scattering that increases at lower wavelengths, the strongest absorption remains in the NIR range, allowing them to be activated by an Nd:YAG laser emitting 1064 nm light.

2.4 Measurable Properties

2.4.1 Size, Absorption, Encapsulation Efficiency

The nanodroplets were characterized for size, dispersity, encapsulation efficiency, optical extinction spectrum, and targeting capabilities. The general size and range was observed using light microscopy (Fig. 2.3a), and then quantified with dynamic light scattering (Fig. 2.3b). The PAnDs range in size from 200 to over 1000 nm in diameter. Next, the encapsulation efficiency of the ICG-loaded PAnDs was measured using spectroscopy before and after washing the particles by centrifugation. The encapsulation efficiency of ICG in the droplets was 75%, with a payload of 0.58 mg of ICG per milliliter of sample. As made, the sample concentration is approximately 10^9 droplets/mL, yielding 5.8×10^{-10} mg ICG per droplet. The average droplet size was 600 nm with a dispersity of 0.28. Droplet size is influenced by BSA concentration, sonication time and power, as well as filter pore size during extrusion. For example, nanodroplets have been created with average diameters ranging from 200 to 1000 nm. In our studies, the nanodroplets have a 600 nm average diameter.

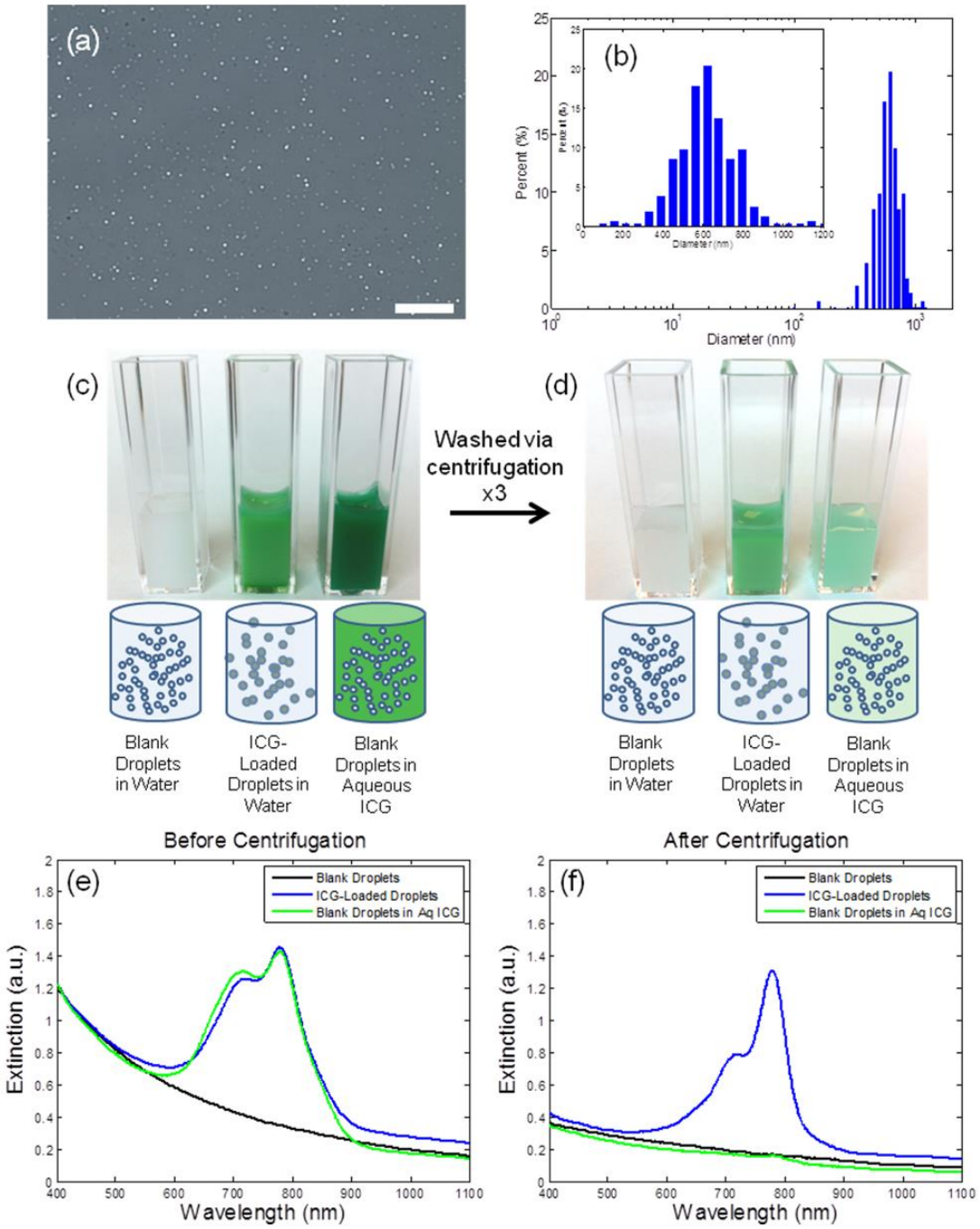

Figure 2.3: (a) Phase microscopy image of ICG-loaded PFC nanodroplets in water. (b) Size distribution of the droplets measured by dynamic light scattering. Photographs and diagrams of (c) prepared and (d) washed samples (from left to right): blank droplets in water, ICG-loaded droplets in water, and blank droplets in aqueous ICG. (e) Extinction spectra of the samples before and (f) after washing. Scale bar = 20 μm.

Three samples of droplets were synthesized for comparison of extinction spectra and dye encapsulation: blank PFC nanodroplets, ICG-loaded PAnDs, and blank PFC nanodroplets in a solution of aqueous ICG (Fig. 2.3c). The mass of ICG in the droplets before (Fig. 2.3c) and after (Fig. 2.3d) washing was measured using optical spectrometry. The ICG dye was added to a blank droplet solution until it reached equivalent optical density (OD) (1 cm path length) to that of the ICG-loaded droplets (Fig. 2.3e). After washing via centrifugation three times, the ICG-loaded droplets did not lose color, but the blank droplets in aqueous ICG did (Fig. 2.3d). The peak OD of the loaded droplets was 75% of its original value after washing, and the OD of blank droplets in aqueous ICG fell below the OD of blank droplets in water caused by scattering alone (Fig. 2.3f). These measurements indicate that some ICG is adherent to the droplet's BSA shell, which is expected due to the affinity of ICG to albumin[31]. However, the encapsulation method ensures that nearly all of the ICG added to the emulsion via solvent evaporation is present after washing, which is paramount to optically triggered vaporization.

To confirm that ICG was in the droplet PFC core, rather than dissolved in the aqueous solvent or adherent to the BSA shell, three samples of droplets were synthesized. These samples were similar to those previously mentioned, but larger in diameter, and imaged using confocal microscopy to identify the location of dye within the solution. The ICG is distributed throughout the PFC core of the particles when loaded using the reported method, whereas blank droplets in aqueous ICG do not encapsulate the dye within the particle (Fig. 2.4).

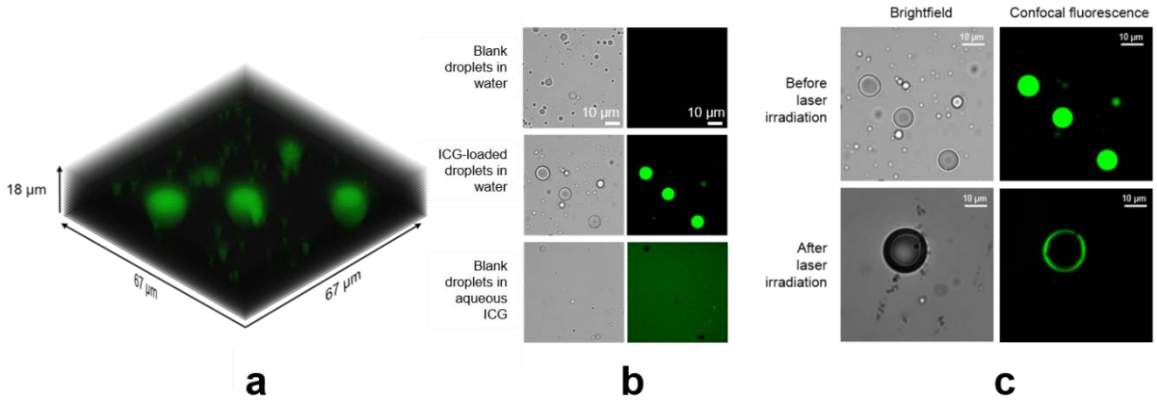

Figure 2.4: (a) Z-stack of confocal fluorescence images of ICG-loaded perfluorocarbon nanodroplets. (b) Brightfield (left) and confocal fluorescence images (right) of blank droplets in water (top), ICG-loaded droplets in water (middle), and blank droplets in aqueous ICG (bottom). (c) Brightfield (left) and confocal fluorescence (right) images of ICG-loaded nanodroplets before irradiation (top), and the resulting microbubbles after laser irradiation (bottom). Scale bars = 10 µm.

2.5. Optical Absorber for Activation

The peak optical absorption wavelength of the particles, and thus wavelength for activation, depends on the properties of the encapsulated photoabsorber. Initially in this work, droplets were synthesized with ICG to promote clinical translation of the particles (Fig. 2.5a). While this dye is clinically approved, its absorption of light is weaker than that of other optical absorbers used in imaging. The peak absorption of ICG-loaded droplets is in the 700-800 nm range (Fig. 2.5b). As previously mentioned, PAnDs were also synthesized using high aspect ratio gold nanorods as a photoabsorber (Fig. 2.5c), which can be tuned to absorb light strongly at 1064 nm (Fig. 2.5d). If imaging is conducted at 1064 nm, absorption of hemoglobin and blood is reduced, and the PAnDs can be activated by an inexpensive Nd:YAG laser source[32]. Finally, PAnDs were synthesized using Epolight™ 3072 dye which absorbs light around 1060 nm (Fig. 2.5e). While this dye is not clinically approved, its solubility in PFC makes for facile synthesis of PAnDs that are activated using a 1064 nm laser (Fig. 2.5f).

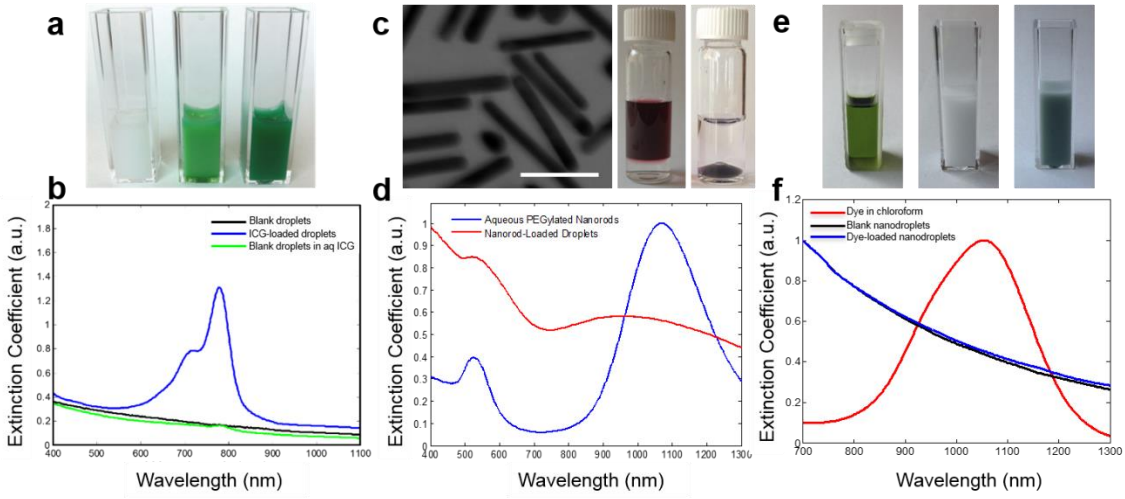

Figure 2.5: (a) Samples of droplets synthesized using ICG and (b) their extinction spectra. (c) Gold nanorods before and after modification for use in perfluorocarbon, and (d) extinction spectra of the rods and nanodroplets. (e) Near infrared absorbing Epolight™ 3072 dye used to make nanodroplets (left), blank droplets (middle), and dye-loaded droplets (right). (f) Extinction spectra of the dye and nanodroplets. Scale bar = 50 nm.

2.6 Synthesizing Targeted Nanodroplets

In contrast agent development, the targeting of specific biomarkers is a powerful tool for diagnosing and treating disease at the earliest stages, because these molecular signatures appear long before other identifiable characteristics[33–35]. In any area of biomedical imaging with contrast agents, researchers pursue the feasibility of targeting the agents to specific disease markers. While PAnDs are an emerging contrast agent, they share constituent characteristics with more commonly studied microbubbles, which have been used in many molecular targeting studies[18,19,36–40]. To show the feasibility of targeting with PAnDs, lipid-coated PFC nanodroplets were synthesized as described before. One sample of nanodroplets was additionally modified with an anti-EGFR antibody. Next, two samples of identical BT474 breast cancer cells were incubated with PAnDs for 2 hours, one

containing the antibody. After incubation, the cells were washed and then imaged using optical microscopy. Images show the greater affinity of the antibody-conjugated PAnDs for breast cancer cells (Fig. 2.6).

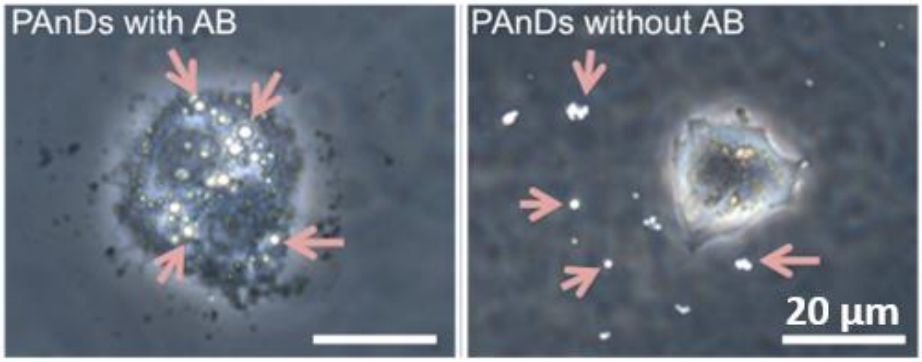

Figure 2.6: Phase microscopy images of BT474 breast cancer cells after mixing with antibody-conjugated (left) and non-antibody-conjugated nanodroplets. Arrows indicate the location of the droplets.

2.7 Conclusions

Optically activatable perfluorocarbon nanodroplets were designed according to the criteria of high US and PA contrast, biocompatibility, clinical translation, sensitivity for deep imaging, and cost. By varying the type of photoabsorber, a particle can be synthesized with clinically approved materials (ICG), one with biocompatible materials capable of triggering by an inexpensive Nd:YAG laser (gold nanorods), and one with facile synthesis and activation using an ND:YAG laser (Epolight™ 3072 dye). The small size and targeting capabilities make them a strong candidate for molecular based imaging of early stage tumors.

2.8 References

1. Hoe, S., Young, P. M., Rogueda, P. & Traini, D. Determination of reference ultrasound parameters for model and hydrofluoroalkane propellants using high-resolution ultrasonic spectroscopy. *AAPS PharmSciTech* **9,** 605–611 (2008).
2. Shpak, O. *et al.* Acoustic droplet vaporization is initiated by superharmonic focusing. *Proc. Natl. Acad. Sci.* **111,** 1697–1702 (2014).
3. Rapoport, N. Y., Kennedy, A. M., Shea, J. E., Scaife, C. L. & Nam, K.-H. Controlled and targeted tumor chemotherapy by ultrasound-activated nanoemulsions/microbubbles. *J. Controlled Release* **138,** 268–276 (2009).
4. Jafari, S. *et al.* High-frequency (20 to 40 MHz) acoustic response of liquid-filled nanocapsules. *IEEE Trans. Ultrason. Ferroelectr. Freq. Control* **61,** 5–15 (2014).
5. Kripfgans, O. D., Fowlkes, J. B., Miller, D. L., Eldevik, O. P. & Carson, P. L. Acoustic droplet vaporization for therapeutic and diagnostic applications. *Ultrasound Med. Biol.* **26,** 1177–1189 (2000).
6. Rapoport, N. *et al.* Ultrasound-mediated tumor imaging and nanotherapy using drug loaded, block copolymer stabilized perfluorocarbon nanoemulsions. *J. Controlled Release* **153,** 4–15 (2011).
7. Prabhakar, U. *et al.* Challenges and key considerations of the enhanced permeability and retention effect for nanomedicine drug delivery in oncology. *Cancer Res.* **73,** 2412–2417 (2013).
8. Hu, G. *et al.* Imaging of Vx-2 rabbit tumors with αvβ3-integrin-targeted 111In nanoparticles. *Int. J. Cancer* **120,** 1951–1957 (2007).

9. Lin, C.-Y. & Pitt, W. G. Acoustic droplet vaporization in biology and medicine. *BioMed Res. Int.* **2013,** e404361 (2013).

10. Wilson, K., Homan, K. & Emelianov, S. Biomedical photoacoustics beyond thermal expansion using triggered nanodroplet vaporization for contrast-enhanced imaging. *Nat. Commun.* **3,** 618 (2012).

11. Nyborg, W. L. Safety of medical diagnostic ultrasound. *Semin. Ultrasound CT MRI* **23,** 377–386 (2002).

12. Haar, G. ter. Safety and bio-effects of ultrasound contrast agents. *Med. Biol. Eng. Comput.* **47,** 893–900 (2009).

13. Hannah, A., Luke, G., Wilson, K., Homan, K. & Emelianov, S. Indocyanine green-loaded photoacoustic nanodroplets: dual contrast nanoconstructs for enhanced photoacoustic and ultrasound imaging. *ACS Nano* **8,** 250–259 (2014).

14. Naito, R. & Yokoyama, K. An improved perfluorodecalin emulsion. *Prog. Clin. Biol. Res.* **19,** 81–89 (1978).

15. Riess, J. G. The design and development of improved fluorocarbon-based products for use in medicine and biology. *Artif. Cells Blood Substit. Biotechnol.* **22,** 215–234 (1994).

16. Yokoyama, K. *et al.* Preparation of perfluorodecalin emulsion, an approach to the red cells substitute. *Fed. Proc.* **34,** 1478–1483 (1975).

17. Klibanov, A. L. *et al.* Targeting of ultrasound contrast material: selective imaging of microbubbles in vitro. *Academic Radiology.* **5,** S243-S246 (1998).

18. Lanza, G. M. *et al.* A novel site-targeted ultrasonic contrast agent with broad biomedical application. *Circulation* **94,** 3334–3340 (1996).

19. Marsh, J. N. *et al.* Molecular imaging with targeted perfluorocarbon nanoparticles: quantification of the concentration dependence of contrast enhancement for binding to sparse cellular epitopes. *Ultrasound Med. Biol.* **33,** 950–958 (2007).

20. Villanueva, F. S. *et al.* Microbubbles targeted to intercellular adhesion molecule-1 bind to activated coronary artery endothelial cells. *Circulation* **98,** 1–5 (1998).

21. Dayton, P. A. & Ferrara, K. W. Targeted imaging using ultrasound. *J. Magn. Reson. Imaging* **16,** 362–377 (2002).

22. Klibanov, A. L. Preparation of targeted microbubbles: ultrasound contrast agents for molecular imaging. *Med. Biol. Eng. Comput.* **47,** 875–882 (2009).

23. Schad, K. C. & Hynynen, K. In vitro characterization of perfluorocarbon droplets for focused ultrasound therapy. *Phys. Med. Biol.* **55,** 4933 (2010).

24. Huynh, E. *et al.* Porphyrin shell microbubbles with intrinsic ultrasound and photoacoustic properties. *J. Am. Chem. Soc.* **134,** 16464–16467 (2012).

25. Reznik, N. *et al.* On the acoustic properties of vaporized submicron perfluorocarbon droplets. *Ultrasound Med. Biol.* **40,** 1379–1384 (2014).

26. Marsh, J. N. *et al.* Improvements in the ultrasonic contrast of targeted perfluorocarbon nanoparticles using an acoustic transmission line model. *IEEE Trans. Ultrason. Ferroelectr. Freq. Control* **49,** 29–38 (2002).

27. Rodriguez, V. B. *et al.* Encapsulation and stabilization of indocyanine green within poly(styrene-alt-maleic anhydride) block-poly(styrene) micelles for near-infrared imaging. *J. Biomed. Opt.* **13,** 014025-1–014025-10 (2008).

28. Gorelikov, I., Martin, A. L., Seo, M. & Matsuura, N. Silica-coated quantum dots for optical evaluation of perfluorocarbon droplet interactions with cells. *Langmuir* **27,** 15024–15033 (2011).

29. Strohm, E., Rui, M., Gorelikov, I., Matsuura, N. & Kolios, M. Vaporization of perfluorocarbon droplets using optical irradiation. *Biomed. Opt. Express* **2,** 1432–1442 (2011).

30. Dove, J. D., Mountford, P. A., Murray, T. W. & Borden, M. A. Engineering optically triggered droplets for photoacoustic imaging and therapy. *Biomed. Opt. Express* **5,** 4417 (2014).

31. Landsman, M. L., Kwant, G., Mook, G. A., & Zijlstra, W. G. Light-absorbing properties, stability, and spectral stabilization of indocyanine green. *J. Appl. Physiol.* **40,** 575–583 (1976).

32. Homan, K. *et al.* Prospects of molecular photoacoustic imaging at 1064 nm wavelength. *Opt. Lett.* **35,** 2663–2665 (2010).

33. Ramaswamy, S., Ross, K. N., Lander, E. S. & Golub, T. R. A molecular signature of metastasis in primary solid tumors. *Nat. Genet.* **33,** 49–54 (2003).

34. Charafe-Jauffret, E. *et al.* Breast cancer cell lines contain functional cancer stem cells with metastatic capacity and a distinct molecular signature. *Cancer Res.* **69,** 1302–1313 (2009).

35. Cuezva, J. M. *et al.* The bioenergetic signature of lung adenocarcinomas is a molecular marker of cancer diagnosis and prognosis. *Carcinogenesis* **25,** 1157–1163 (2004).

36. Kaneda, M. M., Caruthers, S., Lanza, G. M. & Wickline, S. A. Perfluorocarbon nanoemulsions for quantitative molecular imaging and targeted therapeutics. *Ann. Biomed. Eng.* **37,** 1922–1933 (2009).

37. Lanza, G. M. *et al.* Targeted antiproliferative drug delivery to vascular smooth muscle cells with a magnetic resonance imaging nanoparticle contrast agent implications for rational therapy of restenosis. *Circulation* **106,** 2842–2847 (2002).

38. Waters, E. A. *et al.* Detection of targeted perfluorocarbon nanoparticle binding using 19F diffusion weighted MR spectroscopy. *Magn. Reson. Med.* **60,** 1232–1236 (2008).

39. Takalkar, A. M., Klibanov, A. L., Rychak, J. J., Lindner, J. R. & Ley, K. Binding and detachment dynamics of microbubbles targeted to P-selectin under controlled shear flow. *J. Controlled Release* **96,** 473–482 (2004).

40. Lankford, M. *et al.* Effect of microbubble ligation to cells on ultrasound signal enhancement: implications for targeted imaging. *Invest. Radiol.* **41,** 721–728 (2006).

Chapter 3: Ultrasound and Photoacoustic Imaging of PAnDs: Phantoms and *Ex vivo*

To determine if the optically triggerable nanoparticles are functional as an imaging agent, several experiments were conducted. First, the nanodroplets were simply imaged as synthesized in aqueous solution using US and PA methods. They were imaged *ex vivo* to validate their behavior in a tissue-mimicking environment, and to assess the contrast of PAnDs activated with 1064 nm light. In later chapters, *in vivo* imaging experimental results are reported.

It is also critically important in imaging experiments to quantify the enhancement of images from the contrast agent. Therefore the collected data was used to calculate image contrast and contrast-to-noise ratio, which is reported here.

3.1 Ultrasound and Photoacoustic Imaging of Nanodroplets in Solution

To test the ability of the PAnDs to improve US and PA image contrast, and to characterize their imaging properties, a series of components was assembled as shown in Fig 3.1a.

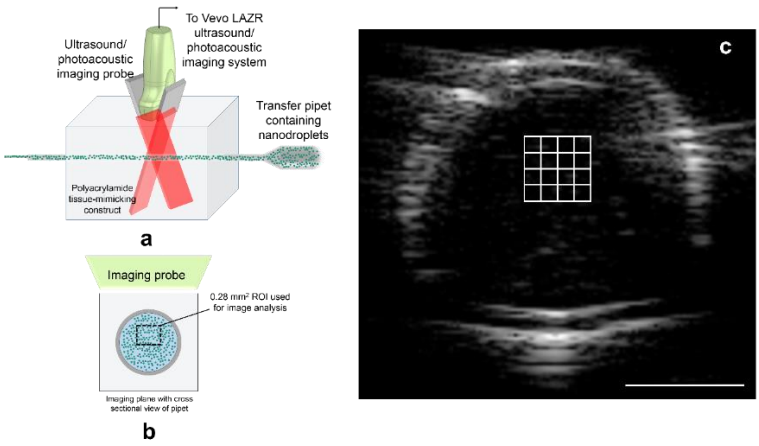

Figure 3.1: (a) Imaging setup for nanodroplet samples, using a Vevo LAZR dual US/PA imaging system. (b) Depiction of droplets within the pipette in the ultrasound imaging plane. (c) Ultrasound image depicted with the subsectioned ROI used for signal analysis. Scale bar = 2 mm.

The PAnDs were synthesized, diluted 1000x and aspirated into a transfer pipette. To stabilize the transfer pipette during irradiation and for ease of imaging, it was inserted into a block made of polyacrylamide gel. To construct the gel, 64 mL of water was stirred at room temperature, and added to the water was 21 mL of 40% acrylamide (Ambion), 850 μL of ammonium persulfate (Sigma-Aldrich), and 106 μL of tetramethylethylenediamine (TEMED) (Sigma). The solution was poured into a mold which contained an inclusion to create a hole for the pipette. The phantom set in 20 min and was stored submerged in water in the refrigerator until ready for use.

The gel block was placed under a Vevo 21 MHz US/PA imaging probe, which was connected to the combined US/PA VevoLAZR imaging system (Fig. 3.1a). Ultrasound gel was applied to the block and the probe was positioned so that the optical beams intersected at the position of the pipette. Ultrasound B-mode data was first collected from the cross section of the pipette (Fig. 3.1b) without optical irradiation, in which droplet samples were suspended. The transmit US power was set to 1% to avoid or minimize any mechanical (i.e. pressure) contribution to droplet vaporization (1% power ~350 kPa). The imaging system was operating in a single-focus imaging mode, with the ultrasound beam focused at 20 mm below the surface of the transducer. The pipette was placed so that its cross section spanned 9–13 mm range below the transducer. Because droplets are denser (1.6 g mL^{-1}) than the aqueous solvent, a new sample of droplets was aspirated into a pipette to prevent droplet settling within the before PA imaging began. The pipette was inserted into the gel block, and the laser was turned on while US and PA data were simultaneously collected. The 780 nm wavelength, 5 ns laser pulses irradiated the sample at 20 pulses/s and a fluence of 20 mJ cm^{-2}, while US and PA frames were captured at a rate of one frame per laser pulse (20 frames/s). B-mode IQ data was collected for analysis of contrast enhancement by custom-designed programs developed in MATLAB.

To measure the mean US signal for a given laser pulse (frame), the signal was converted to dB, then averaged in the ROI (Fig. 3.1c). Each point in the graph is calculated by

$$Mean\ US\ Signal = \frac{\sum_{i=1}^{N} 20log_{10}(I_i)}{N} \tag{3.1}$$

where I_i is the normalized (by maximum pixel of all US images) linear intensity of each pixel in the ROI, and N is the total number of pixels in the ROI. The selection of the ROI within the image frame (Fig. 3.1c) has an effect on the resulting measurement of mean US signal. Because acoustic shadowing occurs more at higher temperatures, there is a gradient of US signal intensity with depth (deeper → more shadowing → artificially lower signal). By selecting the ROI close to the top of the pipette, this effect is minimized, and it is more accurately shown that at 50 °C there is more vaporization than at 37 °C.

Using the same signals at various temperatures (23 °C, 37 °C, 50 °C), contrast and contrast-to-noise (CNR) were computed from the activated ICG-loaded PAnDs:

$$Contrast = \frac{\mu(I_{i,bubbles}) - \mu(I_{i,background})}{\mu(I_{i,background})} \tag{3.2}$$

$$CNR = 20log_{10}\frac{\mu(I_{i,bubbles}) - \mu(I_{i,background})}{\sigma(I_{i,background})} \tag{3.3}$$

where I_i is the average linear US intensity in one of the 16 sub-ROIs in the US image, $\mu(I_{\text{i, bubbles}})$ is an average of 16 values of I_i, where each I_i is an average of all pixel values (linear US signal) in the small square. $I_{\text{i, background}}$ is calculated the same way, using an ROI (and 16 sub-ROIs) outside of the pipette region, and σ is the standard deviation of 16 values of I_i.

Photoacoustic measurements were made in an identical fashion, but using the PA images from the first laser pulse as a measurement of signal rather than the US images. Several values of contrast and CNR were obtained by moving the ROI within the image.

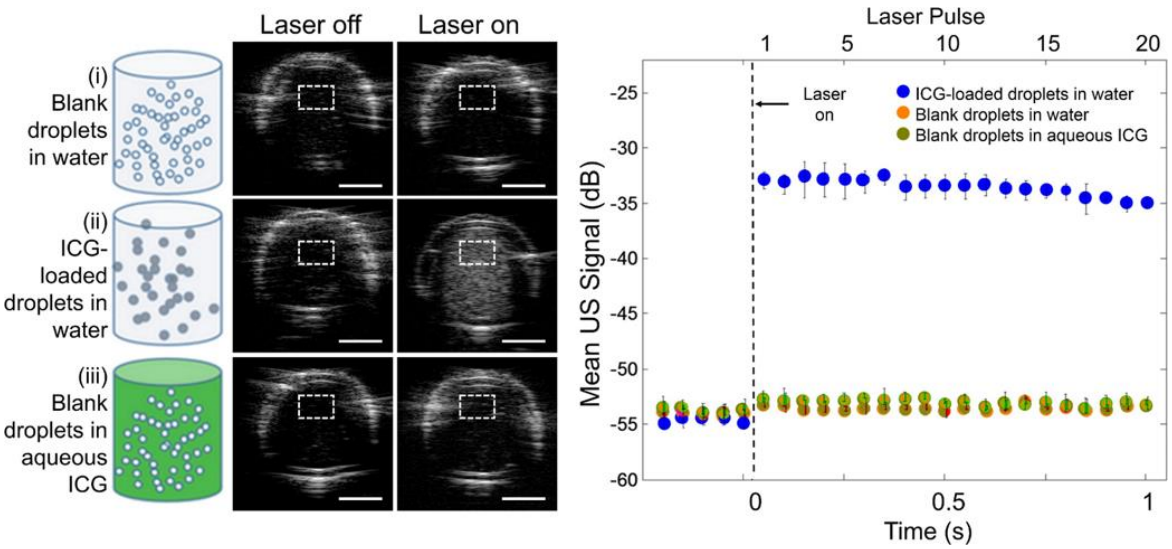

Figure 3.2: Ultrasound images before and after laser irradiation of samples of (i) blank droplets in water, (ii) ICG-loaded droplets in water, and (iii) blank droplets in aqueous ICG (50 dB display dynamic range), and average US intensity in the ROI for each US frame. Error bar represents 1 standard deviation above and 1 standard deviation below the mean value. $N \geq 3$ for all reported values, 37 °C, scale bar = 2 mm.

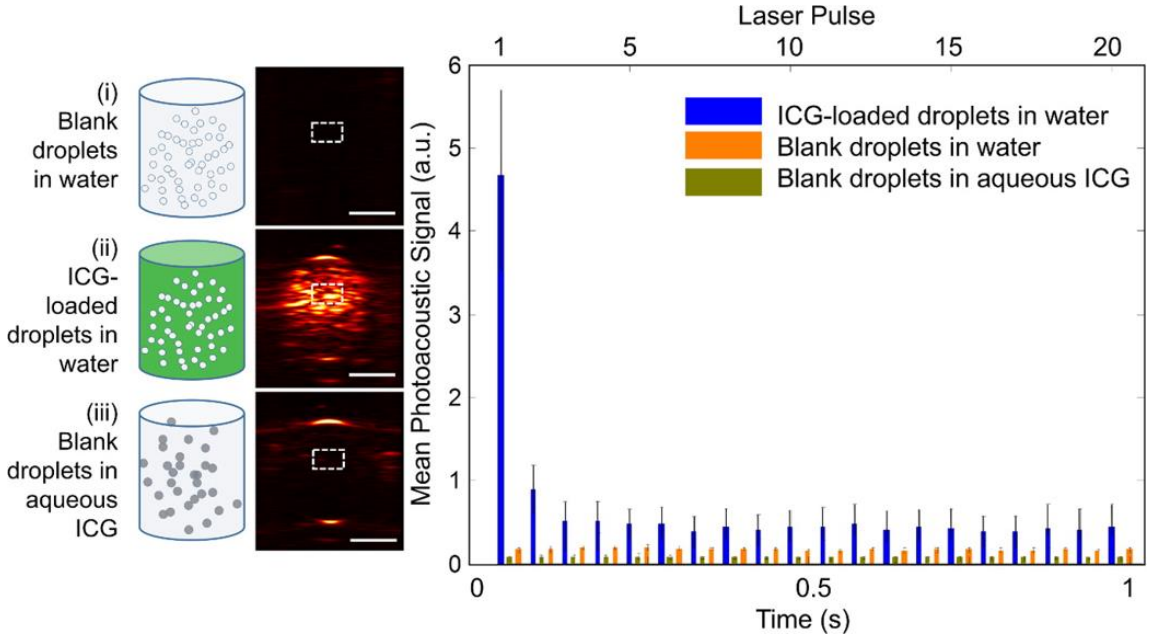

Figure 3.3: Diagram and PA image from the first laser pulse irradiating the samples of (i) blank droplets in water, (ii) ICG-loaded droplets in water, and (iii) blank droplets in aqueous ICG. Average PA intensity, measured in the denoted ROI, over a number of laser pulses (20 pulses/s) or time. Error bar represents 1 standard deviation above and 1 standard deviation below the mean value. $N \geq 3$ for all reported values, 37 °C, scale bar = 2 mm.

To verify droplet vaporization and assess contrast enhancement, B-mode US data were collected from the same three samples, both before and during laser irradiation. The US images of the ICG-loaded droplets exhibit a drastic increase in US contrast upon irradiation, which is absent in the other two samples of blank droplets (Fig. 3.2). The US contrast increases from 1.2 to 14 (a.u.), and the CNR increases from 21 to 46 dB (Table 3.1). In its liquid droplet form, the PFC adds little US contrast to an aqueous background because of its similar acoustic impedance. However, upon optical triggering of an ICG-loaded PFC-droplet, the acoustic impedance of gaseous PFC decreases due to a substantial decrease in density and slight decrease in speed of sound, as indicated by the change in US contrast.

The photoacoustic contrast enhancement through droplet vaporization is shown after the initial laser pulse, and the average signal is quantified over several pulses (Fig. 3.3). A Vevo LAZR imaging system was used to simultaneously collect US and PA data from the samples, using a laser emitting 780 nm light at a fluence of 20 mJ cm^{-2}. Photoacoustic images of a sample containing either (i) washed blank droplets in water, (ii) washed ICG-loaded droplets in water, or (iii) unwashed blank droplets in aqueous ICG (Fig. 3.3) were measured. Upon irradiation, the blank droplets in water emitted no PA signal that was detectable (i.e. the signal was below the system noise). However, for ICG-loaded droplets, the PA signal due to vaporization was 10x higher than that of the system noise, indicating that the dye encapsulated inside the droplet is an effective optical trigger, and the particles are a source of high PA signal. There was no detectable PA signal from blank droplets in aqueous ICG, indicating that an equivalent amount of ICG outside the droplets does not induce vaporization. The PA and US images were further acquired for subsequent laser pulses—a movie made up of US and PA images of the sample of ICG-loaded droplets and blank droplets in aqueous ICG during irradiation can be obtained upon request from the author. In each image, PA signal was averaged over a 0.23 mm^2 ROI to demonstrate droplet behavior as a function of laser pulse over 1 s (Fig. 3.3). Upon irradiation, the PA image contrast is 36 (a.u.), and the contrast-to-noise ratio (CNR) is 51 dB (Table 3.1), compared to 1.1 (a.u.) and 19 dB, respectively, for blank droplets in aqueous ICG. Subsequent laser pulses result in substantially lower PA signal, because very few additional droplets vaporize from these pulses. Almost all droplets that are large enough to vaporize within the sample undergo this phase transition after a single pulse.

	Before Lasing			During Lasing		
	23 °C	37 °C	50 °C	23 °C	37 °C	50 °C
	Average Ultrasound Measurements +/- 1 x Standard Deviation					
Contrast (a.u.)	1.0 +/-0.03	1.2 +/- 0.06	1.7 +/- 0.09	6.1 +/- 0.2	14 +/- 0.3	19 +/- 0.3
CNR (dB)	20 +/- 1.1	21 +/- 0.8	23 +/- 2.1	38 +/- 0.1	46 +/- 0.4	47 +/- 1.1
	Average Photoacoustic Measurements +/- 1 x Standard Deviation					
Contrast (a.u.)	N/A	N/A	N/A	12 +/- 5.6	36 +/- 11	49 +/- 18
CNR (dB)	N/A	N/A	N/A	41 +/- 4.7	51 +/- 6.2	55 +/- 8.6

Table 3.1: Quantified image enhancement for ICG-loaded nanodroplets.

*N>3 for all measurements

3.2 Tissue-Mimicking Phantom Imaging

To demonstrate vaporization of PAnDs loaded with gold nanorods and activated by a 1064 nm Nd:YAG laser, a polyacrylamide phantom was synthesized with embedded PAnDs at a concentration of approximately 10^8 droplets/mL. The phantom was brought to 37 °C in a water bath. To induce vaporization, a pulsed Nd:YAG laser was used to irradiate the phantom at a fluence of up to 90 mJ cm^{-2}, a value greater than the fluence threshold for droplet vaporization under these conditions. An air beam of spot size approximately 27 mm^2 directly irradiated the phantom. To demonstrate that droplet vaporization is localized to the region of irradiation, a star shaped vinyl mask was used to cover the phantom, and the phantom was mechanically scanned during irradiation, so that only the unmasked region was exposed to the laser. After irradiation, the phantom was imaged with a Vevo 2100 US imaging system. A 21 MHz array transducer was used in pulse/receive mode to collect B-mode data of the phantom (Fig 3.4a). Additionally, another phantom

was irradiated using a dual fiber bundle system to visualize the optical path and irradiated area (Fig. 3.5b).

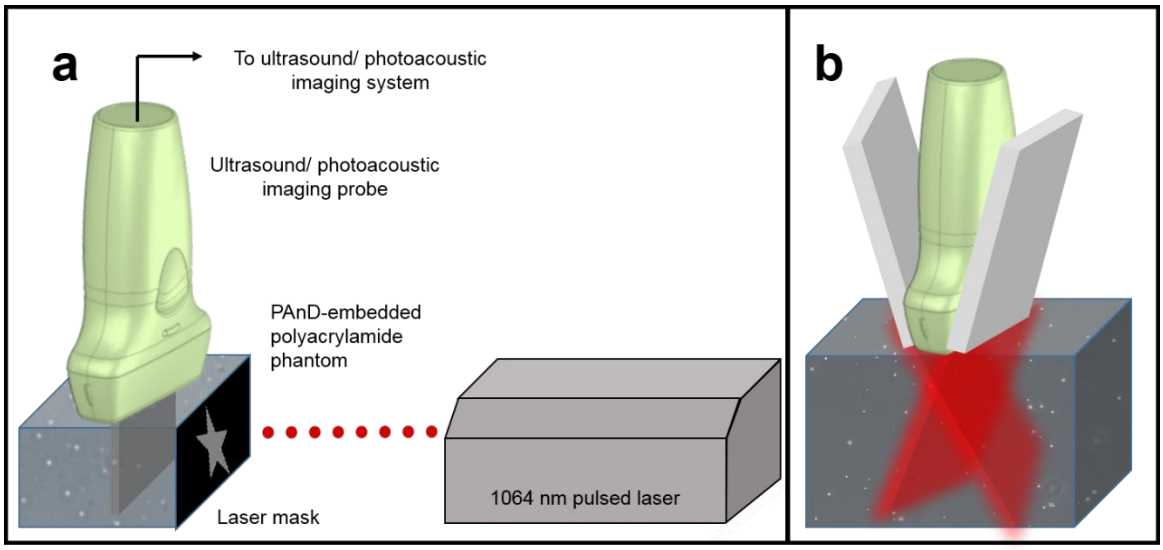

Figure 3.4: (a) Tissue-mimicking polyacrylamide phantom embedded with nanodroplets and irradiated with light through a star-shaped mask. (b) Similar phantom irradiated through dual optical fiber bundles.

Following the selectively masked irradiation of droplet-laden phantoms, the B-mode scans exhibited greater echogenicity in the irradiated regions (Fig. 3.5). After the liquid-to-gas transition of the liquid nanodroplet into a gas microbubble, the local mechanical properties are greatly perturbed, resulting in a contrast of 33 (unitless), and a contrast-to-noise ratio (CNR) of 41 dB (Table 3.1).

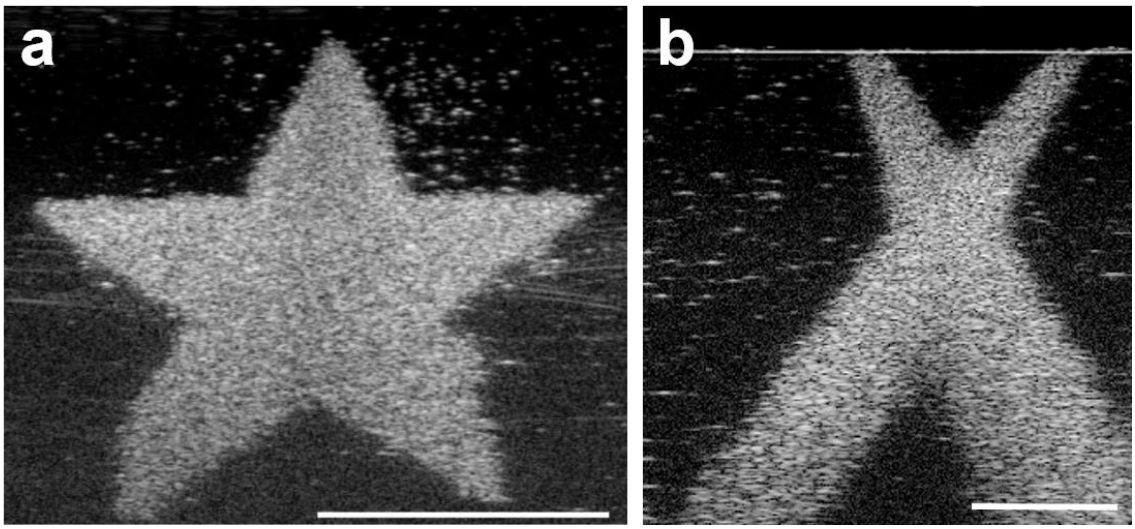

Figure 3.5: Ultrasound images of phantoms after laser irradiation. Scale bars = 10 mm (a), 5 mm (b).

3.3 *Ex Vivo* Imaging

Ultrasound and photoacoustic imaging studies of the PAnDs were conducted in a tissue-mimicking environment using porcine tissue as an imaging medium, whose optical and acoustic absorption and scattering mimic human tissue[1]. A portion of the tissue, free of large pieces of fat, was cut into a 3x3x1 cm slab and brought to 37 °C in a water bath. Before injection of nanodroplets, the tissue was imaged using US and PA systems to establish background signal. Next, a 0.5 mL bolus of PAnDs (3×10^{11} droplets/mL) was injected into the sample, 1 cm from the front of the tissue where the laser is incident, and 1 cm from the top surface where the US transducer contacts the sample, using US imaging to guide a needle and to ensure the injection of the droplets within the imaging plane (Fig. 3.6). A higher concentration of droplets was used to maximize the probability of vaporization and contrast enhancement. While the laser light was blocked, the tissue was imaged simultaneously with US and PA techniques, establishing a PA noise floor and measuring US contrast of the injected liquid-phase PAnDs. The sample was then exposed

to 1064 nm laser light pulses at a fluence of 90 mJ cm^{-2} while PA and US image data was collected over 20 pulses, at a rate of 20 pulses/s.

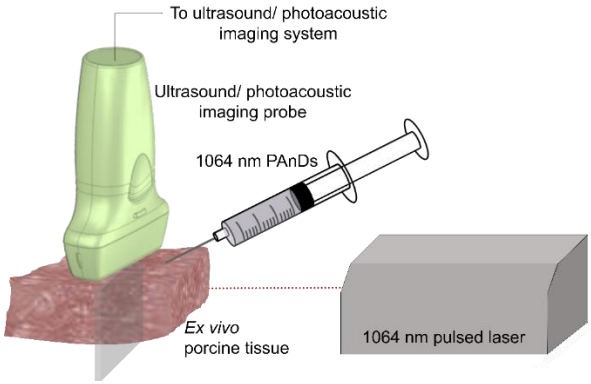

Figure 3.6: Porcine tissue injected with PAnDs, then probed simultaneously using B-mode ultrasound and photoacoustic imaging techniques.

The data was analyzed to quantify the image contrast enhancement within the porcine tissue and to measure the contribution of the particles to image signal over the native tissue. To do so, two contrast metrics were considered: the absolute contrast and local contrast. The absolute contrast, or modulation, is given as follows:

$$Contrast_{abs} = \frac{\mu(A_{i,ROI}) - \mu(A_{i,blank})}{\mu(A_{i,blank})} \quad (3.4)$$

where $\mu(A_{i,ROI})$ is the mean signal amplitude of the PAnDs in the region of interest, calculated using 12 sub-sections, and $\mu(A_{i,blank})$ is the mean amplitude of an image with no target. For PA images, $\mu(A_{i,blank})$ is the mean PA image amplitude when the laser source is blocked from irradiating the target. For US images, $\mu(A_{i,blank})$ is the mean US image amplitude of a sample of degassed water.

Local contrast within the porcine tissue sample was measured as follows:

$$Contrast_{local} = \frac{\mu(A_{i,ROI}) - \mu(A_{i,tissue})}{\mu(A_{i,tissue})} \quad (3.5)$$

where $\mu(A_{i,tissue})$ is the mean amplitude of the surrounding regions of the contrast-enhanced image. From these data, the contrast-to-noise ratios (CNRs) were considered. These were calculated using the following formulas:

$$CNR_{abs} = 20log_{10}\frac{\mu(A_{i,ROI}) - \mu(A_{i,blank})}{\sigma(A_{i,blank})} \quad (3.6)$$

and

$$CNR_{local} = 20log_{10}\frac{\mu(A_{i,ROI}) - \mu(A_{i,tissue})}{\sigma(A_{i,tissue})} \quad (3.7)$$

where $\sigma(A_{i,blank})$ and $\sigma(A_{i,tissue})$ are the standard deviations of the average signal amplitudes in each sub-section for images with no target and images of porcine tissue, respectively. Sectioning was used to diminish the contribution of speckle to the CNR while obtaining an adequate number of averages. Either 9 (porcine tissue) or 16 (phantom) sub-regions—based on the size of the ROI—were used to calculate CNR. Each sub-region was approximately 0.66 mm^2. These measurements are of particular interest when quantifying a contrast agent's capabilities in a biological environment[2–4].

Photoacoustic and ultrasound images of the PAnDs before and after vaporization in *ex vivo* porcine tissue are shown in Fig. 3.7. The highest PA signal—which is emitted as a result of droplet vaporization—occurs immediately after the application of pulsed laser light at t = 0.5 s. Subsequent PA signal results from thermal expansion of the gold nanorods and is much lower than signal from vaporization. In addition, an increase in US echogenicity persists following droplet vaporization. Quantitative measurements of

contrast and CNR in the ROI are given in Table 3.2, which were calculated using Equations 3.4-3.7.

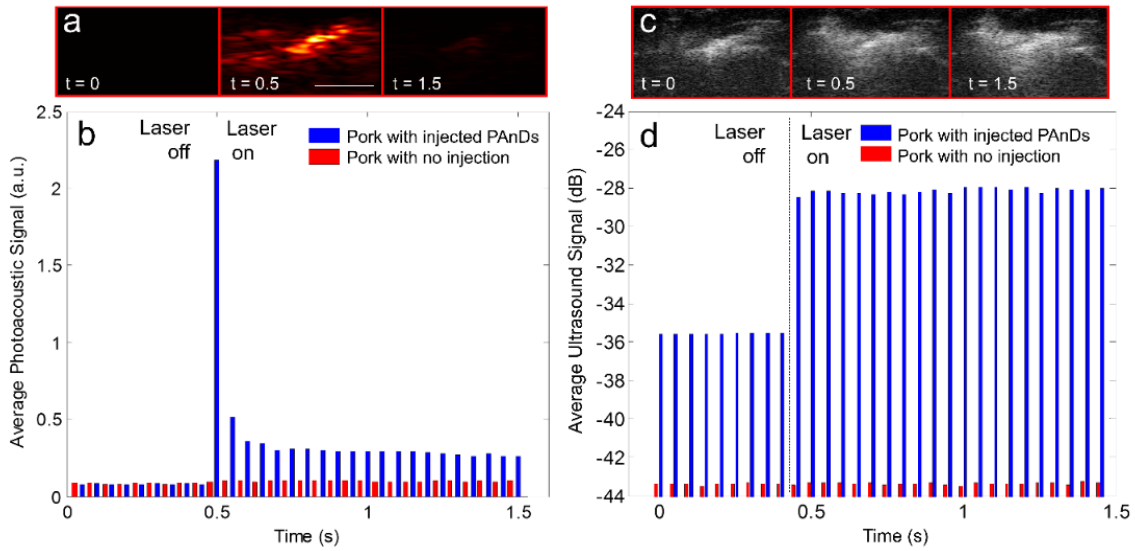

Figure 3.7: (a) Photoacoustic images of *ex vivo* porcine tissue injected with PAnDs, imaged before and during pulsed laser irradiation. Scale bar = 5 mm. (b) Average PA signal over time for native tissue and tissue injected with PAnDs. (c) Ultrasound images of the same tissue sample imaged before and during laser irradiation. Scale bar = 5 mm. (d) Average US echogenicity over time for PAnD injected tissue.

Ultrasound echogenicity is enhanced by the activation of PAnDs into bubbles upon pulsed laser irradiation, resulting in high local contrast and CNR both in a phantom and in *ex vivo* settings. The porcine tissue exhibits little native US contrast; however, local contrast is increased 18 times in the presence of bubbles, while the CNR doubles. The tissue provides nearly zero endogenous PA signal, but the contrast and CNR increase dramatically upon vaporization of the PAnDs.

	$Contrast_{abs}$	CNR_{abs} (dB)	$Contrast_{local}$	CNR_{local} (dB)
	Ultrasound Signal			
Native porcine tissue	1.56	23	21	37
Bubbles in polyacrylamide phantom	31	44	21	29
Bubbles in porcine tissue	28	48	10	29
	Photoacoustic Signal			
Native porcine tissue	N/A	N/A	N/A	N/A
PAnD vaporization in porcine tissue	38	50	38	50
Thermal expansion in porcine tissue	3.2	27	3.2	27

Table 3.2: Contrast and contrast-to-noise ratio for various samples measured with and without PAnDs.

3.4 Conclusions

The development of a functional nanoconstruct made entirely of biocompatible materials is shown here, which enhances contrast in PA and US images in response to an external optical trigger. The PA and US signal generation from the developed nanoconstructs and several control nanodroplets was measured. Additionally, a photoacoustic nanodroplet capable of vaporization using 1064 nm pulsed laser irradiation has been developed. Using a mask, localized droplet activation at 37 °C was shown, indicating that the droplets are stable in the body and activated only upon external trigger. Then an *ex vivo* porcine tissue sample was used to demonstrate the signal and contrast enhancement of US and PA signal, which was quantified. These nanodroplets have

potential for imaging of dense tissue for tumor location using an inexpensive light source and can act as a triggered drug delivery vehicle for therapeutic purposes.

3.5 References

1. Du, Y. *et al.* Optical properties of porcine skin dermis between 900 nm and 1500 nm. *Phys. Med. Biol.* **46,** 167 (2001).
2. Prince, J. L. & Links, J. *Medical Imaging Signals and Systems*. Prentice Hall (2005).
3. Oppelt, A. *Imaging Systems for Medical Diagnostics: Fundamentals, Technical Solutions and Applications for Systems Applying Ionizing Radiation, Nuclear Magnetic Resonance and Ultrasound*. John Wiley & Sons (2011).
4. Webb, A. & Kagadis, G. C. Introduction to biomedical imaging. *Med. Phys.* **30,** 2267 (2003).

Chapter 4: Properties that Influence Optical Droplet Vaporization

As synthesized for the reported studies, the perfluoropentane PAnDs are in a liquid, but superheated form in their native state. Many factors influence the phase of the droplet as well as its tendency to undergo a liquid-to-gas phase change. These factors can be divided into properties of the droplets themselves, and properties of the environment; both will be discussed in detail. By exploring these properties, the formulation of PAnDs can be optimized for a biomedical setting, improving stability and maximizing image contrast.

4.1 Properties of the Droplet

4.1.1 Size

The hydrophobic nature of the PFC causes it to separate from water when the two liquids are mixed. Normally, because surface tension energetically favors a minimal surface area contact between a hydrophobic substance and water, the PFC will coalesce into a single bolus within the water. The addition of a surfactant, however, changes the chemistry and physics of the emulsion. The surfactant contains a hydrophilic head and hydrophobic tail. By coating the hydrophobic phase of the emulsion, the surfactant provides a stable interface between the hydrophobic PFC droplet and the surrounding water. When an emulsion of PFC in water containing a surfactant is agitated, the PFC disrupts into small droplets, which are stable due to the surfactant and do not coalesce. By varying the surfactant and the amount and type of energy used to disrupt the emulsion, the average size of PFC droplets can be altered.

The size of a PFC droplet has a profound effect on its stability in a liquid state, which is due to the Laplace pressure exerted by the water onto the droplet, defined as

$$\Delta P = P_{in} - P_{out} = 2\frac{\gamma}{R} \tag{4.1}$$

where γ is the surface tension at the droplet/water interface, and R is the radius of the droplet[1,2]. As the radius of the droplet decreases, the Laplace pressure increases. This increased Laplace pressure increases the boiling point of the droplet (Fig. 4.1)[3].

For the purposes of an injectable solution for biomedical imaging and therapy, small PFC droplets are desirable for a few reasons. First, small particles can escape leaky blood vessels via the enhanced permeability and retention (EPR) effect, perfusing through tissue more effectively than larger ones, which are confined to the vasculature[4]. This effect allows them to accumulate in tumors.[5] Additionally, ligand density on the nanoparticle surface is increased for small particles, allowing for active targeting[6]. The size of a PFC droplet affects its boiling point, as mentioned above. For example, many PFC emulsions are synthesized from perfluoropentane (PFP), which has a boiling point of 29 °C in its bulk phase. However, in their small droplet form, with the elevated Laplace Pressure, their boiling point can be elevated to over 80 °C (Fig. 4.1)[3].

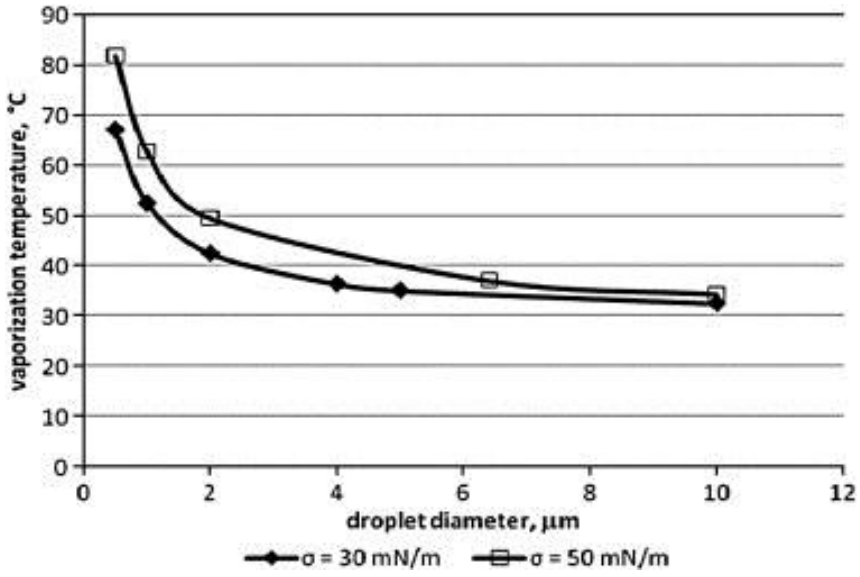

Figure 4.1: Droplet vaporization temperature as a function of droplet size for the surface tension values of 30 mN m^{-1} and 50 mN m^{-1}.

Due to their increased boiling point, small PFC droplets are less likely to undergo spontaneous vaporization, which would defeat their triggering capability. Also, liquid nanodroplets have a substantially higher lifetime in the body than gas bubbles, likely due to gas diffusion from the core[7]. If particles spontaneously vaporize, the time for imaging decreases. Lastly, the shelf life of smaller droplets is increased due to the increased stability.

A drawback of small PFC droplet size is that they are less sensitive to vaporization than their larger counterparts. When the boiling point is vastly increased, a great deal of energy (thermal and/or mechanical) is required to induce vaporization. This limits the depth at which the particles can be activated using a safe dose of energy. For this reason, a tradeoff exists between the perfusion ability of very small droplets (<100 nm) and the high vaporization sensitivity of larger droplets. Because small particles are generally preferred as an injectable construct, it is desirable to find an efficient method of droplet vaporization, so a small droplet can be synthesized and also triggered using safe energy levels.

Although some methods using microfluidics have been reported which can synthesize monodisperse PFC droplets, these methods are typically low-yield and can only produce droplets several microns in diameter[8–10]. To make droplets smaller, bulk PFC in the presence of a surfactant is ultrasonically agitated, either with an immersion bath sonication system or a probe sonicator. While this method produces droplets in the nano size range, the particles are polydisperse, ranging from 100-2000 nm in diameter (Fig. 2.3b). Some methods, such as centrifugation[11] or extrusion[12] can decrease the size dispersity of particles, but these processes can be cumbersome and decrease the yield of particles. Groups have researched the production of monodisperse, submicron PFC

droplets using microfluidics to create a PFC bubble and then condensing them into a smaller liquid droplet, but considerable complexity is required for this synthesis[13,14].

Due to the wide range of nanodroplet diameters within a given sample, the sensitivity to vaporization of each droplet can vary greatly. For the largest droplets, low laser fluence levels are required to induce vaporization, whereas for the smallest particles, much greater fluence is needed. For example, in a polydisperse sample, the largest 10% of the droplets may vaporize at a fluence of 10 mJ cm^{-2}, whereas this energy is insufficient to vaporize anything smaller, due to the increased Laplace pressure and thus droplet boiling point. At a fluence of 40 mJ cm^{-2}, 50% of the droplets may vaporize, leaving the rest in a liquid state. It may take 100 mJ cm^{-2} to vaporize an entire population of droplets within a sample, specifically those less than 100 nm in diameter. Measuring a threshold value for a single droplet with a known size usually requires optical observation methods[15,16].

To determine the threshold laser fluence for visualizing the vaporization of our synthesized optically triggerable PFP nanodroplets, a phantom of nanodroplets was constructed and imaged with US while irradiating it with increasing levels of optical energy. While keeping all other variables constant, the laser fluence irradiating a phantom was varied to determine the threshold for US visualization of PAnD vaporization. The experimental design was similar to that in Fig. 3.4a, with two major differences: the sample was not moved during laser irradiation and US data were collected immediately before, during and after irradiation. The concentration of droplets within the phantom was approximately 10^7 droplets/mL, decreased in this experiment to reduce US signal from nanodroplets prior to vaporization, providing a clear distinction for detecting vaporization threshold.

Image data from each sample was divided into two frames, before and after irradiation. For each of these frames, the following metrics were calculated:

$$signal\ (dB) = \sum_{pixels\ in\ ROI} 20 * log_{10}(A) \tag{4.2}$$

and

$$\Delta\ signal\ (dB) = signal_{after\ irradiation} - signal_{before\ irradiation} \tag{4.3}$$

where A is the linear US amplitude at a given pixel in the image. To quantify the difference in US signal after vaporization, Δ *signal* was plotted as a function of laser fluence, including 0 mJ cm^{-2} (i.e. no laser irradiation) to show noise of the measurement.

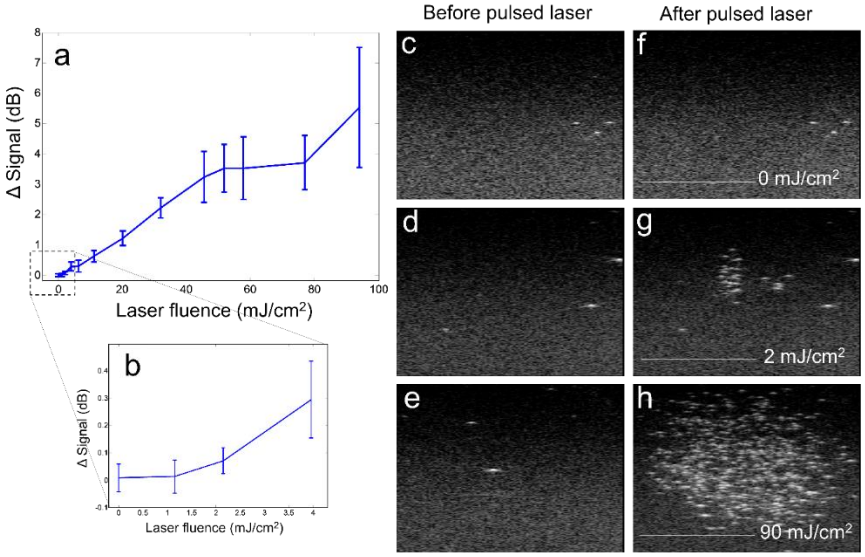

Figure 4.2: (a) Ultrasound signal difference as a function of laser fluence. (b) Ultrasound signal difference at low laser fluences, demonstrating the fluence at which measurable vaporization is detected. (c-e) Droplet-laden polyacrylamide construct before pulsed laser irradiation. (f-h) Construct after irradiation at various fluences, showing droplet vaporization. Images displayed on a 50 dB scale. Scale bar = 5 mm.

Irradiation of the phantom at increasing levels of fluence results in the vaporization of more droplets, and thus greater increases in echogenicity, which is quantified in Fig. 4.2a and 4.2b and shown visually from ultrasound images before laser irradiation in Fig. 4.2c-4.2e, and after irradiation in Fig. 4.2f-4.2h. This sample of droplets ranges from 200 to 800 nm in diameter. At low laser fluence, only the largest droplets vaporize, because they require the least energy to undergo phase change. At higher fluence, the smaller droplets vaporize as well. To determine the threshold for vaporization that is detectable by US in these conditions, the change in US signal was calculated at various fluence levels, and the threshold was considered to be the fluence at which a significant change in echogenicity is measured. In these conditions, a minimum fluence of 4 mJ cm^{-2} was necessary to induce vaporization that results in a detectable change in US signal, shown in Fig. 4.2b.

4.1.2 Type of Perfluorocarbon (Boiling Point)

It has been shown that the size of the droplet has a profound effect on its vaporization sensitivity and thus imaging depth. Another feature of PFC nanodroplets which affects their imaging properties is the type of perfluorocarbon used to synthesize the droplets. Namely, the length of the fluorocarbon chain influences the boiling point. Three commonly used PFCs used to synthesize US contrast agents for medical applications are perfluorobutane (C_4F_{10}, boiling point = -1 °C), perfluoropentane (C_5F_{12}, boiling point = 29 °C), and perfluorohexane (C_6F_{14}, boiling point = 56 °C) (Fig. 4.3). It is expected that lower boiling point droplets experience a lower vaporization threshold at the expense of stability. Higher boiling point droplets, while easy to synthesize and stable at physiological temperatures, will require substantial energy to induce vaporization.

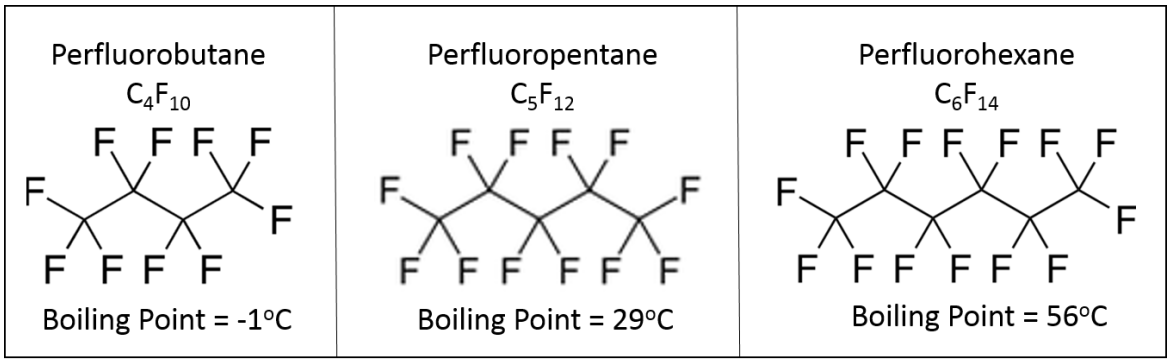

Figure 4.3: Molecular structures of perfluorocarbons used to create nanodroplets used in these studies.

The US and PA imaging properties of PFC droplets with different boiling points was investigated. First, US echogenicity was measured for three different samples of droplets using a solution of droplets in a pipette and irradiated with a pulsed laser, as shown in Fig. 3.1a. The linear US intensity before and after lasing are shown in Fig. 4.4.

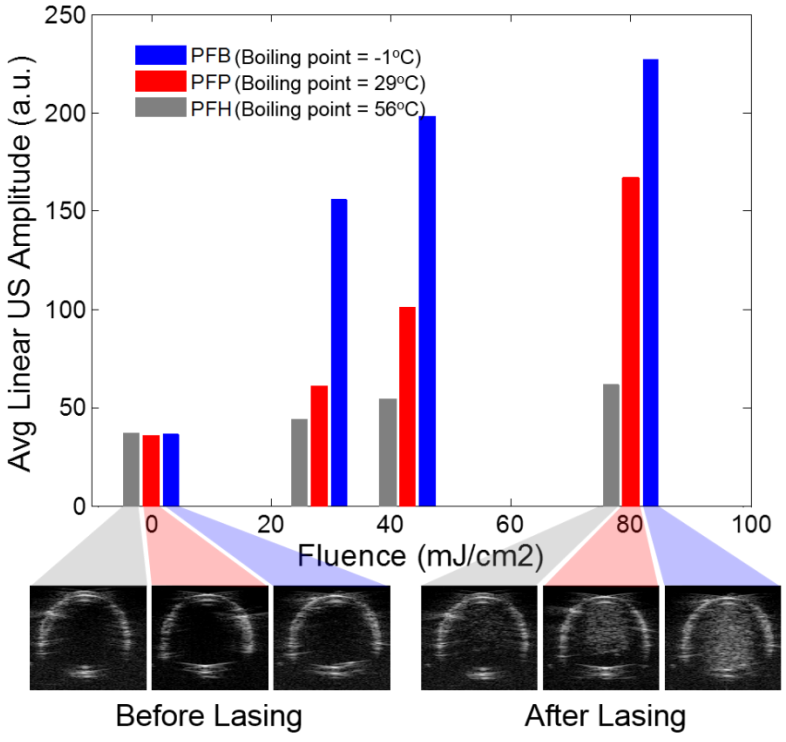

Figure 4.4: Ultrasound signal from vaporization of PFC nanodroplets using PFCs of varying boiling points.

There are a few notable results from the data in Fig. 4.4. First, for a given type of PFC, as the laser fluence increases, US echogenicity increases. This is the same trend seen in Fig. 4.2—that is, the smaller (higher boiling point) droplets vaporize only at higher laser fluence levels. Second, for a given laser fluence, lower boiling point droplets become more echogenic than higher boiling point droplets upon activation. For example, at 40 mJ cm^{-2}, nearly all of the PFB droplets vaporize in response to the laser; a smaller percentage of the PFP droplets vaporize at this fluence; and very few PFH droplets vaporize. Lastly, it seems that even at high fluence, very few of the PFH droplets vaporize. To investigate this further, and to observe PA behavior, the same three samples were embedded in polyacrylamide phantoms and imaged with US and PA techniques over a period of 10 seconds using the Vevo 2100 imaging system and pulsed laser light delivered through two fiber bundles, depicted in Fig. 4.5.

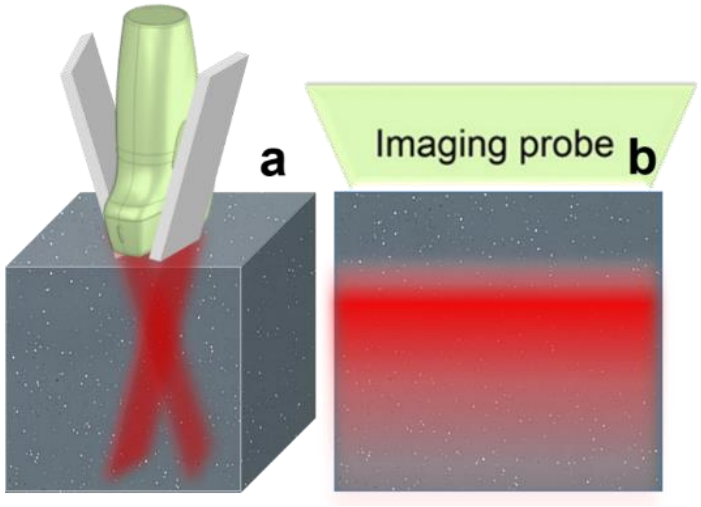

Figure 4.5: (a) Droplet-laden phantom irradiated with a pulsed laser while imaged using ultrasound and photoacoustic techniques. (b) Imaging plane, where red color indicates region of overlapping optical beams and thus highest energy.

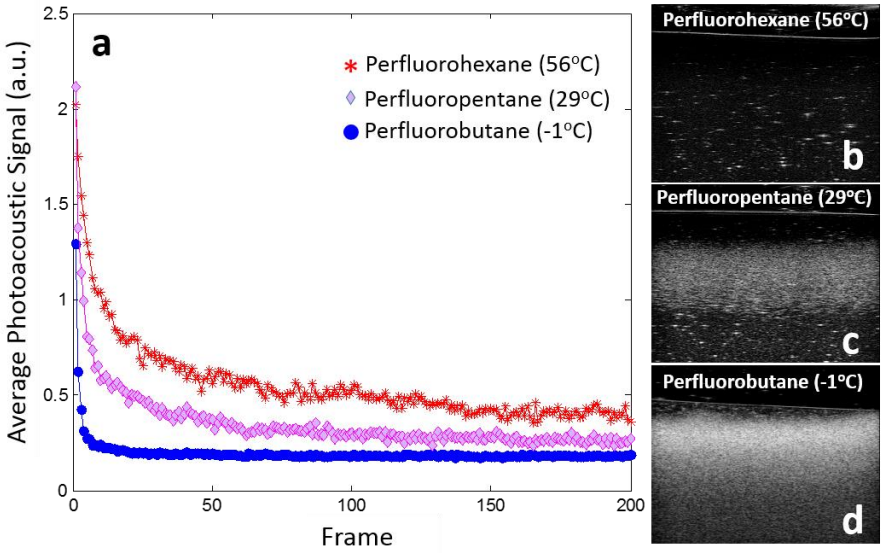

Figure 4.6: (a) Average photoacoustic signal as a function of time and frame for phantoms containing PAnDs made with various boiling point PFCs. (b) Ultrasound contrast following laser irradiation of perfluorohexane, (c) perfluoropentane, and (d) perfluorobutane PAnDs.

Figure 4.6a shows the PA intensity as a function of time from each phantom. From previous experiments, it seems that the greatest PA signal follows the first laser pulse, due to vaporization of the particles. This is followed by a rapid decay, where some remaining particles vaporize on subsequent pulses. Finally, the PA signal falls to a steady floor, representing signal from thermal expansion of the photoabsorber.

Figure 4.6b-d shows the phantoms after irradiation at a fluence of 20 mJ cm^{-2}. The trend in vaporization efficiency is consistent with the particles in solution. However, the PFH droplets exhibit no increase in echogenicity, indicating that they did not vaporize.

The behavior of different boiling point droplets follows some expected trends, but also raises some questions. First, upon the initial laser pulse, there is no significant difference in PA signal among the different types of droplets. However, when comparing the US contrast, there is a significant increase in contrast from the PFB droplets, indicating

more vaporization. It was initially believed that the vaporization of the droplets corresponded to the initial PA signal. However, further investigation explains why the US signal shown in Fig. 4.6b does not correspond with the PA signal in Fig. 4.6a.

The US images from Figure 4.6b-d were collected simultaneously with PA data at a frequency of 20 frames/second, corresponding to the laser pulse repetition frequency. While the vaporization of PFP and PFB droplets can be seen in US images at this frame rate, the images of the PFH droplet-laden phantom, when viewed at 20 frames/s, suggest that no vaporization is occurring, while the PA signal shows strong signal normally associated with vaporization.

To investigate, the same PFH phantom was irradiated with a pulsed laser at 2 pulses/second, while imaged with US at 580 frames/second. Figure 4.7a shows the average linear US amplitude of the phantom over time, and Fig. 4.7b shows US images of the phantom. While the images in Fig 4.6b suggest that PFH droplets do not vaporize, the data at high frame rates show spikes in US echogenicity, followed by decay toward baseline, which repeats at the rate of the laser pulse repetition frequency. This suggests that the PFH droplets are undergoing repeatable vaporization, a phenomenon first reported by Asami et al[17]. This finding might explain the presence of PA signal in the absence of lasting US contrast enhancement, and has many potential applications for contrast agent development, explored in Chapter 5.

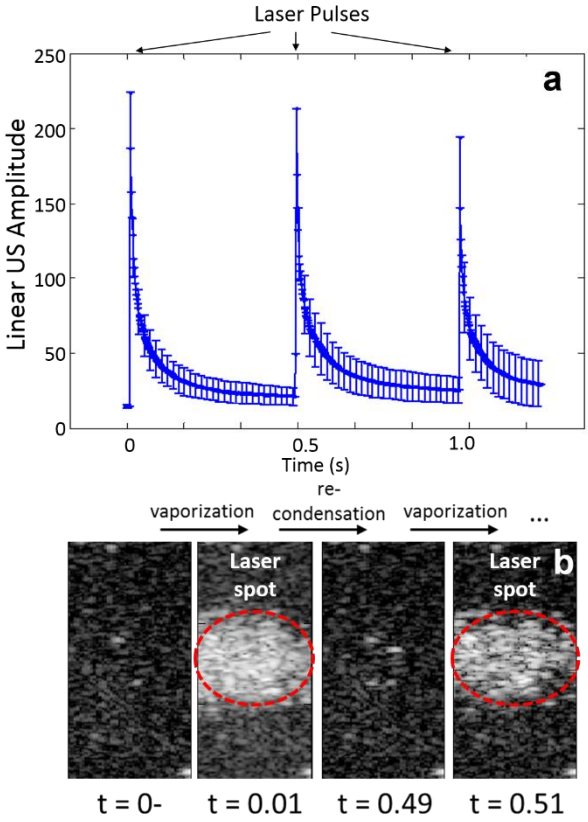

Figure 4.7: (a) Ultrasound signal over time from a droplet-laden phantom irradiated with 3 laser pulses. (b) Ultrasound images of the phantom before, during and between laser pulses.

4.1.3 Optical Absorption

Another factor of the PAnDs that influence their vaporization sensitivity is the amount of optical energy they can absorb and convert to heat and mechanical energy; this largely depends on the optical absorption coefficient of the droplets. This coefficient can be increased by the type of dye or nanoparticle, or the amount of encapsulated absorber in each PFC droplet. When no absorber is included in the sample, laser irradiation is unable to induce vaporization, as shown in the samples of blank nanodroplets (Fig. 3.2, 3.3). In response to increasing the amount of photoabsorber in the droplet sample, it is hypothesized that the vaporization efficiency of the particles will increase rapidly, resulting

in increased US contrast and PA signal from the initial laser pulse. However, at some degree of loading, the vaporization efficiency will be maximized, and the addition of more dye or nanoparticles will not increase vaporization efficiency further.

When measuring PA signal, it should be noted that the signal from the first laser pulse comes from two sources: 1) the vaporization of the PFC droplet, and 2) thermal expansion of the encapsulated photoabsorber. Therefore, once the particles are saturated with photoabsorber, adding more dye or gold nanoparticles will still increase the PA signal, but only by an amount corresponding to thermal expansion of more particles, and not from more vaporization. The vaporization provides signal upwards of 10x greater than signal from thermal expansion (Fig. 3.3), so once the signal from vaporization has reached maximum efficiency, the extra increase in PA signal should be only 10% as quick as the increase when vaporization efficiency was increasing.

To test this hypothesis, a series of PFP nanodroplet samples was synthesized, to which an increasing number of fluorinated gold nanorods was added. The samples were imaged within a pipette using US and PA methods, (Fig. 3.1a).

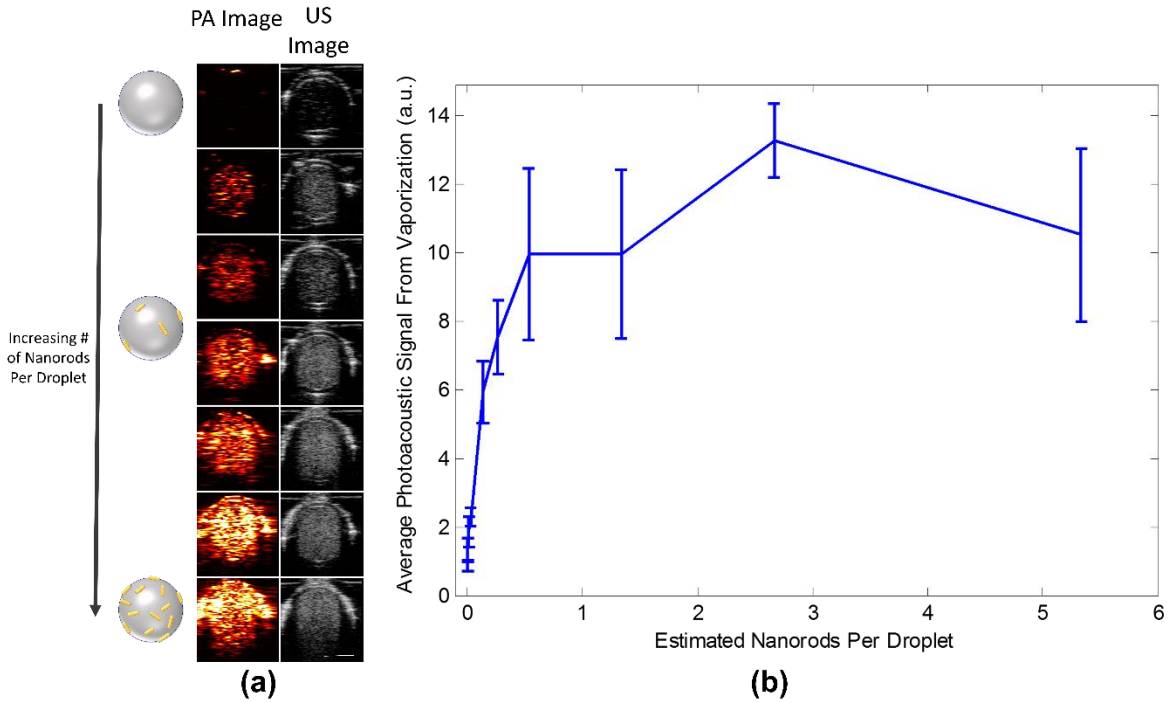

Figure 4.8: (a) Droplet samples with increasing loading of nanorods. PA images resulting from droplet vaporization, and US images from the bubbles. (b) Average PA signal from droplet vaporization, plotted as a function of nanorod loading. Scale bar = 2 mm.

Figure 4.8a shows the PA and US images immediately following the initial laser pulse, and Figure 4.8b shows the average PA signal within the tube following the first laser pulse. As expected, there is initially a rapid increase in PA signal as the number of nanorods in the sample increases. Eventually the PAnDs are "saturated" with gold nanorods—that is, the sample contains approximately 1 gold nanorod per droplet. Once this state is achieved, further increasing the number of nanorods per droplet does not increase the PA signal from the initial laser pulse. It was hypothesized the adding more nanorods would still increase the signal, due to thermal expansion. However, because signal from thermal expansion is so much lower than from vaporization (at this laser fluence), the extra thermal expansion signal is not detectable above the noise of the measurements (Fig. 4.8b). A more precise measurement scheme must be devised to test this hypothesis. It should also be noted

that during the process of modifying the surface of the gold nanorods to bind to the nanodroplets, there is substantial aggregation and loss of particles. Because of this, the number of nanorods per droplet is a gross estimation.

4.1.4 Shell Material (Stiffness)

Another parameter which may affect the PFC droplet vaporization sensitivity is the material used as a surfactant, or shell of the droplet. Materials such as bovine serum albumin (BSA), lipid cocktails, and polymers have all been used in this project to synthesize PFC droplets. Each of these materials confers different properties, most notably stiffness, which may affect vaporization threshold. The shell material also affects droplet size and dispersity, as well as the ability of gas to diffuse across the membrane, which affects bubble lifetime. While these have not been studied explicitly for effect on optical droplet vaporization thresholds, several studies report thresholds for acoustic droplet vaporization, which varies with shell material. For example, Sheeran et al report a vaporization threshold of 3.35 MPa for lipid shelled PFB droplets[18]. For a lipid shelled PFP droplet, Schad & Hynynen report a threshold of 4 MPa[15], whereas Lo et al report a threshold of 5 MPa for an albumin shelled particle[19]. Reznik et al report a threshold of 1.6 MPa for PFP droplets with a Zonyl FSO shell[16], suggesting that this material may increase vaporization sensitivity. Additionally, the shell stiffness has been studied and reported for bubble oscillation[20,21], and "it is possible that the stiffness, fluidity or surface tension of the shell will presumably affect the vaporization process through changes to the Poisson pressure inside the droplet/bubble."[15]

4.2 Properties of the Environment

In addition to the properties of the PAnDs that determine their sensitivity to vaporization, several properties of the environment contribute to their liquid-to-gas phase

change. Most notably, the temperature, elasticity of the surrounding medium, interstitial pressure, laser fluence for activation, and external US field intensity have measurable effects on droplet vaporization. Several of these are explored in detail, with implications for making biomedical measurements.

4.2.1 Laser Fluence

Because the main mechanism for droplet vaporization in the studies reported here is absorption of optical energy and conversion to heat and pressure, a given sample of droplets has a laser fluence threshold for vaporization, which may depend on a variety of factors discussed here. A study was performed in which increasing levels of fluence were used to irradiate a phantom, and the change in US signal was recorded after each irradiation. Figure 4.2 shows the results of this experiment, and for the purposes of visualizing bubbles with a clinical US system, the minimal local fluence required to induce vaporization of PAnDs was determined to be approximately 4 mJ cm^{-2}.

It should be noted that 4 mJ cm^{-2} is the *local* laser fluence required to induce vaporization. In biomedical applications, light must travel through human tissue before reaching the PAnDs, undergoing scattering and absorption due to various endogenous chromophores[22,23]. This absorption by blood is possibly the greatest limitation to any light-based applied imaging or therapeutic tool[24]. Therefore it is of great interest to increase the sensitivity of the PAnDs to vaporization as much as possible.

4.2.2 Stiffness/Elasticity of the Environment

In section 4.1.1, it was stated that the local pressure within a droplet has a profound effect on its vaporization threshold, which is influenced by droplet size. A feature of the environment which has the same effect is stiffness. As the stiffness of the surrounding

environment increases, it is hypothesized that it is more difficult for a liquid droplet to expand into a gaseous bubble 5x larger in diameter. To test this effect, a polyacrylamide tissue-mimicking phantom was synthesized, whose background contained 10% acrylamide, yielding a shear modulus of ~5 kPa ; a cylindrical inclusion in the phantom contained 45% acrylamide for a shear modulus of ~20 kPa[25–27]. The background was made to mimic the stiffness of healthy tissue, while the inclusion mimicked a tumor's stiffness. The entire phantom was embedded with PFP PAnDs. The experimental design is depicted in Fig. 4.9a, and the imaging plane is depicted in Fig. 4.9b. A pulsed laser irradiated the sample via fiber bundles. Ultrasound image data of the phantom was collected before (Fig. 4.9c) and after (Fig. 4.9d) laser irradiation.

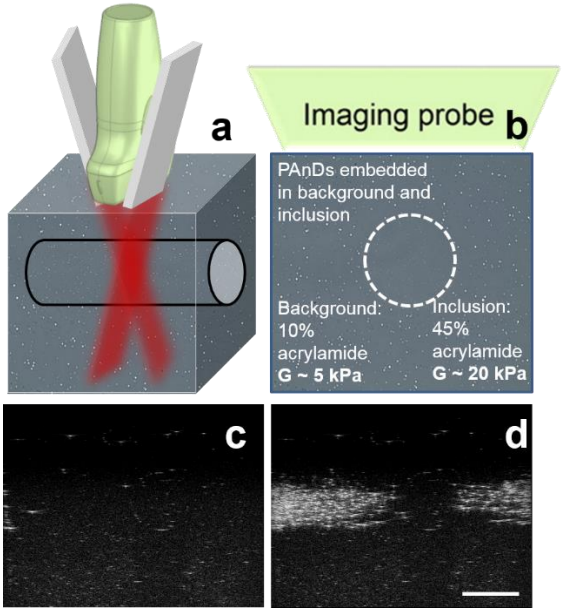

Figure 4.9: (a) Tissue-mimicking phantom embedded with PAnDs, with soft background and stiff inclusion imaged by US probe. (b) Diagram of imaging plane with inclusion surrounded by background. (c) Ultrasound image of phantom before laser irradiation. (d) Ultrasound image of phantom after laser irradiation. Scale bar = 5 mm.

The stiff inclusion impedes droplet vaporization, or induces rapid recondensation of the droplets following the laser pulses. By increasing the laser fluence used to irradiate the phantom, vaporization was induced in both the soft background and the stiff inclusion, indicating that the droplets within the inclusion were not defunct, but instead their vaporization was impeded by the phantom's mechanical properties at a lower fluence.

To quantify the effect of stiffness on droplet vaporization and recondensation, two separate phantoms made of polyacrylamide were synthesized, with shear moduli of 5 and 30 kPa to mimic healthy and cancerous tissues[28,29]. The phantoms were embedded with PFH nanodroplets, which recondense after vaporization at body temperature. Each phantom was irradiated by a pulsed laser while being imaged with US at a rate of 580 frames/s.

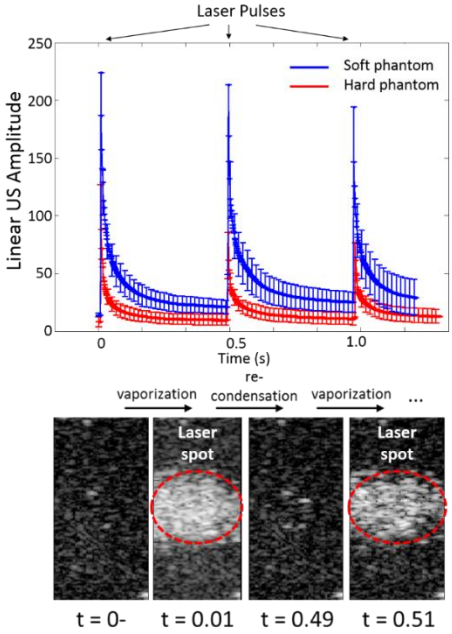

Figure 4.10: (a) Linear ultrasound amplitude over time and three laser pulses for nanodroplets in a hard and soft phantom. (b) Ultrasound images of the nanodroplets before, during, and after laser irradiation.

The average linear US amplitude of the irradiated phantom is shown over time in Fig. 4.10. The soft phantom, shown in blue, experiences a greater increase in US echogenicity than the hard phantom following the first laser pulse. This is likely due to increased vaporization efficiency in the sample. This particular laser fluence is sufficient to vaporize a greater subset of droplets (large and small) in a soft environment, whereas only a small subset (the largest droplets) vaporize in a stiffer environment.

Because the droplets have a much higher boiling point than the background temperature, the bubbles recondense after vaporization. And because the environments differ in stiffness, the rate at which the bubbles recondense differs between a hard and soft phantom, giving another method to potentially discriminate healthy from diseased tissue.

The US amplitude data in Fig. 4.10 was fit to a power function, and the coefficient and exponential term were extracted to differentiate hard and soft phantoms. The data from the experiment reported in Fig. 4.10 was fit to a power function,

$$y = Ax^{-B} \tag{4.4}$$

where y is the linear US amplitude, x is time, and A and B are coefficients fitting the decay. To discern hard from soft phantoms, the coefficients were plotted together and displayed in Fig. 4.11. It was observed that the power function coefficient was significantly greater for the equations in the soft phantoms than for the hard ones, but the decay exponent was not significantly different for the two phantoms. This means that in this experiment, the total increase in echogenicity in response to a laser pulse depended on stiffness. However, the decay time for US echogenicity was not significantly different, so stiffness did not affect recondensation time.

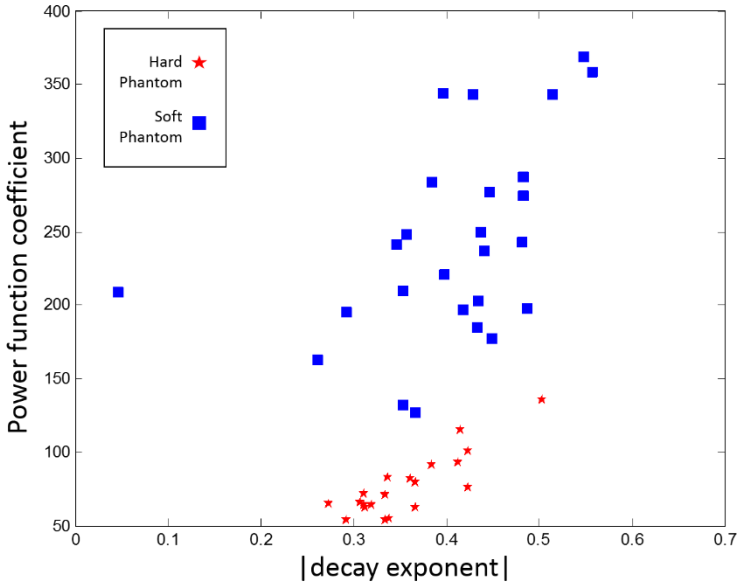

Figure 4.11 Power function coefficient plotted vs decay exponent for the curves of US echogenicity in hard and soft phantoms.

4.2.3 Interstitial Pressure

In addition to stiffness, pressure of the surrounding medium has an effect on droplet vaporization dynamics. It is documented that tumor regions experience elevated interstitial pressure relative to the surrounding healthy tissue[30,31], which was hypothesized would impede droplet vaporization and/or hasten the recondensation of bubbles once vaporized, similar to the effect of size on increased Laplace pressure. To test this, PAnDs were injected into a dialysis tube inside a water tank, which was closed on one side and connected to a tank of carbon dioxide, whose pressure could be adjusted manually, as shown in Fig. 4.12. The droplets were irradiated with a laser and simultaneously imaged with US at a high frame rate.

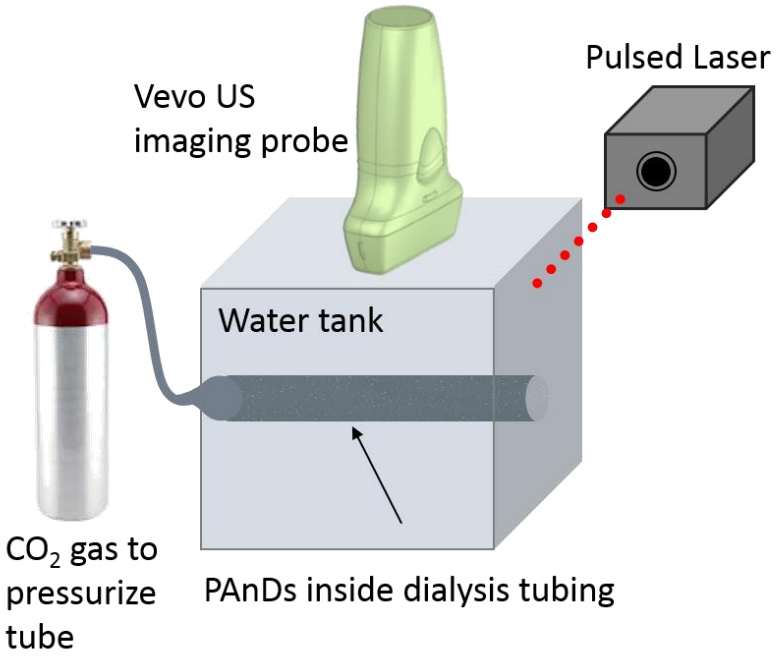

Figure 4.12: PAnDs inside a pressurized tube, irradiated with a pulsed laser and imaged with high frame rate ultrasound.

The US intensity for various pressures is shown in Fig. 4.13a, and US images during irradiation are shown in Fig. 4.13b. As expected, increasing the pressure results in decreased vaporization efficiency (lower peaks) as well as more rapid vaporization (signal decays back to baseline more quickly).

The differences in vaporization kinetics are most pronounced between 1 and 5 pounds per square inch (psi). Pressures measured in this experiment were much greater than values of interstitial pressure reported for healthy and cancerous tissues, which vary between 0.05 and 0.29 psi. Because of this, discerning between tissues would require a precise measurement. It is more likely that other factors, such as tissue stiffness, would have a greater effect on vaporization and recondensation.

The behavior of the PAnDs in solution in the dialysis tube differed from that of the PAnDs embedded in a phantom. When the PAnDs were in solution, rather than embedded

in a phantom, there was a cumulative increase in US echogenicity over time, most notably at low pressure. This is likely because the phantom physically impedes bubble formation more than the liquid environment. To ensure that droplet vaporization is repeatable over many laser pulses, it is important to use a laser fluence which his high enough to induce brief, but not stable, vaporization. This balance is also discussed in the work by Asami et al[17].

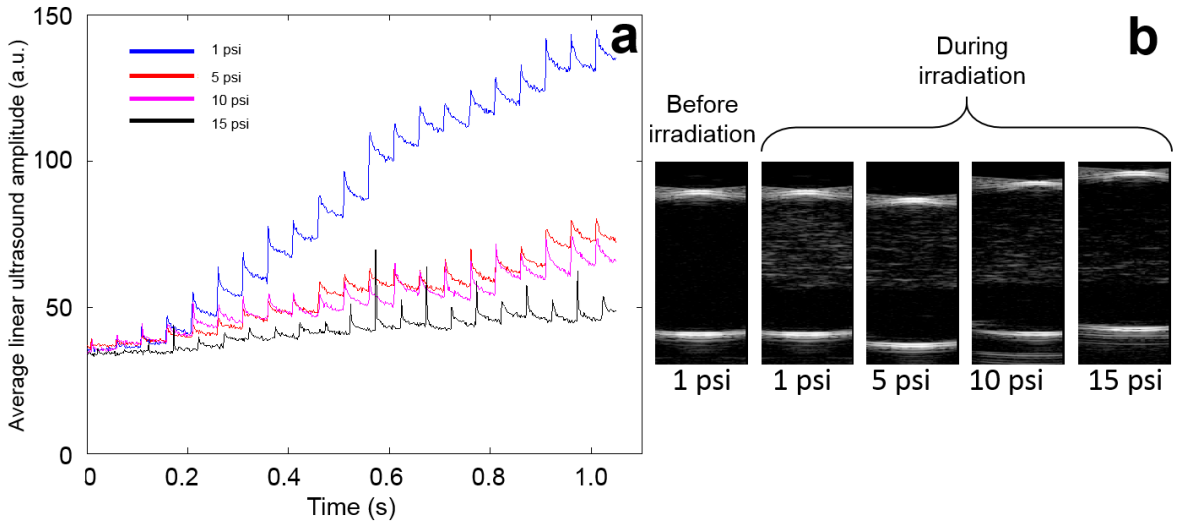

Figure 4.13 (a) Linear US signal within the tube over time and several laser pulses for various levels of pressure. (b) US images of the tube cross section after irradiating under various pressures.

Ideally, by formulating a droplet which is sensitive to repeatable vaporization/condensation cycles, combined with measuring the dynamics of their US echogenicity, this imaging technique may be used to map the interstitial pressure and elastic modulus of potentially cancerous regions, outlining tumor boundaries inside otherwise healthy tissue.

4.2.4 External Temperature

Another variable which affects droplet vaporization is external temperature, which has a similar effect to PFC boiling point. Samples of ICG-loaded droplets and of blank droplets in aqueous ICG were imaged using PA and US techniques at three different temperatures: room temperature (23 °C) to observe the effect of irradiation on droplets well below their boiling point; body temperature (37 °C) to study biologically relevant conditions; and 50 °C to observe the effects of further superheating the droplets. Photoacoustic images and signal averages at all temperatures are shown in Fig. 4.14. The PA signal from ICG-loaded droplets over time (Fig. 4.14a) is accompanied by images from the first laser pulse for each temperature (Fig. 4.14c). At increased temperatures, the nanodroplets produce greater PA signal upon vaporization. For the blank droplets in aqueous ICG, there was no detectable PA signal at any temperature. This is also confirmed from the US data in Fig. 4.15. Because of the acoustic shadowing at 50 °C, there is greater signal variance within the frame than at 37 °C. This increase in "noise" artificially decreases the CNR for the 50 °C case.

Each sample contained droplets ranging in diameter from approximately 200 nm up to 1 μm, and the Laplace pressure on a small droplet may significantly increase its boiling point. At lower temperatures, the laser fluence is insufficient to vaporize all (i.e. the smaller) droplets. At higher temperatures, the PFC is superheated and volatile, so a laser pulse of the same fluence vaporizes a greater percentage of the irradiated droplets, producing a higher average PA signal. Alternatively, volume or rate of particle expansion during irradiation is greater at increased temperatures, inducing stronger PA signal. This increased signal at high temperatures can be exploited to maximize contrast using this imaging technique. To do so, factors such as the type of PFC (and thus boiling point),

droplet size and shell stiffness, and laser fluence may be adjusted. It is noted that at 50 °C, the PA signal is small but detectable (i.e. above the noise level of the system) during the subsequent laser pulses, while at other temperatures the PA signal is detected from only the first pulse. At 50 °C, surrounding droplets in aqueous solution are likely to enter the imaging plane due to flow caused by vaporization. These introduced droplets undergo vaporization, prolonging the elevated PA signal in the subsequent pulses. This is also evident in a movie showing vaporization at high temperature, which is available from the author upon request. However, it is unlikely to be a significant phenomenon in clinical imaging conditions if the nanodroplets are imaged outside of the vascular compartments. This phenomenon was also explored by Reznik et al with regard to ultrasound triggered droplet vaporization, and similar conclusions were made[32].

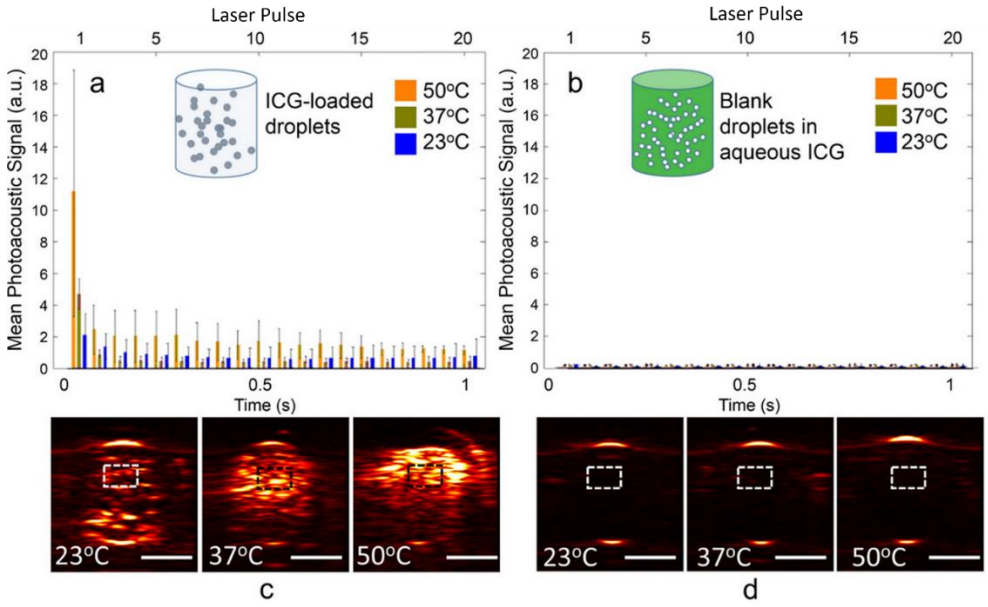

Figure 4.14: (a) Average PA intensity in the ROI from ICG-loaded droplets, and (b) from blank droplets in aqueous ICG over 20 laser pulses and equivalent time. (c) Photoacoustic images of the pipette cross section after the first laser pulse, observed at three temperatures, from ICG-loaded droplets and (b) from blank droplets in aqueous ICG. Error bar represents 1 standard deviation above and 1 standard deviation below the mean value. $N \geq 3$ for all reported values. Scale bar = 2 mm.

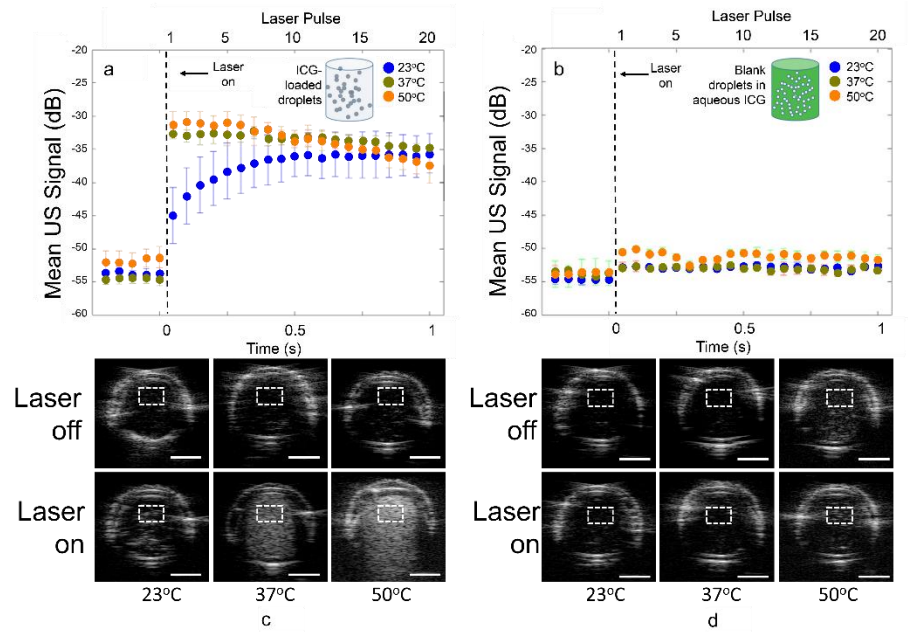

Figure 4.15: (a) Average US signal in the ROI before and after laser irradiation over each pulse and equivalent time from ICG-loaded droplets and (b) from blank droplets in aqueous ICG, displayed on a 50 dB scale. (c) Ultrasound images at three temperatures before and during laser irradiation from ICG-loaded droplets and (d) from blank droplets in aqueous ICG. Error bar represents 1 standard deviation above and 1 standard deviation below the mean value. $N \geq 3$ for all reported values. Scale bar = 2 mm.

4.2.5 Ultrasound Pressure Field

One must keep in mind when developing volatile US contrast agents that the particles are constantly in a US pressure field, even at diagnostic levels. This field affects droplet vaporization and recondensation. The local changes in pressure from a therapeutic or even diagnostic level of US can have a noticeable effect on the vaporization threshold of PAnDs, as well as their condensation kinetics. Many studies have reported using HIFU to induce droplet vaporization, where a local increase in rarefactional pressure induces a phase conversion of the PFC droplet[3,15,16,18,33–35]. In our studies, optical energy is used to induce vaporization, but it is likely that a combination of photothermal energy from laser irradiation and mechanical energy from US imaging contribute to droplet vaporization.

For nanodroplets containing the compounds PFB or PFP, the acoustic vaporization threshold is reported to be anywhere between 1.6 and 5 MPa, depending on insonation time[32], shell material[36], and transducer frequency[34]. It has been shown that vaporization thresholds are lower for higher frequency US insonation[15,37,38]. Because diagnostic US imaging can induce pressure levels on the order of 0.5 MPa, and because diagnostic US is generally in the range of 5 MHz or greater, the acoustic pressure from the imaging transducer should be considered when inducing optical vaporization.

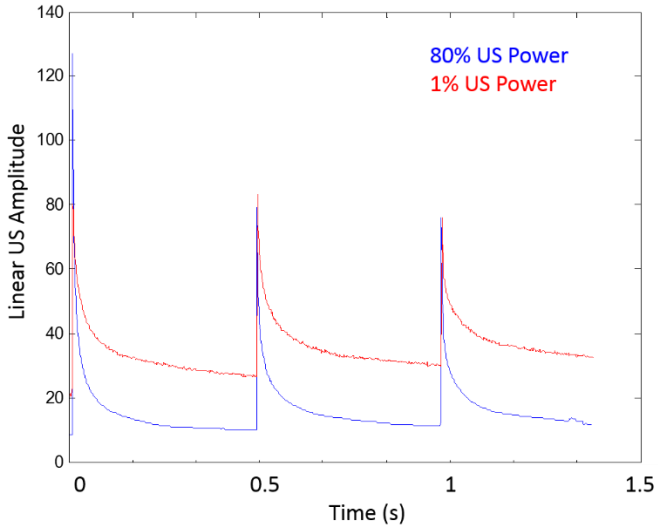

Figure 4.16: Average linear ultrasound amplitude of a droplet-laden phantom imaged at high frame rate while irradiating with pulsed laser. Ultrasound imaging was conducted at two pressure levels.

Figure 4.16 shows the average linear US amplitude of a phantom loaded with PFH droplets, which was irradiated to induce repeated vaporization. As the US power is increased, the US signal decays more quickly, and the US signal following recondensation is lower. This is likely due to more rapid recondensation of bubbles in the presence of a strong US field. It should be noted that the baseline level of US echogenicity is lower for

higher US power, which is noted by the US amplitude before the first laser pulse. However, accounting for this, the rate of recondensation is still greater for higher power US.

4.2.6 Concentration of Droplets

The local concentration of PFC nanodroplets may affect the vaporization sensitivity. Reznik et al measured the acoustic pressure threshold to vaporize samples of droplets at various concentrations (10^6, 10^7, 10^8, and 10^9 droplets/mL) (Fig. 4.17)[32]. It was reported that higher concentrations vaporized at lower pressures, which is in agreement with findings by Zhang and Porter[39]. This is possibly due to a higher probability of nucleation within the total PFC volume, or greater presence of larger (easier to vaporize) PFC droplets. It was also hypothesized that an increased concentration led to greater heating of the sample, which decreased the energy required to vaporize them.

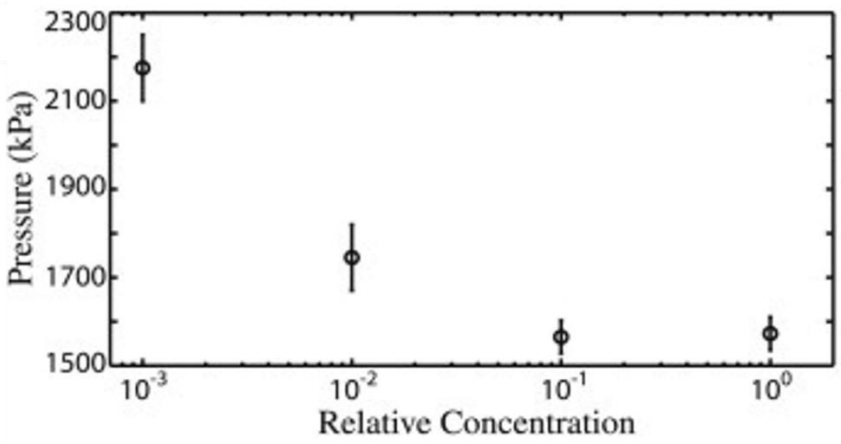

Figure 4.17 Vaporization pressure threshold measurements as a function of relative droplet concentration. There is a decrease in vaporization threshold pressure associated with elevation of this parameter. Each point represents the mean value ± the standard error over 10 trials.

4.2.7 Heating or Pressure (Length of Laser Pulse)

Determining the mechanism of optical droplet vaporization is an area of great interest[17,40,41], because it would broaden our knowledge of PAnD behavior and help to improve their properties for increased sensitivity and stability. Much research has been conducted on acoustic droplet vaporization, and theories about how HIFU induces vaporization include heating, rarefactional pressure, and inertial cavitation[16,19,42,43]. Fewer experiments have been able to elucidate the mechanisms of optical induced vaporization.

An overarching question posed regarding the behavior is "Is heating causing the droplets to vaporize, or is a photoacoustic pressure wave inducing the vaporization of superheated particles?"

A few experiments have been conducted by us to possibly elucidate this mechanism. A phantom embedded with droplets sensitive to light at 1064 nm was irradiated using two different 1064 nm lasers: a continuous wave (CW) laser, and a pulsed laser. According to photoacoustic theory, the pulsed laser will induce PA signal from the optical absorber, given its sufficiently short pulse length, which will bring about thermal expansion. However, the CW laser will only bring about heating of the optical absorber. Because the deposition of heat is not concentrated into a short time, thermal and stress confinement are not achieved (Section 1.4), so no pressure waves will be generated. If the CW laser can induce vaporization, it could be concluded that induction of a pressure wave is not necessary for droplet vaporization.

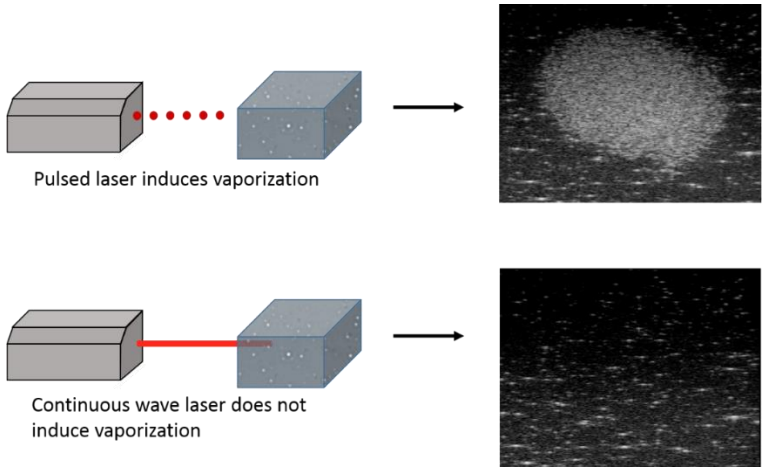

Figure 4.18: Effect of pulsed and continuous wave laser irradiation on a droplet-embedded phantom.

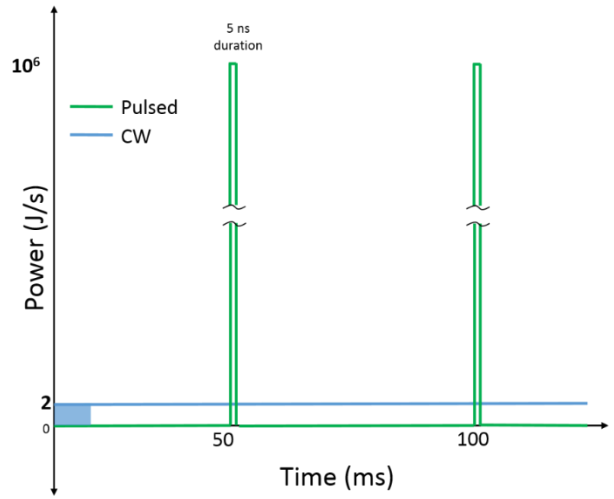

Figure 4.19: Laser power as a function of time for the continuous-wave and pulsed lasers used in the experiments described, highlighting the differences between the two lasers in energy deposition over time.

After irradiation of the phantom, it was concluded that the CW laser did not vaporize the PFC droplets, even after 15 minutes of irradiation (Fig. 4.18). Unfortunately, because the temporal deposition of energy into the phantom and thus thermal gradients is so different between the two cases, it cannot be concluded that a PA wave is necessary for vaporization (Fig. 4.18). The pulsed laser delivers an energy payload of 20 mJ in one pulse,

and one pulse is sufficient to induce droplet vaporization. The continuous wave laser, which operates at 2 W, achieves 20 mJ in 10 ms. While the pulsed laser has an "average" power of only 0.4 W, all of this energy is concentrated into 5 ns pulses, whereas the continuous wave laser spreads out its energy over time (Fig. 4.19).

An infrared camera was used to measure the temperature increase at the surface of the phantom during continuous wave irradiation. Measuring the surface of the phantom, the maximum temperatures achieved were 52 °C, (5 minutes), 60 °C (10 minutes), and 65 °C (15 minutes). Similar temperature measurements were made in the phantom when irradiated with a pulsed laser. There was no measurable increase in temperature over 10 pulses. However, the temporal frame rate of the IR camera is much slower than the 5 ns pulse width of the laser, so it is likely that any temperature increase was quickly dissipated and not detectable by the camera.

One group achieved "opening of hollow capsules" with a CW laser, however, their capsules are comprised of a hollow polymer sphere, so this mechanism may be entirely different than from PFC particles[44]. Lajoinie et al studied laser activated vaporization of hexadecane microcapsules, and they concluded that heating induced vaporization[45].

4.3 Conclusions

After many experiments, it is concluded that the following parameters have measurable influence on the optically triggered phase change of PFC droplets: droplet size, laser fluence, type of PFC (boiling point), amount and type of photoabsorber (optical absorption), elasticity of the medium, pressure of the medium, external temperature, US pressure field, and length of the laser pulse. Additional parameters which may affect triggered vaporization, but were not measured by us directly, are the droplet shell material, and the concentration of droplets. Controlling the properties of the nanodroplets will have

a profound effect on their stability and sensitivity, yielding a robust imaging contrast agent that is optimized for imaging at great depth. Additionally, by understanding how the droplets react to irradiation in their environment, information about the perfused tissue can be obtained for noninvasive diagnosis.

4.4 References

1. Butt, H.-J., Graf, K. & Kappl, M. *Physics and Chemistry of Interfaces*. John Wiley & Sons (2006).
2. De Gennes, P. G., Brochard-Wyart, F. & Quéré, D. *Capillarity and Wetting Phenomena - Drops, Bubbles, Pearls, Waves*. Springer (2004).
3. Rapoport, N. Y., Kennedy, A. M., Shea, J. E., Scaife, C. L. & Nam, K.-H. Controlled and targeted tumor chemotherapy by ultrasound-activated nanoemulsions/microbubbles. *J. Controlled Release* **138**, 268–276 (2009).
4. Prabhakar, U. *et al.* Challenges and key considerations of the enhanced permeability and retention effect for nanomedicine drug delivery in oncology. *Cancer Res.* **73**, 2412–2417 (2013).
5. Fang, C. *et al.* In vivo tumor targeting of tumor necrosis factor-α-loaded stealth nanoparticles: Effect of MePEG molecular weight and particle size. *Eur. J. Pharm. Sci.* **27**, 27–36 (2006).
6. Albanese, A., Tang, P. S. & Chan, W. C. W. The effect of nanoparticle size, shape, and surface chemistry on biological systems. *Annu. Rev. Biomed. Eng.* **14**, 1–16 (2012).

7. Lentacker, I., De Smedt, S. C. & Sanders, N. N. Drug loaded microbubble design for ultrasound triggered delivery. *Soft Matter* **5**, 2161–2170 (2009).

8. Martz, T. D., Sheeran, P. S., Bardin, D., Lee, A. P. & Dayton, P. A. Precision manufacture of phase-change perfluorocarbon droplets using microfluidics. *Ultrasound Med. Biol.* **37**, 1952–1957 (2011).

9. Martz, T. D., Bardin, D., Sheeran, P. S., Lee, A. P. & Dayton, P. A. Microfluidic generation of acoustically active nanodroplets. *Small* **8**, 1876–1879 (2012).

10. Seo, M., Gorelikov, I., Williams, R. & Matsuura, N. Microfluidic assembly of monodisperse, nanoparticle-incorporated perfluorocarbon microbubbles for medical imaging and therapy. *Langmuir* **26**, 13855–13860 (2010).

11. Weers, J. G. & Arlauskas, R. A. Particle size analysis of perfluorocarbon emulsions in a complex whole blood matrix by sedimentation field-flow fractionation. *Colloids Surf. B Biointerfaces* **33**, 265–269 (2004).

12. Giesecke, T. & Hynynen, K. Ultrasound-mediated cavitation thresholds of liquid perfluorocarbon droplets in vitro. *Ultrasound Med. Biol.* **29**, 1359–1365 (2003).

13. Tan, Y. C. & Lee, A.P. Microfluidic separation of satellite droplets as the basis of a monodispersed micron and submicron emulsification system. *Lab on a Chip* **5**, 1178–1183 (2005).

14. Sang, Y. Y. *et al*. A microfluidic technique for generating monodisperse submicron drops. *RSC Adv.* **3**, 2330–2335 (2013).

15. Schad, K. C. & Hynynen, K. In vitro characterization of perfluorocarbon droplets for focused ultrasound therapy. *Phys. Med. Biol.* **55**, 4933 (2010).

16. Reznik, N. *et al.* The efficiency and stability of bubble formation by acoustic vaporization of submicron perfluorocarbon droplets. *Ultrasonics* **53**, 1368–1376 (2013).

17. Asami, R. & Kawabata, K. Repeatable vaporization of optically vaporizable perfluorocarbon droplets for photoacoustic contrast enhanced imaging. *Ultrasonics Symposium (IUS), 2012 IEEE International* 1200–1203 (2012).

18. Sheeran, P. S., Luois, S., Dayton, P. A. & Matsunaga, T. O. Formulation and acoustic studies of a new phase-shift agent for diagnostic and therapeutic ultrasound. *Langmuir* **27**, 10412–10420 (2011).

19. Lo, A. H., Kripfgans, O. D., Carson, P. L., Rothman, E. D. & Fowlkes, J. B. Acoustic droplet vaporization threshold: effects of pulse duration and contrast agent. *IEEE Trans. Ultrason. Ferroelectr. Freq. Control* **54**, 933–946 (2007).

20. Hoff, L., Sontum, P. C. & Hovem, J. M. Oscillations of polymeric microbubbles: effect of the encapsulating shell. *J. Acoust. Soc. Am.* **107**, 2272–2280 (2000).

21. Sboros, V. Response of contrast agents to ultrasound. *Adv. Drug Deliv. Rev.* **60**, 1117–1136 (2008).

22. Mourant, J. R., Fuselier, T., Boyer, J., Johnson, T. M. & Bigio, I. J. Predictions and measurements of scattering and absorption over broad wavelength ranges in tissue phantoms. *Appl. Opt.* **36**, 949–957 (1997).

23. Bashkatov, A. N., Genina, E. A., Kochubey, V. I. & Tuchin, V. V. Optical properties of human skin, subcutaneous and mucous tissues in the wavelength range from 400 to 2000 nm. *J. Phys. Appl. Phys.* **38**, 2543 (2005).

24. Xu, X., Wang, R. K., Elder, J. B. & Tuchin, V. V. Effect of dextran-induced changes in refractive index and aggregation on optical properties of whole blood. *Phys. Med. Biol.* **48**, 1205 (2003).

25. Yeung, T. *et al.* Effects of substrate stiffness on cell morphology, cytoskeletal structure, and adhesion. *Cell Motil. Cytoskeleton* **60**, 24–34 (2005).

26. Saha, K. *et al.* Surface creasing instability of soft polyacrylamide cell culture substrates. *Biophys. J.* 99, L94–L96 (2010).

27. Fischer, R. S., Myers, K. A., Gardel, M. L. & Waterman, C. M. Stiffness-controlled three-dimensional extracellular matrices for high-resolution imaging of cell behavior. *Nat. Protoc.* **7**, 2056–2066 (2012).

28. Parker, K. J., Huang, S. R., Musulin, R. A. & Lerner, R. M. Tissue response to mechanical vibrations for 'sonoelasticity imaging'. *Ultrasound Med. Biol.* **16**, 241–246 (1990).

29. Lawrence, A. J. Palpating breast cancer by magnetic resonance elastography. *Proc. ISMRM* (1999).

30. Curti, B. D. Physical barriers to drug delivery in tumors. *Crit. Rev. Oncol. Hematol.* **14**, 29–39 (1993).

31. Heldin, C.-H., Rubin, K., Pietras, K. & Östman, A. High interstitial fluid pressure — an obstacle in cancer therapy. *Nat. Rev. Cancer* **4**, 806–813 (2004).

32. Reznik, N., Williams, R. & Burns, P. N. Investigation of vaporized submicron perfluorocarbon droplets as an ultrasound contrast agent. *Ultrasound Med. Biol.* **37**, 1271–1279 (2011).

33. Dayton, P. A. *et al.* Application of ultrasound to selectively localize nanodroplets for targeted imaging and therapy. *Mol. Imaging* **5**, 160–174 (2006).

34. Kripfgans, O. D., Fowlkes, J. B., Miller, D. L., Eldevik, O. P. & Carson, P. L. Acoustic droplet vaporization for therapeutic and diagnostic applications. *Ultrasound Med. Biol.* **26**, 1177–1189 (2000).

35. Kripfgans, O. D., Miller, D. L., Fowlkes, J. B. & Carson, P. L. Vaporization of micrometer size droplets in simulated in vivo environments. *J. Acoust. Soc. Am.* **106**, 2191–2191 (1999).

36. Moncion, A., Kripfgans, O. D., Carson, P. L., Fowlkes, J. B. & Fabiilli, M. L. Characterization of acoustic droplet vaporization and inertial cavitation thresholds in acoustically-responsive tissue scaffolds. *Ultrasonics Symposium (IUS), 2014 IEEE International* 1646–1649 (2014).

37. Kripfgans, O. D., Fowlkes, J. B., Woydt, M., Eldevik, O. P. & Carson, P. L. In vivo droplet vaporization for occlusion therapy and phase aberration correction. *IEEE Trans. Ultrason. Ferroelectr. Freq. Control* **49**, 726–738 (2002).

38. Sheeran, P. S., Luois, S. H., Mullin, L. B., Matsunaga, T. O. & Dayton, P. A. Design of ultrasonically-activatable nanoparticles using low boiling point perfluorocarbons. *Biomaterials* **33**, 3262–3269 (2012).

39. Zhang, P. & Porter, T. An in vitro study of a phase-shift nanoemulsion: a potential nucleation agent for bubble-enhanced HIFU tumor ablation. *Ultrasound Med. Biol.* **36**, 1856–1866 (2010).

40. Wilson, K., Homan, K. & Emelianov, S. Biomedical photoacoustics beyond thermal expansion using triggered nanodroplet vaporization for contrast-enhanced imaging. *Nat. Commun.* **3**, 618 (2012).

41. Strohm, E., Rui, M., Gorelikov, I., Matsuura, N. & Kolios, M. Vaporization of perfluorocarbon droplets using optical irradiation. *Biomed. Opt. Express* **2**, 1432–1442 (2011).

42. Fabiilli, M. L. *et al.* The role of inertial cavitation in acoustic droplet vaporization. *IEEE Trans. Ultrason. Ferroelectr. Freq. Control* **56**, 1006–1017 (2009).

43. Rapoport, N. Y., Efros, A. L., Christensen, D. A., Kennedy, A. M. & Nam, K.-H. Microbubble generation in phase-shift nanoemulsions used as anticancer drug carriers. *Bubble Sci. Eng. Technol.* **1**, 31–39 (2009).

44. Sukhorukov, G. B. *et al.* Nanoengineered polymer capsules: tools for detection, controlled delivery, and site-specific manipulation. *Small* **1**, 194–200 (2005).

45. Lajoinie, G. *et al.* Ultrafast vapourization dynamics of laser-activated polymeric microcapsules. *Nat. Commun.* **5**, (2014).

Chapter 5: Blinking Phase-Change Nanocapsules (BLInCs) Enable Background-Free Ultrasound Imaging

Despite the high echogenicity of microbubbles, or even the triggerable contrast of liquid PFC nandroplets, local image contrast is still limited by the vast number of sub-wavelength acoustic scatterers that exist in most tissues. To combat this issue, several functional agents and nonlinear imaging techniques have been implemented. Harmonic and pulse inversion imaging utilize the nonlinear oscillatory behavior of microbubbles in response to US irradiation, which can be used to distinguish them from the background tissue[1,2]. However, a high concentration of bubbles is needed and contrast is limited due to the nonlinear response from tissue[3,4]. Thus an imaging strategy to further improve the contrast from injected nanoparticles is desirable. Any strategy to image injected particles and suppress background requires detecting a property of the particles that is not detected from the background. This is where traditional B-mode US imaging fails, because many tissue scatterers reflect sound similarly to injected bubbles. To improve image contrast, an optically activated particle has been developed, termed blinking nanocapsule (BLInC), along with an image processing algorithm, to conduct background free imaging of the nanoparticles.

5.1 BLInking nanoCapsules

The design of BLInCs is rooted in the high boiling point of perfluorohexane (56 °C) compared to body temperature, rendering them capable of repeated vaporization/condensation cycles, a phenomenon first reported by Asami et al[5]. Due to the acoustic impedance difference between liquid and gas, the US echogenicity of BLInCs can change temporarily, and we have developed an algorithm for a background-free image of the particles using only a laser and a US imaging system. The BLInCs, depicted in

Fig. 5.1a, consist of a liquid perfluorohexane (PFH) core, resulting in a stable liquid nanodroplet at physiological temperatures. The BLInCs are bound by a Zonyl FSO polymer shell, which lowers the surface tension, yielding particles smaller in size than microbubbles[6] and preventing their coalescence. The BLInCs are further stabilized by the Laplace pressure between the PFH core and the surrounding water due to their small size[7]. The BLInCs encapsulate an Epolight™ 3072 near infrared absorbing dye (Fig 5.1b), enabling specific optical activation at the peak absorption wavelength of the dye.

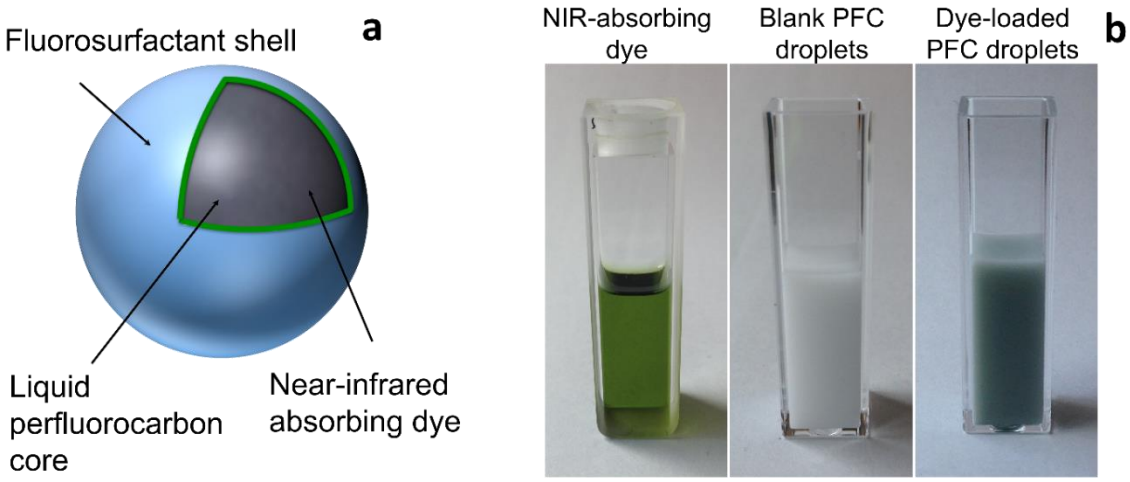

Figure 5.1: (a) Depiction of the nanodroplets, consisting of a perfluorohexane core surrounded by a Zonyl FSO fluorosurfactant polymer shell and encapsulating an optically absorbing dye. (b) Photographs of the dye (left), the blank perfluorocarbon nanodroplets (middle), and the dye-encapsulated nanodroplets (right).

5.2 Response of BLINCs to Laser Pulses

When the BLInCs are imaged, their unique dynamics can be used to differentiate them from background tissue (Fig. 5.2a). In response to pulsed laser irradiation, the encapsulated optical absorber catalyzes a rapid (< 1-2 µs) droplet-to-bubble phase change, a phenomenon reported similarly for particles made of other perfluorocarbons[8–10]. The resulting transient gaseous microbubbles, which persist for several milliseconds,

temporarily enhance the local US contrast before recondensing to their stable nanodroplet form at physiological temperatures (Fig. 5.2a). This entire "blinking" process can be measured using any clinical US imaging system capable of high frame rate imaging (> 400 frames/s) (Fig. 5.2b). The vaporized bubbles and recondensed liquid droplets can also be observed using light microscopy (Fig. 5.2c). When combined with their nano size, the highly dynamic and controllable behavior of the BLInCs enables a wide array of high contrast and molecular US imaging applications.

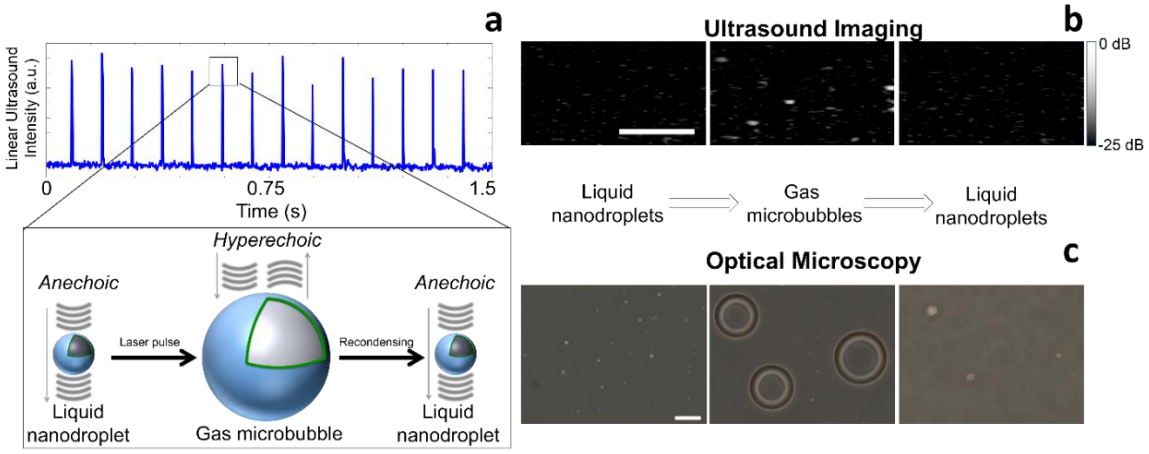

Figure 5.2: (a) US echogenicity as a function of time over 14 laser pulses (top), as a result of repeated activation of the particles, depicted below. (b) Ultrasound images of the nanodroplets in a tissue-mimicking phantom before (left), during (middle), and after (right) laser-induced vaporization. Scale bar = 1 mm. (c) Phase microscopy images of the nanodroplets before (left), immediately after laser irradiation (middle), and after cooling below boiling temperature (right). Scale bar = 20 µm.

5.3 Synthesis of BLINCs

First, 1 mg of Epolight™ 3072 dye (Epolin, Inc.) was added to 300 µL of perfluorohexane (FluoroMed, L.P.) and dissolved by sonication at 180 W for 30 s in a VWR benchtop ultrasonic cleaner. Then 1 mL of 1% v/v aqueous Zonyl FSO fluorosurfactant polymer (Sigma) and 1.7 mL of DI water were added to the PFH. The

mixture was emulsified by vortexing for 10s and sonicated for 2 minutes at 180 W in a VWR benchtop ultrasonic cleaner. The nanodroplets were washed of excess dye and polymer by centrifuging at 1000 rcf for 5 minutes and replacing the supernatant with deionized water. The BLInCs were characterized for optical extinction using UV-Vis spectrometry and for size by dynamic light scattering (Fig. 5.3). Droplet vaporization and recondensation was confirmed using US imaging (Fig. 5.2b) and phase microscopy (Fig. 5.2c).

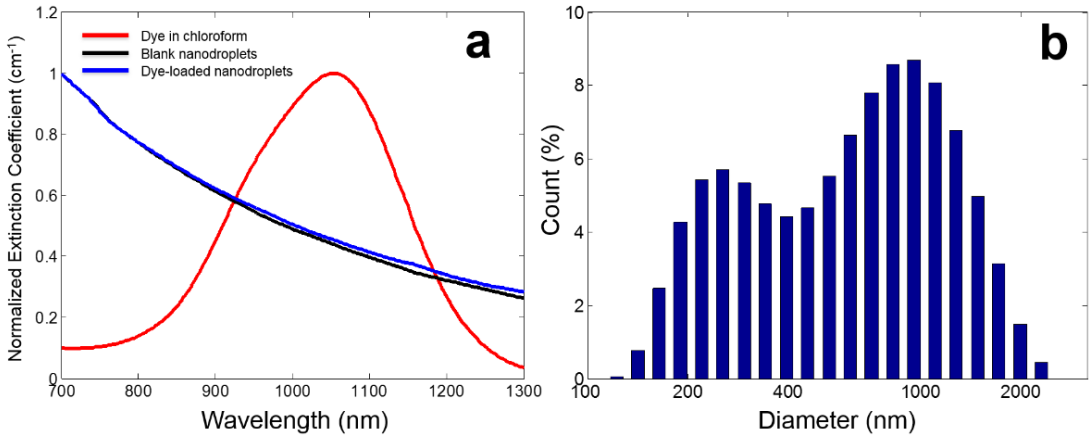

Figure 5.3: (a) Normalized extinction spectra of the near infrared absorbing dye in chloroform, blank perfluorohexane BLInCs, and dye-loaded nanodroplets. (b) Size distribution of the BLInCs.

5.4 Phantom Imaging and Image Processing

To determine if the BLInCs are detectable by a US imaging system among other acoustic scatterers and optical absorbers, the behavior of the particles was observed relative to background in a tissue-mimicking phantom. This would determine if the BLInCs, and not the background, change US intensity in response to pulsed laser irradiation, verifying the specificity of the imaging technique. It would also show if an optically absorbing background induces changes in US echogenicity in response to irradiation in the absence of BLInCs.

A polyacrylamide phantom was created by mixing 64 mL deionized water, 21 mL of 40% acrylamide (Ambion), 850 µL 10% w/v ammonium persulfate (Sigma-Aldrich), and 106 µL of tetramethylethylenedimine (Sigma). Before crosslinking, 0.2% w/v silica particles and 0.01% w/v graphite were added to the phantom solution to scatter US and attenuate light similarly to biological tissue[11]. A 1 mm diameter cylindrical inclusion was embedded in the phantom, identical to the background except for an inclusion of 100x diluted BLInCs, and not containing graphite. The final concentration of nanodroplets in the inclusion was approximately 10^8 particles/mL.

The phantom was imaged using a Vevo 2100 US imaging system, using a 40 MHz array transducer. The phantom was uniformly irradiated by a pulsed laser with light with a wavelength of 1064 nm, while B-mode image data was collected from a cross-section of the cylindrical inclusion at 670 frames per second (Fig. 5.4a). This resulted in a US image of the background with the inclusion cross-section (Fig. 5.4). The fluence of the laser was approximately 40 mJ cm^{-2}. Raw data was collected and further processed using MATLAB.

The traditional B-mode US scans did not reveal distinct differences between the inclusion and the background when viewed in real-time (Fig. 5.4c). A map of the BLInCs was formed by the steps described below, and the map was overlaid on a B-mode US image (Fig. 5.4d). It should be noted that despite optical absorbers and US scattering particles present throughout the volume of the phantom, only the inclusion of perfluorocarbon nanodroplets was identified, demonstrating the specificity of the imaging technique.

To identify the location of the BLInCs, each pixel was evaluated over many frames of a B-mode US movie captured at a frame rate 670 Hz. The US intensities over time of a pixel in the inclusion of BLInCs and a pixel in the background show the difference in behavior between the droplets and the background (Fig. 5.4e). The vaporization events

were highlighted by differentiating the US intensity over time. Positive spikes in differential intensity denote increases in US signal from the droplet-to-bubble conversion, and negative spikes correspond to decreases in US signal from recondensation of the bubbles back into droplets (Fig. 5.4f). Pixels not containing BLInCs, even though equally irradiated by the laser, did not exhibit this behavior. Next, a temporal autocorrelation of the differential US intensity over time was calculated for each pixel (Fig. 5.4g). To form a map of the particles, the ratio of the 2^{nd} highest peak (delay = 0.2s) to the highest peak (delay = 0s) in the autocorrelation was calculated for each pixel based on the appropriate delay. The value of this ratio was then converted to image intensity and overlaid onto a B-mode image (Fig. 5.4d). The delay to be used to calculate the ratio for BLInC signal is based on the US frame rate, the laser pulse repetition frequency, and the length of imaging time. This algorithm would be adjusted if any of these parameters changes, and it could be customized for a given system.

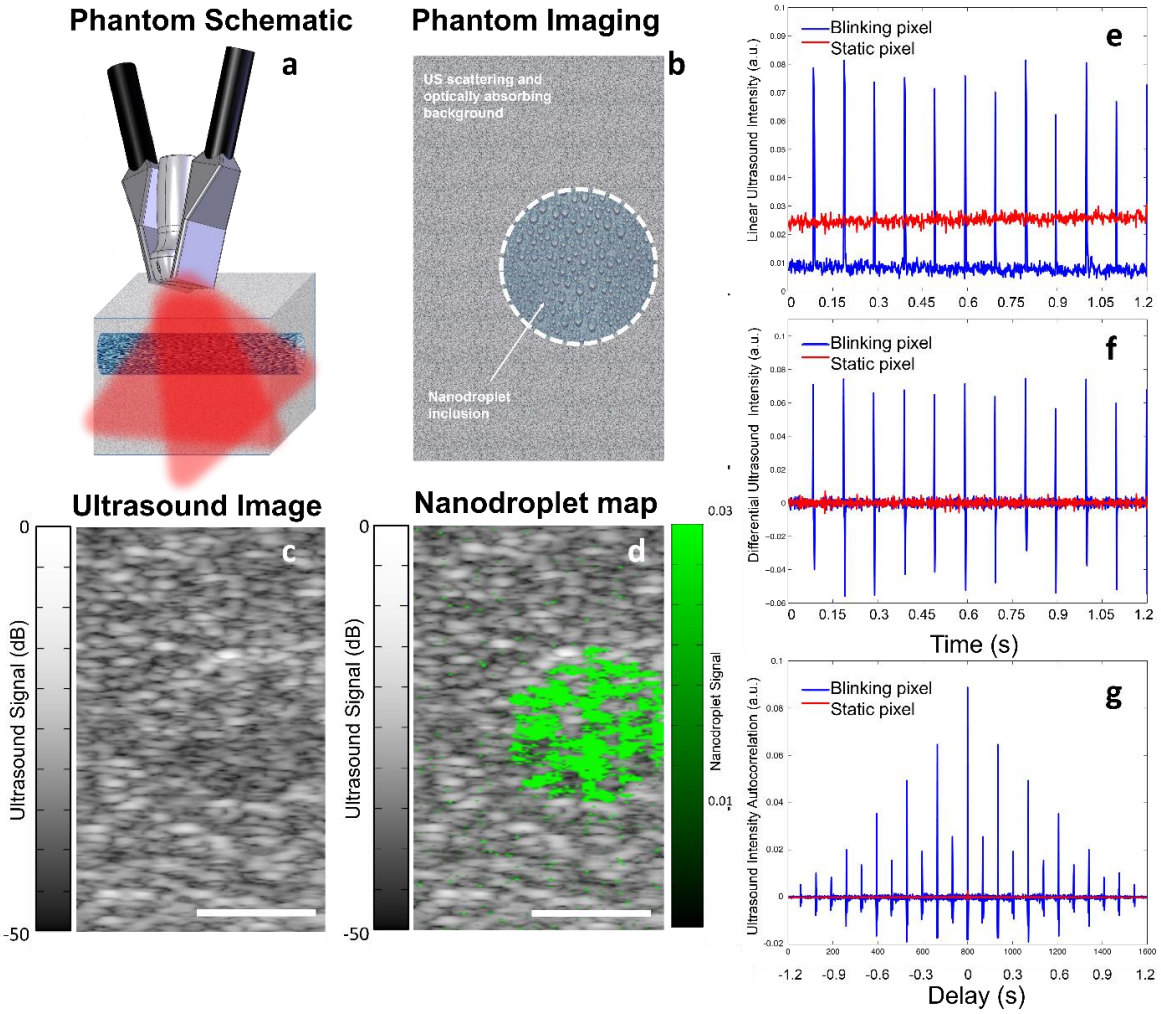

Figure 5.4: (a) Diagram of a tissue-mimicking phantom with inclusion of BLInCs, imaged with a clinical array transducer while irradiated with a pulsed laser. (b) Depiction of a US image of the phantom, indicating areas of BLInC inclusion and background. (c) B-mode US image of the phantom during laser irradiation. (d) Map of BLInCs signal overlaid onto a B-mode image of the phantom, indicating the position of the particles. Scale bars = 1 mm. (e) Linear US intensity of pixels representing a blinking particle (blue) and background (red) in the phantom over time. (e) Derivative of the US pixel intensity for a blinking particle (blue) and background (red). (f) Autocorrelation of the derivative of the US intensity of an individual image pixel representing a blinking particle (blue) and background (red) as a function of delay. Scale bars = 1 mm.

5.5 Imaging of BLInCs in the Lymph Node

In many types of cancer, identifying the first lymph node to which a tumor drains, the sentinel lymph node (SLN), is critical for accurate staging. A mouse model of lymphatic drainage was used to demonstrate the high contrast utility of BLInCs in SLN mapping using US imaging[12]. Although US imaging is routinely used for lymph node imaging, the SLN cannot be identified from anatomy alone. Therefore, an injection of a contrast agent is needed to identify the SLN, and BLInCs can provide higher contrast than traditional microbubbles.

All animal studies were performed under protocols approved by the Institutional Animal Care and Use Committee sat The University of Texas at Austin. A previously developed mouse model of lymph node drainage was used[13,14] in which a nude Nu/Nu mouse (Charles River Laboratories) was injected submucosally into the tongue with the nanodroplets. Prior to injection, the mouse was anesthetized with a combination of isoflurane (1.5%) and O_2 (2 L min^{-1}). The nanodroplets were allowed to drain for 30 minutes at which point US imaging was performed on the cervical lymph nodes located in the mouse's neck. Clear US gel was used for acoustic coupling between the transducer to the mouse. Ultrasound images were acquired with a Vevo 2100 (VisualSonics) using a 40-MHz linear array transducer (MS-550). Light with a wavelength of 1064 nm was generated by a Vibrant Nd:YAG laser (Opotek) operating at 10 Hz and coupled to a custom fiber bundle. The optical fluence irradiating the mouse of approximately 40 mJ cm^{-2} was well below the safety limit of 100 $mJcm^{-2}$ for human skin exposure established by the American National Standards Institute. Immediately following the imaging, the mouse was euthanized via an overdose of isoflurane (5%) and cervical dislocation.

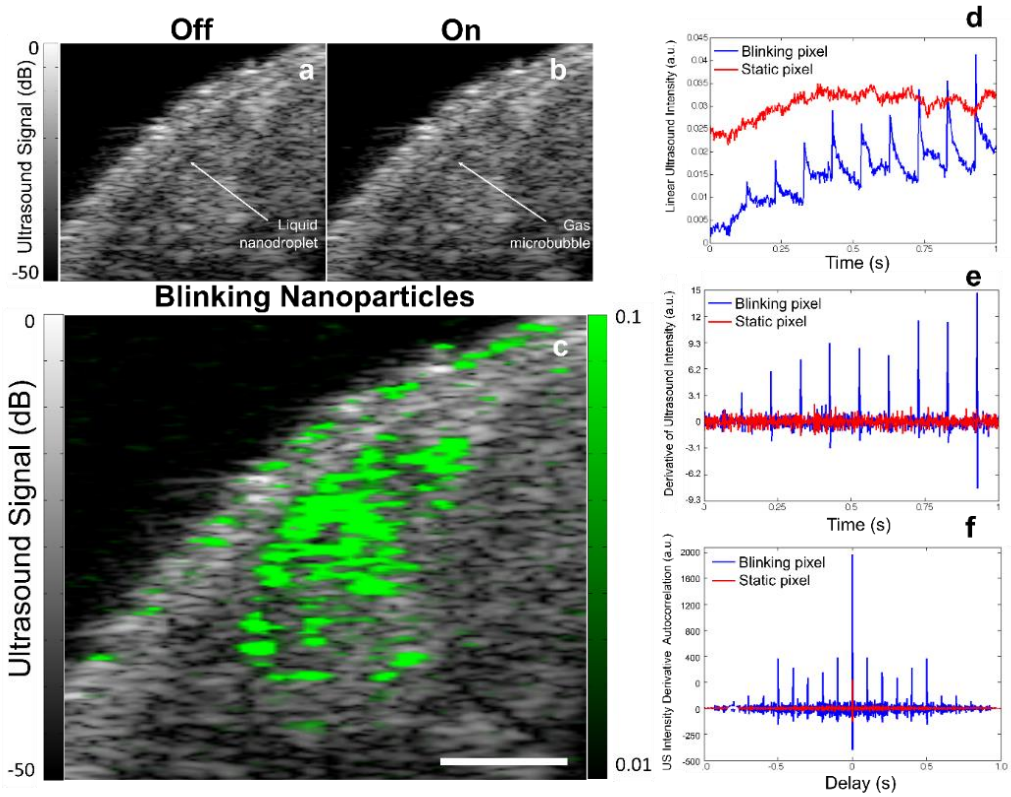

Figure 5.5: (a) Pulse-echo B-mode US image of a mouse lymph node with injected BLInCs before laser irradiation. (b) B-mode US image of a mouse lymph node with injected BLInCs during laser irradiation. (c) B-mode image of the lymph node with overlay of BLInCs location after processing the autocorrelation signal. (d) Linear US intensity of pixels representing a blinking particle (blue) and background (red) in the mouse tissue over time. (e) Derivative of US pixel intensity for a blinking particle (blue) and background (red). (f) Autocorrelation of the derivative of the US intensity of an individual image pixel representing a blinking particle (blue) and background (red) as a function of delay. Scale bars = 1 mm.

While in their native liquid state, the BLInCs do not provide detectable contrast in the SLN 30 minutes after their submucosal injection into the tongue (Fig. 5.5a). Upon pulsed laser irradiation, the particles blink, (Fig. 5.5b); however, it is difficult to see even on a real-time US imaging system, due to the low concentration of bubbles, the highly scattering background, and the rapid recondensation of the BLInCs into their liquid state.

However, the phase change behavior of the BLInCs in the lymph node can be distinguished from background after processing the temporal characteristics of individual image pixels, providing a background free map of the BLInCs which can be overlaid on a US image to visualize them in an anatomical reference (Fig. 5.5c). To obtain the map of the BLInCs, the same algorithm described in section 5.4 was applied (Fig. 5.5d-f).

Next, the drainage kinetics of the BLInCs in the lymph node were observed. Thirty minutes following the injection into the mouse tongue, the lymph node was identified using conventional B-mode US imaging (Fig. 5.6a), and the BLInCs were located using the autocorrelation algorithm and mapped onto the anatomical US image (Fig. 5.6b). Here the BLInCs can be seen throughout the volume of the lymph node, indicating rapid drainage via the lymphatic system, behavior that has been previously observed and reported for similarly sized particles[14]. Sixty minutes after the injection, B-mode imaging shows the location of a major blood vessel adjacent to the lymph node (Fig. 5.6c, arrow). Imaging of the BLInCs indicates that while they have largely drained from the lymph node, a substantial portion of them are in the vasculature (Fig. 5.6d). The stability of perfluorohexane droplets *in vitro*[15] and perfluoropentane droplets *in vivo*[16] suggest that BLInCs can circulate through the bloodstream for several hours. Prolonged imaging may be conducted due to the sensitivity of the imaging procedure and the ability of the BLInCs to undergo repeatable activation, which would allow sufficient time for their accumulation into extravascular tissues and/or attachment to molecular targets.

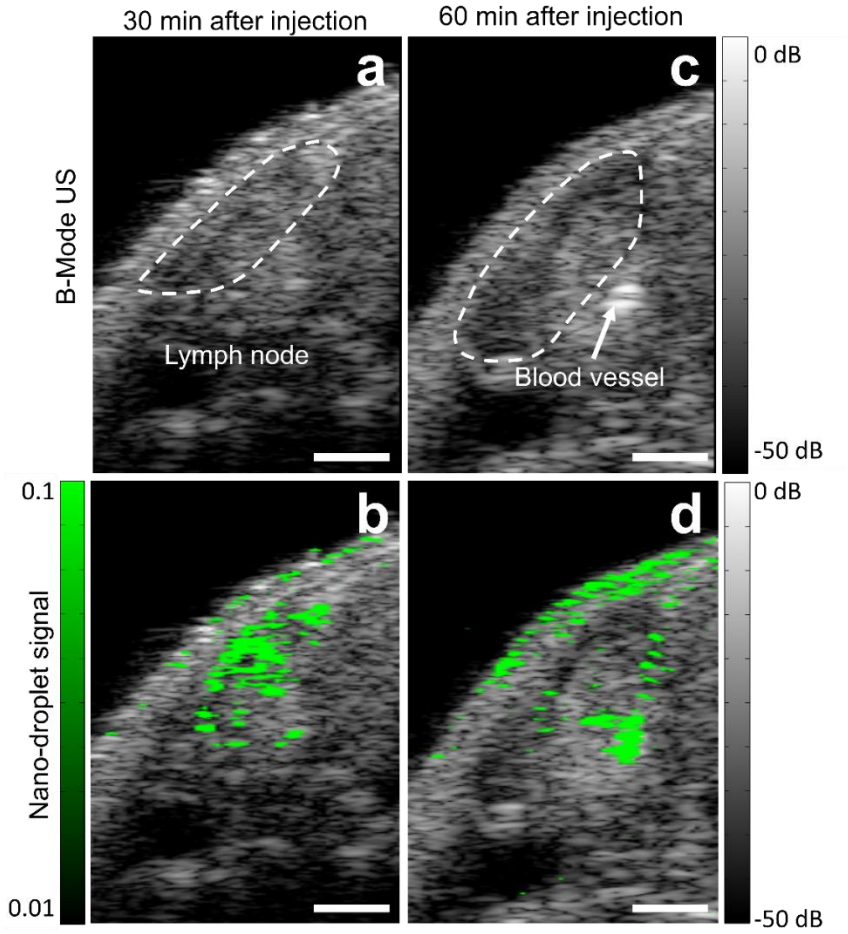

Figure 5.6: (a) Pulse-echo B-mode US image of a mouse lymph node 30 minutes after injection of BLInCs. (b) Image of BLInC location in the region at 30 minutes. (c) B-mode image of the lymph node 60 minutes after BLInCs injection. (d) Image of BLInCs location at 60 minutes. Scale bars = 1 mm.

5.6 Imaging of BLInCs in the Brain

Imaging of brain vasculature may answer important questions about neurophysiology, and US imaging may play a role, given the proper contrast agents and imaging techniques. Here BLInCs were injected into a mouse brain to visualize microvessels with high contrast. Images of the BLInCs using the autocorrelation-based algorithm were compared to B-mode and color Doppler US images of a mouse brain after

a retro-orbital injection of the BLInCs. Conventional B-mode US provides only a gross anatomical image of the brain (Fig. 5.7a). Color Doppler imaging (Fig. 5.7b) is capable of measuring the velocity of blood in large vessels. However, this technique is limited to flow velocities in the direction of sound propagation, and it is not sensitive to slow-moving blood in the smaller vessels of the brain[17]. By identifying the BLInCs, the dense, slow-moving network of microvasculature in the brain can be detected (Fig. 5.7c).

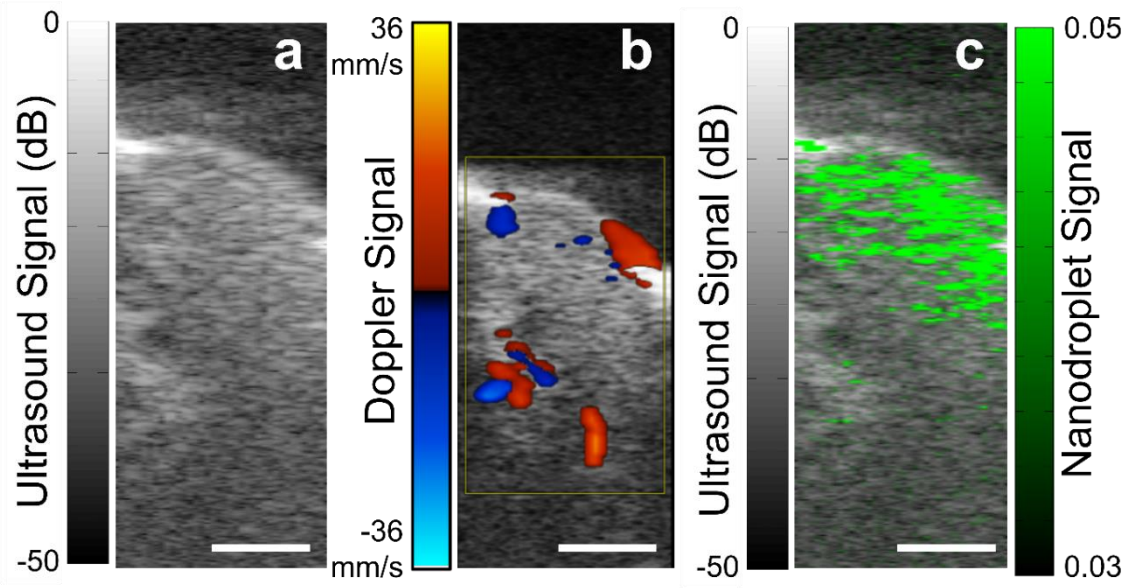

Figure 5.7: (a) B-mode US image of a mouse brain with injected BLInCs. (b) Color Doppler image of the brain, indicating flow of large vessels. (c) B-mode image of brain with overlay of BLInCs location. Scale bar = 1 mm.

5.7 Photoacoustic Imaging of BLINCs

To demonstrate the multimodal imaging capabilities of BLInCs, PA imaging was conducted in the mouse lymph node *in vivo*. Imaging using PA techniques provides a map of the optical absorption, which is greater for BLInCs than for the background tissue (Fig. 5.8a). Previous reports of optically-triggered PFC nanodroplets demonstrate a

stronger signal from vaporization of the droplet than from subsequent thermal expansion of the photoabsorber[8–10]. The BLInCs have the unique property of recondensing, allowing for repeatable vaporization, and thus a sustained PA signal (Fig. 5.8b).

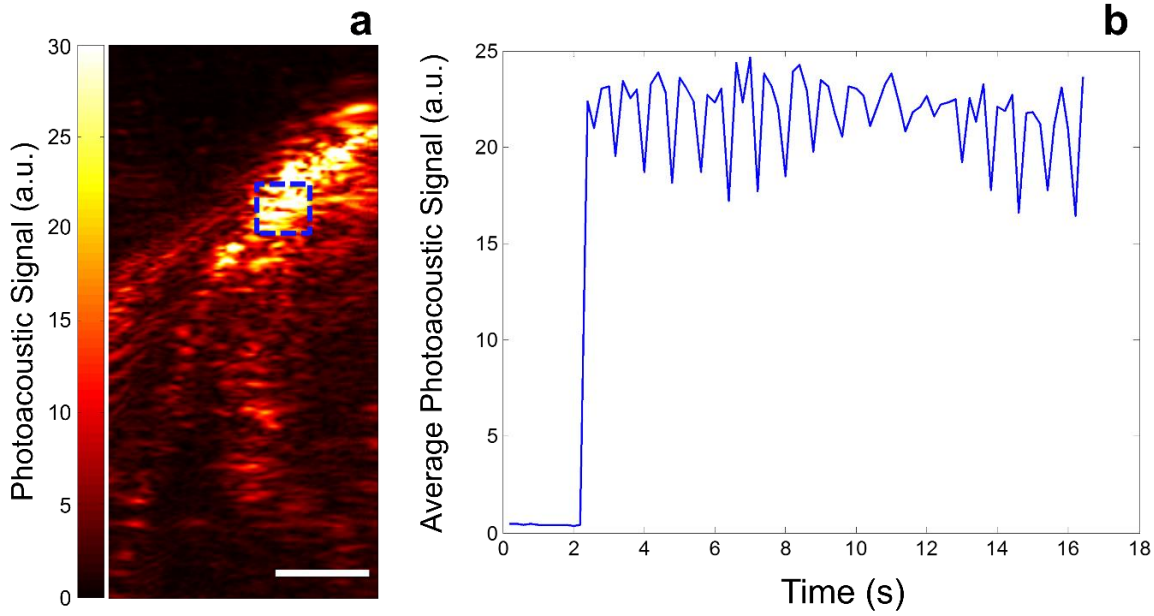

Figure 5.8: (a) Photoacoustic image of BLInCs in a mouse lymph node. Scale bar = 1 mm. (b) Average PA signal in the ROI as a function of time.

5.8 Varying Laser Power for BLInCs

To demonstrate the importance of proper laser fluence used to irradiate the BLInCs, a phantom was made which included BLInCs and imaged using the same techniques described previously. Three different laser fluences were used to irradiate the samples during imaging: 5, 8, and 20 mJ cm^{-2}. The linear US intensity of an individual pixel from each sample was measured (Fig. 5.9a). The BLInCs did not undergo a phase change when irradiated below their vaporization threshold. This makes them difficult to differentiate from the surrounding tissue, and no BLInCs signal can be calculated (Fig. 5.9b). When the phantom is irradiated with laser fluence within a certain range, the BLInCs undergo the

liquid-gas-liquid repeatable phase change (Fig. 5.9c). The images can be processed to identify the particles and they can be irradiated multiple times. At higher laser fluences, in this case 20 mJ cm^{-2}, the BLInCs are prone to undergoing an irreversible phase change (Fig. 5.9d), which results in a stable microbubble and cannot be induced repeatedly. While some particles may still blink, the drastic increase in echogenicity throughout the phantom disguises the smaller changes, and it is more difficult to obtain a map of the BLInCs.

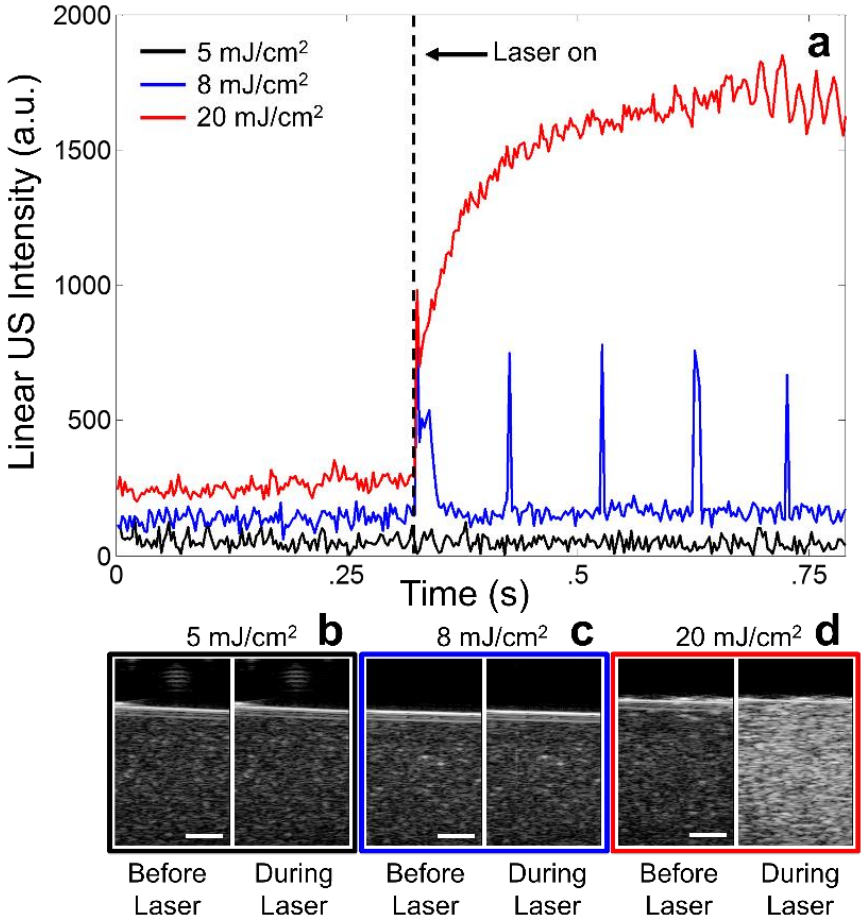

Figure 5.9: (a) Linear US echogenicity of an individual pixel from phantom containing BLInCs irradiated with 5 mJ cm^{-2} (black), 8 mJ cm^{-2} (blue), and 20 mJ cm^{-2} (red) . (b) Ultrasound image of a phantom before and during irradiation at 5 mJ cm^{-2}, (c) 8 mJ cm^{-2}, and (d) 20 mJ cm^{-2}. Scale bars = 1 mm.

5.9 Blinking Artifact

There is considerable concern regarding the signal obtained on the surface of the skin of the mouse (Fig. 5.5c). To determine if the signal was coming from the BLInCs, three additional mice were imaged using identical methods, except that no BLInCs were injected. Two were imaged around the lymph node, and a third was imaged in the abdomen.

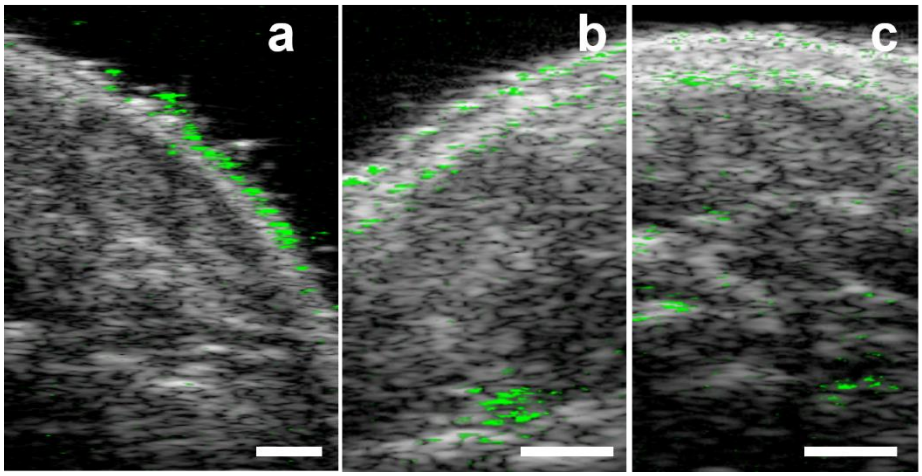

Figure 5.10: (a) Mouse lymph node imaged with US without injection, showing signal at the gel-skin interface. (b) Mouse lymph node imaged with US with no injection and using degassed coupling gel. (c) Mouse abdomen imaged with US without injection and using degassed US gel. Scale bars = 1 mm.

Because these three mice were imaged without the injection of BLInCs, the signal, which is obtained by the method described in Section 5.4, cannot originate from the vaporization and recondensation of BLInCs. However, there are changes in US signal at the gel-skin interface which correspond in time exactly to the laser pulses, and thus appears as BLInC signal (Fig. 5.10a). It is hypothesized that small bubbles at the interface between the US gel and the skin are present. In response to laser pulses, PA waves are emitted from endogenous chromophores. These acoustic emissions may interact with the surface bubbles, causing small but noticeable oscillations, resulting in regular spaced changes in US contrast. Next, another mouse was imaged, and the US gel was centrifuged before

imaging to remove any air bubbles and decrease the likelihood of interfacial bubbles. In this experiment, a decrease in signal is observed at the skin-gel interface (Fig. 5.10b). However, there is still some underlying signal present in the mouse. Lastly, a mouse was imaged with degassed gel, but imaged it over the abdomen instead of the lymph node. The signal at the skin-gel interface was decreased as well, though some signal in the skin is detected (Fig. 5.10c). It is possible that sub-surface bubbles, particularly in regions of high blood flow, may be interacting with the PA waves and causing cyclical changes in US signal that appears as signal from blinking nanodroplets. Overall, however, the signal that appears in mice that were not injected with BLInCs is significantly smaller than the signal in the lymph node after BLInCs injection (Fig. 5.5c).

5.10 Conclusions

The blinking behavior of BLInCs make them a valuable tool for high contrast biomedical imaging. However, for the BLInCs to undergo repeatable vaporization effectively, several parameters which dictate droplet vaporization must be optimized[6,7,10]. For instance, if the laser fluence is too low, then the droplets will not vaporize. If the fluence is too high, or the particles are too large, then they will not recondense after vaporization, and they cannot be triggered multiple times (Fig. 5.9d). In addition, the injectable nanoconstructs must be made of materials approved for human use before clinical translation. While the BLInCs reported here encapsulate an NIR-absorbing dye for improved optical penetration in tissue at 1064 nm, similar particles have been made using clinically approved indocyanine green dye[10]. Thus it is feasible to synthesize BLInCs out of entirely approved materials to be used in a clinical setting.

Many particle formulations have been applied for triggered contrast using HIFU as a vaporization trigger[18,19], and HIFU could potentially be used to induce repeated

vaporization and recondensation of perfluorocarbon nanodroplets without a laser or optical absorber. However, due to the high boiling point of perfluorohexane, vaporization with HIFU would potentially require intensity levels of up to 980 W cm^{-2} [5], which is at least 500 times the safe recognized level for peripheral tissue[20], and may compromise the safety of the vaporization technique. The optical trigger provides a safer mechanism for vaporization of the particles.

The BLInCs introduced here facilitate a new technique for detecting nanoparticles with a conventional US imaging system. Due to their stability and small size, the droplets are capable of extended circulation time and extravasation, a key component of imaging on the molecular scale. The BLInCs are made to activate through a unique, laser-induced rapid sequence of two phase changes—vaporization and recondensation—which can be processed into an extremely high contrast map of the particles. This imaging technique is highly sensitive to diluted particles. Due to their blinking behavior, individual BLInCs can be located among the vast acoustic scatterers present in tissue. In addition to the background-free image, the BLInCs provide photoacoustic signal from the vaporization event, a property that has been previously reported from similar particles[8–10,21]. These experiments demonstrate the ability to locate BLInCs with high specificity and sensitivity in the optically absorbing and acoustically scattering background of a living mouse. Furthermore, cell-specific targeting has been achieved with similar perfluorocarbon microbubbles by conjugating various molecules to the particle shell[22–25]. The smaller size and enhanced circulation time of nanodroplets would make them a feasible candidate for molecular imaging as well, expanding the performance of this nanoparticle-based US imaging platform.

5.11 References

1. Simpson, D. H., Chin, C. T. & Burns, P. N. Pulse inversion Doppler: a new method for detecting nonlinear echoes from microbubble contrast agents. *IEEE Trans. Ultrason. Ferroelectr. Freq. Control* **46,** 372–382 (1999).
2. Miller, D. L. Ultrasonic detection of resonant cavitation bubbles in a flow tube by their second-harmonic emissions. *Ultrasonics* **19,** 217–224 (1981).
3. Needles, A. *et al.* Nonlinear contrast imaging with an array-based micro-ultrasound system. *Ultrasound Med. Biol.* **36,** 2097–2106 (2010).
4. Bauer, A. *et al.* Wideband harmonic imaging: a novel contrast ultrasound imaging technique. *Eur. Radiol.* **9,** S364–S367 (1999).
5. Asami, R., Azuma, T. & Kawabata, K. Fluorocarbon droplets as next generation contrast agents - their behavior under 1 #x2013;3 MHz ultrasound. *Ultrasonics Symposium (IUS), 2009 IEEE International* 1294–1297 (2009).
6. Reznik, N., Williams, R. & Burns, P. N. Investigation of vaporized submicron perfluorocarbon droplets as an ultrasound contrast agent. *Ultrasound Med. Biol.* **37,** 1271–1279 (2011).
7. Reznik, N. *et al.* The efficiency and stability of bubble formation by acoustic vaporization of submicron perfluorocarbon droplets. *Ultrasonics* **53,** 1368–1376 (2013).
8. Wilson, K., Homan, K. & Emelianov, S. Biomedical photoacoustics beyond thermal expansion using triggered nanodroplet vaporization for contrast-enhanced imaging. *Nat. Commun.* **3,** 618 (2012).

9. Strohm, E. M., Rui, M., Kolios, M. C., Gorelikov, I. & Matsuura, N. Optical droplet vaporization (ODV): photoacoustic characterization of perfluorocarbon droplets. *2010 IEEE Ultrasonics Symposium (IUS)* 495–498 (2010).

10. Hannah, A., Luke, G., Wilson, K., Homan, K. & Emelianov, S. Indocyanine green-loaded photoacoustic nanodroplets: dual contrast nanoconstructs for enhanced photoacoustic and ultrasound imaging. *ACS Nano* **8,** 250–259 (2014).

11. Cook, J. R., Bouchard, R. R. & Emelianov, S. Y. Tissue-mimicking phantoms for photoacoustic and ultrasonic imaging. *Biomed. Opt. Express* **2,** 3193 (2011).

12. Myers, J. N., Holsinger, F. C., Jasser, S. A., Bekele, B. N. & Fidler, I. J. An orthotopic nude mouse model of oral tongue squamous cell carcinoma. *Clin. Cancer Res.* **8,** 293–298 (2002).

13. Luke, G. P., Myers, J. N., Emelianov, S. Y. & Sokolov, K. V. Sentinel lymph node biopsy revisited: ultrasound-guided photoacoustic detection of micrometastases using molecularly targeted plasmonic nanosensors. *Cancer Res.* **74**, 19 (2014).

14. Luke, G. P. *et al.* Silica-coated gold nanoplates as stable photoacoustic contrast agents for sentinel lymph node imaging. *Nanotechnology* **24,** 455101 (2013).

15. Simons, J. M. M. *et al.* Monodisperse perfluorohexane emulsions for targeted ultrasound contrast imaging. *J. Mater. Chem.* **20,** 3918 (2010).

16. Rapoport, N. *et al.* Ultrasound-mediated tumor imaging and nanotherapy using drug loaded, block copolymer stabilized perfluorocarbon nanoemulsions. *J. Controlled Release* **153,** 4–15 (2011).

17. Heimdal, A. & Torp, H. Ultrasound Doppler measurements of low velocity blood flow: limitations due to clutter signals from vibrating muscles. *IEEE Trans. Ultrason. Ferroelectr. Freq. Control* **44,** 873–881 (1997).

18. Miller, D. L., Kripfgans, O. D., Fowlkes, J. B. & Carson, P. L. Cavitation nucleation agents for nonthermal ultrasound therapy. *J. Acoust. Soc. Am.* **107,** 3480–3486 (2000).

19. Rapoport, N., Gao, Z. & Kennedy, A. Multifunctional nanoparticles for combining ultrasonic tumor imaging and targeted chemotherapy. *J. Natl. Cancer Inst.* **99,** 1095–1106 (2007).

20. Singh, V. R. Safety standards for medical ultrasound systems." *World Congress on Medical Physics and Biomedical Engineering 2006*. Springer Berlin Heidelberg (2007).

21. Hannah, A. S., VanderLaan, D., Chen, Y.-S. & Emelianov, S. Y. Photoacoustic and ultrasound imaging using dual contrast perfluorocarbon nanodroplets triggered by laser pulses at 1064 nm. *Biomed. Opt. Express* **5,** 3042 (2014).

22. Willmann, J. K. *et al.* US imaging of tumor angiogenesis with microbubbles targeted to vascular endothelial growth factor receptor type 2 in mice. *Radiology* **246,** 508–518 (2008).

23. Villanueva, F. S. *et al.* Microbubbles targeted to intercellular adhesion molecule-1 bind to activated coronary artery endothelial cells. *Circulation* **98,** 1–5 (1998).

24. Lindner, J. R. *et al.* Ultrasound assessment of inflammation and renal tissue injury with microbubbles targeted to p-selectin. *Circulation* **104,** 2107–2112 (2001).

25. Ellegala, D. B. *et al.* Imaging tumor angiogenesis with contrast ultrasound and microbubbles targeted to αvβ3. *Circulation* **108,** 336–341 (2003).

Chapter 6: Conclusions and Future Work

6.1 Motivation

There were several motivating factors behind the efforts of this research, reasons to pursue answers to fundamental questions or to develop materials and imaging techniques. First and principally, this research aimed to improve the ability of US and PA imaging techniques to identify tumors and other targeted diseases at an early stage. Although ultrasound is a clinically ubiquitous modality, it still has shortcomings that prevent its use in many applications. If solutions to these issues can be engineered, US imaging can prevail as an inexpensive, easy, safe imaging technique that becomes the gold standard for diagnosing many diseases.

Since the advent of photoacoustics and PA imaging, scientists have discovered numerous ways that light and sound interact, yielding high contrast images and wavelength-based specificity for specific biological chromophores. Additionally, the introduction of injectable agents opened the door to many technologies that use chemistry, mechanics, and electromagnetism to achieve theranostic purposes. By developing these agents in a laboratory setting and implementing them in biomedical imaging research, we gain further knowledge of the underlying physics of their operation and how we can exploit their behavior to bring about impactful clinical results.

As with any research, experiments lead to more questions than answers, and sometimes these questions lead to discovery outside the scope of the original inquiry. In addition to the direct study of perfluorocarbon nanodroplets for ultrasound and photoacoustic imaging, this research contributes to other related scientific endeavors which may use the technology. Some of these include the development of super resolution

ultrasound imaging, drug delivery, therapeutic acoustics, image processing techniques, and bubble physics.

6.2 Scientific Innovation, Contribution, Significance

With the help of past researchers and collaborative work, we made several contributions to the field of biomedical imaging. To summarize the scientific significance of this work, we first designed an injectable contrast agent based on properties that are important to biomedical imaging, including safety, high contrast, sensitivity for imaging depth, facile synthesis, and cost. We designed and developed the first dual US and PA contrast agent made entirely of materials approved for clinical use, and demonstrated strong improvements in image contrast. Next, we furthered the functionality of currently synthesized US/PA contrast agents by synthesizing a perfluorocarbon particle encapsulating high aspect ratio gold nanorods, using a specific wavelength selection (based on others' previous findings[1]) to optimize the particle's sensitivity and contrast. We also created a new blinking nanodroplet, capable of undergoing repeated activation, and we developed an image processing algorithm for extremely high contrast imaging of the particles, which other activatable nanodroplets cannot achieve. Lastly, we demonstrated the ability of these particles to identify key diagnostic features *in vivo*, including the sentinel lymph node and brain vasculature in mice.

6.3 Clinical Relevance

As a biomedical engineering laboratory, it is our mission to conduct research that is relevant for human problems, and it is my hope that this research has clinical applicability outside of the lab. The ICG-loaded nanodroplets could potentially be translated to the clinic quickly upon the approval of photoacoustic imaging techniques. Additionally, although gold nanoparticles face difficulty in clinical approval, the gold nanorod-loaded PFC

droplets have shown great promise in PA imaging. Gold nanorod-loaded PFC droplets, when combined with an Nd:YAG laser, would decrease the operational cost and increase sensitivity and contrast in medical imaging. Lastly, the introduction of BLINCs into a clinical setting would vastly improve the contrast and specificity of US imaging, which is arguably the greatest drawback of this imaging modality. By improving US image contrast and thus making it easy and for ancillary technologies to be used, the clinical impact of US imaging could extend beyond obstetric sonography and into early detection of a wider array of diseases.

6.4 Future Directions

Through developing nanoparticles and imaging them with US techniques, several unexplored directions and specific questions were unearthed. It is hoped that through the continuation of this work, some of the more relevant pursuits will be investigated by future researchers in the laboratory.

6.4.1 Mechanism of Optical Droplet Vaporization

The exact mechanism of optically triggered perfluorocarbon droplet vaporization has yet to be clearly elucidated. Some experiments hinted that the photoabsorber heats the perfluorocarbon beyond its boiling point[2,3], resulting in boiling of the PFC or of the surrounding water. Experiments in Section 4.2.7, however, hint that heating of the PFC by a continuous wave laser does not suffice for droplet vaporization, and instead the production of a photoacoustic pressure wave by a pulsed laser may be necessary to vaporize them. Unfortunately, due to lack of control over laser power (energy per unit time), these experiments did not definitively answer the question. Either through high speed optical microscopy, or by clever experimental design, the behavior of the nanodroplets in response to optical irradiation could be determined and is of interest for designing contrast agents

and an imaging system. Current collaborative work with the Multi-modality Biomedical Ultrasound Imaging Lab at the University of Pittsburgh is hoping to answer this question by observing with high speed microscopy and changing the length of the laser pulse. At the time of this writing, however, it is still uncertain.

6.4.2 Mapping Elasticity and Pressure

Initial experiments have been conducted which show that the behavior of vaporized droplets depends largely on the elasticity and the local pressure of the environment in which they are activated, which varies between healthy and diseased tissues (Sections 4.2.2 and 4.2.3). The goal of this project was to devise a system of measuring the elasticity and pressure of tissue with high resolution to map the confines of tumor growth. However, practical limitations made this difficult. Namely, while pressure certainly the affected the vaporization and recondensation kinetics of nanodroplets, the differences in interstitial pressure between tumor tissue and healthy tissue are small compared to the ranges measured in this study. Thus detecting these differences may be difficult *in vivo*, where blood flow optical attenuation may confound droplet behavior.

Differences in elasticity between healthy and cancerous tissue are large enough to impact vaporization and recondensation of the droplets. However, in our experiment, the particles were embedded within the matrix of a polyacrylamide phantom, whereas *in vivo* they are circulating through the bloodstream and possibly perfusing through tumor tissue. Their behavior in a phantom thus might not accurately mimic their behavior *in vivo*, so further modifications to the particles and/or experimental design must be made to improve the tool enough to bring about its intended purpose. Specifically, the behavior of droplets varies more due to the range of sizes within a sample than it does on the external

environment. Controlling the droplet size is thus necessary to extract accurate data regarding elasticity and pressure.

6.4.3 Molecular Targeting

The focus of all biomedical imaging techniques is shifting toward the detection of processes at a molecular level, because many diseases exhibit this subcellular information before they emerge on the level of gross anatomy or physiology. Injectable contrast agents, especially on the nano scale, are a primary candidate for detection of molecular processes. These agents can be manipulated to bind to specific biomarkers and exhibit high contrast, thus providing this molecular information. The molecular targeting capabilities of perfluorocarbon particles were only minimally explored in this work (Section 2.6). However, based on the size, components, and high contrast capabilities of BLInCs, for example, a safe, inexpensive, highly specific imaging strategy could be developed with potential for locating early disease markers far before anatomical indicators emerge.

6.4.4 Repeated Vaporization as a Therapeutic Tool

The BLInCs are an advancement from traditional nanodroplets, largely due to their ability to activate repeatedly[4]. Other perfluorocarbon droplets undergo vaporization only one time. The repeatable vaporization has potential as a therapeutic tool. Traditionally microbubbles have been combined with focused ultrasound to induce cavitation and micro streaming, inducing clot lysis[5], ablation[6], sonoporation[7], and lithotripsy[8]. However, using repeated optical triggering of vaporization, the mechanical and thermal effects of HIFU could be avoided, and localize the therapeutic effects of the agent. This could have applications in the above mentioned therapies, as well as drug delivery.

6.4.5 Drug Delivery Using Nanodroplets

The use of PFC nanodroplets in drug delivery are currently being explored by encapsulating drugs in the core or shell and inducing their release through triggered vaporization[9–11]. Additionally, enhanced uptake can be achieved by using microbubbles in the presence of HIFU[12]. Perfluorohexane droplets, which vaporize repeatedly in response to many laser pulses, may be used to achieve the same effect without the potentially harmful bioeffects of HIFU.

6.4.6 Oxygen Delivery Using Nanodroplets

Another therapeutic capability of perfluorocarbon is oxygen delivery[13,14], which can improve the survival of stem cells[15], or render PFC nanoparticles oxygen-carrying blood substitutes[16]. The high solubility of oxygen in perfluorocarbon, as well as their prolonged circulation time, make PFC nanodroplets a candidate for these therapeutic tools. It is also possible that the delivery of oxygen from a stored state in PFC particles to cellular recipients may be induced through triggered vaporization at strategic time points[17]. The imaging capabilities of these particles may allow for visualization of the oxygen delivery to regions of interest.

6.4.7 Magneto-Motive Droplet Vaporization

A new area of research with perfluorocarbon droplets involves yet another mechanism of vaporization separate from HIFU and optical based vaporization. Previously, “magneto-motive” ultrasound imaging has been conducted, where an external high-strength pulsed magnetic field is applied to induce motion within magnetically-labeled tissue, and ultrasound is used to detect the induced internal tissue motion[18]. It is possible that by encapsulating these magnetic particles inside perfluorocarbon droplets,

magneto-motive droplet vaporization could be achieved. The benefit is that magnetic activation could be achieved at greater depths than from optical activation, which limited by optical attenuation from tissue. Also, due to the absence of photothermal heating using this technique, it is possible to demonstrate vaporization without boiling the perfluorocarbon.

6.4.8 Optimizing Encapsulation of Gold Nanoparticles

In addition to these new paths of experimental work, the nanodroplets themselves may still be improved in several ways. First, the encapsulation of ICG or gold nanoparticles into the droplets is a chemically inefficient process, resulting in loss of ICG or gold particles and aggregation of gold particles due to the addition of chemicals mentioned in Sections 2.3.1 and 2.3.2. By exploring additional solvents and adjusting the chemical reactions of this process, the synthesis of PAnDs could be a lossless process and potentially result in a very narrow absorption band, making them very sensitive to light at a specific wavelength, and insensitive to other wavelengths. By doing this, one could construct a cocktail of nanodroplets with several activation wavelengths. Following a single injection, one can activate a subset of the particles using one wavelength (to identify their location, for instance) and activate another subset some time later (for oxygen or drug delivery).

6.4.9 New Optically Absorbing Dyes for Nanodroplets

At the time of this work, only three dyes have been reported to be incorporated into PFC nanodroplets. Indocyanine green requires a chemical modification, Epolight™ 3072 contains nickel, and Acridine Orange, used by the Multi-modality Biomedical Ultrasound Imaging Lab at the University of Pittsburgh, absorbs light at the same wavelength as blood. The chemical engineering of new dyes that could easily be incorporated into

perfluorocarbon is highly desired. These new dyes could be designed to absorb at specific wavelengths, have high optical absorption, and be soluble in perfluorocarbon.

6.4.10 Mixing Perfluorocarbons

Nanodroplets can be synthesized from several different perfluorocarbons, and this project focuses on just three. However, several more exist with higher and lower boiling points that could be used to make extremely sensitive particles for deep activation or highly stable particles for long-term circulation, or passive or active targeting. Additionally and interestingly, perfluorocarbons can be mixed before synthesizing droplets. This has been done previously for acoustic droplet vaporization[19], and it could be applied to optical vaporization as well. Incipient work on this topic is being explored currently but is not included in this report.

6.4.11 Narrowing the Size Distribution of Nanodroplets

Lastly, the size distribution of the particles is currently wide, from 100 nm to over 2 μm. This wide range of sizes results in different behavior of the droplets within a sample, most notably their stability and vaporization threshold. This is not optimal as an engineering design or for obtaining accurate experimental results. If a uniform droplet size can be achieved within a sample, then an exact vaporization threshold could be measured, and the droplet behavior in response to other factors (environmental stiffness, photoabsorber loading, imaging depth, etc.) could be measured more accurately. Additionally, biodistribution could be determined more easily from a monodisperse sample. Current research using microfluidics and condensation techniques hope to narrow the size range within a sample of droplets.

6.5 References

1. Homan, K. *et al.* Prospects of molecular photoacoustic imaging at 1064 nm wavelength. *Opt. Lett.* **35,** 2663–2665 (2010).
2. Sukhorukov, G. B. *et al.* Nanoengineered polymer capsules: tools for detection, controlled delivery, and site-specific manipulation. *Small* **1,** 194–200 (2005).
3. Lajoinie, G. *et al.* Ultrafast vapourization dynamics of laser-activated polymeric microcapsules. *Nat. Commun.* **5,** (2014).
4. Asami, R. & Kawabata, K. Repeatable vaporization of optically vaporizable perfluorocarbon droplets for photoacoustic contrast enhanced imaging. *Ultrasonics Symposium (IUS), 2012 IEEE International* 1200–1203 (2012).
5. Brown, A. T. *et al.* Microbubbles improve sonothrombolysis in vitro and decrease hemorrhage in vivo in a rabbit stroke model. *Invest. Radiol.* **46,** (2011).
6. Zhang, P. & Porter, T. An in vitro study of a phase-shift nanoemulsion: a potential nucleation agent for bubble-enhanced HIFU tumor ablation. *Ultrasound Med. Biol.* **36,** 1856–1866 (2010).
7. Liang, H.-D., Tang, J. & Halliwell, M. Sonoporation, drug delivery, and gene therapy. *Proc. Inst. Mech. Eng. [H]* **224,** 343–361 (2010).
8. Yoshizawa, S. *et al.* High intensity focused ultrasound lithotripsy with cavitating microbubbles. *Med. Biol. Eng. Comput.* **47,** 851–860 (2009).
9. Lattin, J. R., Belnap, D. M. & Pitt, W. G. Formation of eLiposomes as a drug delivery vehicle. *Colloids Surf. B Biointerfaces* **89,** 93–100 (2012).

10. Kang, S.-T. & Yeh, C.-K. Intracellular acoustic droplet vaporization in a single peritoneal macrophage for drug delivery applications. *Langmuir* **27,** 13183–13188 (2011).

11. Fabiilli, M. L. *et al.* Delivery of chlorambucil using an acoustically-triggered perfluoropentane emulsion. *Ultrasound Med. Biol.* **36,** 1364–1375 (2010).

12. Ferrara, K., Pollard, R. & Borden, M. Ultrasound microbubble contrast agents: fundamentals and application to gene and drug delivery. *Annu. Rev. Biomed. Eng.* **9,** 415–447 (2007).

13. Riess, J. G. The design and development of improved fluorocarbon-based products for use in medicine and biology. *Artif. Cells Blood Substit. Biotechnol.* **22,** 215–234 (1994).

14. Riess, J. G. Perfluorocarbon-based oxygen delivery. *Artif. Cells Blood Substit. Biotechnol.* **34,** 567–580 (2006).

15. Cavalli, R. *et al.* Preparation and characterization of dextran nanobubbles for oxygen delivery. *Int. J. Pharm.* **381,** 160–165 (2009).

16. Biro, G. P., Blais, P. & Rosen, A. L. Perfluorocarbon blood substitutes. *Crit. Rev. Oncol. Hematol.* **6,** 311–374 (1987).

17. Magnetto, C. *et al.* Ultrasound-activated decafluoropentane-cored and chitosan-shelled nanodroplets for oxygen delivery to hypoxic cutaneous tissues. *RSC Adv.* **4,** 38433–38441 (2014).

18. Mehrmohammadi, M., Oh, J., Mallidi, S. & Emelianov, S. Y. Pulsed magneto-motive ultrasound imaging using ultrasmall magnetic nanoprobes. *Mol. Imaging* **10,** 102–110 (2011).

19. Sheeran, P. S., Luois, S. H., Mullin, L. B., Matsunaga, T. O. & Dayton, P. A. Design of ultrasonically-activatable nanoparticles using low boiling point perfluorocarbons. *Biomaterials* **33,** 3262–3269 (2012).

References

Aaslid, R., Markwalder, T.-M. & Nornes, H. Noninvasive transcranial Doppler ultrasound recording of flow velocity in basal cerebral arteries. *Spec. Suppl*. **112**, 769–774 (2009).

Albanese, A., Tang, P. S. & Chan, W. C. W. The effect of nanoparticle size, shape, and surface chemistry on biological systems. *Annu. Rev. Biomed. Eng*. **14**, 1–16 (2012).

Apfel, R. E. Activatable infusable dispersions containing drops of a superheated liquid for methods of therapy and diagnosis. U.S. Patent No. 5,840,276 filed 8 Jan. 1997, and issued 24 Nov. 1998.

Asami, R. & Kawabata, K. Repeatable vaporization of optically vaporizable perfluorocarbon droplets for photoacoustic contrast enhanced imaging. *Ultrasonics Symposium (IUS), 2012 IEEE International* 1200–1203 (2012).

Barnett, S. B. *et al*. International recommendations and guidelines for the safe use of diagnostic ultrasound in medicine. *Ultrasound Med. Biol*. **26**, 355–366 (2000).

Bashkatov, A. N., Genina, E. A., Kochubey, V. I. & Tuchin, V. V. Optical properties of human skin, subcutaneous and mucous tissues in the wavelength range from 400 to 2000 nm. *J. Phys. Appl. Phys*. **38**, 2543 (2005).

Bauer, A. *et al*. Wideband harmonic imaging: a novel contrast ultrasound imaging technique. *Eur. Radiol*. **9**, S364–S367 (1999).

Bell, A. G. *Upon the Production of Sound by Radiant Energy*. Gibson Brothers, printers (1881).

Biro, G. P., Blais, P. & Rosen, A. L. Perfluorocarbon blood substitutes. *Crit. Rev. Oncol. Hematol*. **6**, 311–374 (1987).

Bloch, F. Nuclear induction. *Phys. Rev*. **70**, 460–474 (1946).

Borden, M. A. & Longo, M. L. Dissolution behavior of lipid monolayer-coated, air-filled microbubbles: effect of lipid hydrophobic chain length. *Langmuir* **18**, 9225–9233 (2002).

Brown, A. T. *et al*. Microbubbles improve sonothrombolysis in vitro and decrease hemorrhage in vivo in a rabbit stroke model. *Invest. Radiol*. **46**, (2011).

Brownell, G. L. & Sweet, W. H. Localization of brain tumors with positron emitters. *Nucleonics* **11**, 40–45 (1953).

Burckhardt, C. B. Speckle in ultrasound B-mode scans. *IEEE Trans. Sonics Ultrason*. **25**, 1–6 (1978).

Butt, H.-J., Graf, K. & Kappl, M. *Physics and Chemistry of Interfaces*. John Wiley & Sons (2006).

Carr, H. Y. & Purcell, E. M. Effects of diffusion on free precession in nuclear magnetic resonance experiments. *Phys. Rev*. **94**, 630–638 (1954).

Cavalli, R. *et al*. Preparation and characterization of dextran nanobubbles for oxygen delivery. *Int. J. Pharm*. **381**, 160–165 (2009).

Charafe-Jauffret, E. *et al*. Breast cancer cell lines contain functional cancer stem cells with metastatic capacity and a distinct molecular signature. *Cancer Res*. **69**, 1302–1313 (2009).

Chen, H. & Diebold, G. Chemical generation of acoustic waves: a giant photoacoustic effect. *Science* **270**, 963–966 (1995).

Chivers, R. C. The scattering of ultrasound by human tissues—some theoretical models. *Ultrasound Med. Biol*. **3**, 1–13 (1977).

Church, C. C. Spontaneous homogeneous nucleation, inertial cavitation and the safety of diagnostic ultrasound. *Ultrasound Med. Biol*. **28**, 1349–1364 (2002).

Cook, J. R., Bouchard, R. R. & Emelianov, S. Y. Tissue-mimicking phantoms for photoacoustic and ultrasonic imaging. *Biomed. Opt. Express* **2**, 3193 (2011).

Correas, J. M. *et al*. The first phase shift ultrasound contrast agent: EchoGen. *Ultrasound Contrast Agents*. 101–120 (1997).

Cuezva, J. M. *et al*. The bioenergetic signature of lung adenocarcinomas is a molecular marker of cancer diagnosis and prognosis. *Carcinogenesis* **25**, 1157–1163 (2004).

Curti, B. D. Physical barriers to drug delivery in tumors. *Crit. Rev. Oncol. Hematol*. **14**, 29–39 (1993).

Dayton, P. A. & Ferrara, K. W. Targeted imaging using ultrasound. *J. Magn. Reson. Imaging* **16**, 362–377 (2002).

Dayton, P. A. *et al*. Application of ultrasound to selectively localize nanodroplets for targeted imaging and therapy. *Mol. Imaging* **5**, 160–174 (2006).

De Gennes, P. G., Brochard-Wyart, F. & Quéré, D. *Capillarity and Wetting Phenomena - Drops, Bubbles, Pearls, Waves.* Springer (2004).

De Jong, N., Emmer, M., van Wamel, A. & Versluis, M. Ultrasonic characterization of ultrasound contrast agents. *Med. Biol. Eng. Comput*. **47**, 861–873 (2009).

De Jong, N., Hoff, L., Skotland, T. & Bom, N. Absorption and scatter of encapsulated gas filled microspheres: Theoretical considerations and some measurements. *Ultrasonics* **30**, 95–103 (1992).

De La Zerda, A. *et al*. Carbon nanotubes as photoacoustic molecular imaging agents in living mice. Nat. *Nanotechnol*. **3**, 557–562 (2008).

Deans, S. R. *The Radon Transform and Some Of Its Applications*. Courier Dover Publications (2007).

Diebold, G. J. & Sun, T. properties of photoacoustic waves in one, two, and three dimensions. *Acta Acust. United Acust*. **80**, 339–351 (1994).

Dove, J. D., Mountford, P. A., Murray, T. W. & Borden, M. A. Engineering optically triggered droplets for photoacoustic imaging and therapy. *Biomed. Opt. Express* **5**, 4417 (2014).

Du, Y. *et al*. Optical properties of porcine skin dermis between 900 nm and 1500 nm. *Phys. Med. Biol*. **46**, 167 (2001).

Ellegala, D. B. *et al*. Imaging tumor angiogenesis with contrast ultrasound and microbubbles targeted to αvβ3. *Circulation* **108**, 336–341 (2003).

Epstein, P. S. & Plesset, M. S. On the stability of gas bubbles in liquid-gas solutions. *J. Chem. Phys*. **18**, 1505–1509 (1950).

Fabiilli, M. L. *et al*. Delivery of chlorambucil using an acoustically-triggered perfluoropentane emulsion. *Ultrasound Med. Biol*. **36**, 1364–1375 (2010).

Fabiilli, M. L. *et al*. The role of inertial cavitation in acoustic droplet vaporization. *IEEE Trans. Ultrason. Ferroelectr. Freq. Control* **56**, 1006–1017 (2009).

Fang, C. *et al*. In vivo tumor targeting of tumor necrosis factor-α-loaded stealth nanoparticles: Effect of MePEG molecular weight and particle size. *Eur. J. Pharm. Sci*. **27**, 27–36 (2006).

Ferrara, K., Pollard, R. & Borden, M. Ultrasound microbubble contrast agents: fundamentals and application to gene and drug delivery. *Annu. Rev. Biomed. Eng*. **9**, 415–447 (2007).

Fischer, R. S., Myers, K. A., Gardel, M. L. & Waterman, C. M. Stiffness-controlled three-dimensional extracellular matrices for high-resolution imaging of cell behavior. *Nat. Protoc*. **7**, 2056–2066 (2012).

Forsberg, F. *et al*. Conventional and hypobaric activation of an ultrasound contrast agent. *Ultrasound Med. Biol*. **24**, 1143–1150 (1998).

Giesecke, T. & Hynynen, K. Ultrasound-mediated cavitation thresholds of liquid perfluorocarbon droplets in vitro. *Ultrasound Med. Biol*. **29**, 1359–1365 (2003).

Gorelikov, I., Martin, A. L., Seo, M. & Matsuura, N. Silica-coated quantum dots for optical evaluation of perfluorocarbon droplet interactions with cells. *Langmuir* **27**, 15024–15033 (2011).

Gramiak, R. & Shah, P. M. Echocardiography of the aortic root. *Invest. Radiol*. **3**, 356–366 (1967).

Gusev, V. E. & Karabutov, A. A. Laser optoacoustics. *Am. Inst. Phys*. 63–77 (1993).

Haar, G. ter. Safety and bio-effects of ultrasound contrast agents. *Med. Biol. Eng. Comput*. **47**, 893–900 (2009).

Hahn, E. L. Spin echoes. *Phys. Rev*. **80**, 580–594 (1950).

Hannah, A. S., VanderLaan, D., Chen, Y.-S. & Emelianov, S. Y. Photoacoustic and ultrasound imaging using dual contrast perfluorocarbon nanodroplets triggered by laser pulses at 1064 nm. *Biomed. Opt. Express* **5**, 3042 (2014).

Hannah, A., Luke, G., Wilson, K., Homan, K. & Emelianov, S. Indocyanine green-loaded photoacoustic nanodroplets: dual contrast nanoconstructs for enhanced photoacoustic and ultrasound imaging. *ACS Nano* **8**, 250–259 (2014).

Heimdal, A. & Torp, H. Ultrasound Doppler measurements of low velocity blood flow: limitations due to clutter signals from vibrating muscles. *IEEE Trans. Ultrason. Ferroelectr. Freq. Control* **44**, 873–881 (1997).

Heldin, C.-H., Rubin, K., Pietras, K. & Östman, A. High interstitial fluid pressure — an obstacle in cancer therapy. *Nat. Rev. Cancer* **4**, 806–813 (2004).

Hoe, S., Young, P. M., Rogueda, P. & Traini, D. determination of reference ultrasound parameters for model and hydrofluoroalkane propellants using high-resolution ultrasonic spectroscopy. *AAPS PharmSciTech* **9**, 605–611 (2008).

Hoff, L., Sontum, P. C. & Hovem, J. M. Oscillations of polymeric microbubbles: effect of the encapsulating shell. *J. Acoust. Soc. Am*. **107**, 2272–2280 (2000).

Homan, K. A. *et al*. Silver nanoplate contrast agents for in vivo molecular photoacoustic imaging. *ACS Nano* **6**, 641–650 (2012).

Homan, K. *et al*. Prospects of molecular photoacoustic imaging at 1064 nm wavelength. *Opt. Lett*. **35**, 2663–2665 (2010).

Hounsfield, G. N. Computerized transverse axial scanning (tomography): Part 1. Description of system. *Br. J. Radiol*., **46**, 1016-1022 (1973).

Hu, G. *et al*. Imaging of Vx-2 rabbit tumors with αvβ3-integrin-targeted 111In nanoparticles. *Int. J. Cancer* **120**, 1951–1957 (2007).

Huynh, E. *et al*. Porphyrin shell microbubbles with intrinsic ultrasound and photoacoustic properties. *J. Am. Chem. Soc*. **134**, 16464–16467 (2012).

Jafari, S. *et al*. High-frequency (20 to 40 MHz) acoustic response of liquid-filled nanocapsules. *IEEE Trans. Ultrason. Ferroelectr. Freq. Control* **61**, 5–15 (2014).

Jain, P. K., Lee, K. S., El-Sayed, I. H. & El-Sayed, M. A. Calculated absorption and scattering properties of gold nanoparticles of different size, shape, and composition: applications in biological imaging and biomedicine. *J. Phys. Chem*. B **110**, 7238–7248 (2006).

Kaneda, M. M., Caruthers, S., Lanza, G. M. & Wickline, S. A. Perfluorocarbon nanoemulsions for quantitative molecular imaging and targeted therapeutics. *Ann. Biomed. Eng*. **37**, 1922–1933 (2009).

Kang, S.-T. & Yeh, C.-K. Intracellular acoustic droplet vaporization in a single peritoneal macrophage for drug delivery applications. *Langmuir* **27**, 13183–13188 (2011).

Kim, J.-W., Galanzha, E. I., Shashkov, E. V., Moon, H.-M. & Zharov, V. P. Golden carbon nanotubes as multimodal photoacoustic and photothermal high-contrast molecular agents. *Nat. Nanotechnol*. **4**, 688–694 (2009).

Klibanov, A. L. *et al*. Targeting of ultrasound contrast material: selective imaging of microbubbles in vitro. *Academic Radiology*. **5**, S243-S246 (1998).

Klibanov, A. L. Preparation of targeted microbubbles: ultrasound contrast agents for molecular imaging. *Med. Biol. Eng. Comput*. **47**, 875–882 (2009).

Kripfgans, O. D., Fowlkes, J. B., Miller, D. L., Eldevik, O. P. & Carson, P. L. Acoustic droplet vaporization for therapeutic and diagnostic applications. *Ultrasound Med. Biol*. **26**, 1177–1189 (2000).

Kripfgans, O. D., Fowlkes, J. B., Woydt, M., Eldevik, O. P. & Carson, P. L. In vivo droplet vaporization for occlusion therapy and phase aberration correction. *IEEE Trans. Ultrason. Ferroelectr. Freq. Control* **49**, 726–738 (2002).

Kripfgans, O. D., Miller, D. L., Fowlkes, J. B. & Carson, P. L. Vaporization of micrometer size droplets in simulated in vivo environments. *J. Acoust. Soc. Am*. **106**, 2191–2191 (1999).

Ku, G. *et al*. Copper sulfide nanoparticles as a new class of photoacoustic contrast agent for deep tissue imaging at 1064 nm. *ACS Nano* **6**, 7489–7496 (2012).

Lajoinie, G. *et al*. Ultrafast vapourization dynamics of laser-activated polymeric microcapsules. *Nat. Commun*. **5**, (2014).

Landsman, M. L., Kwant, G., Mook, G. A., & Zijlstra, W. G. Light-absorbing properties, stability, and spectral stabilization of indocyanine green. *J. Appl. Physiol*. **40**, 575–583 (1976).

Lankford, M. *et al*. Effect of microbubble ligation to cells on ultrasound signal enhancement: implications for targeted imaging. *Invest. Radiol*. **41**, 721–728 (2006).

Lanza, G. M. *et al*. A novel site-targeted ultrasonic contrast agent with broad biomedical application. *Circulation* **94**, 3334–3340 (1996).

Lanza, G. M. *et al*. Targeted antiproliferative drug delivery to vascular smooth muscle cells with a magnetic resonance imaging nanoparticle contrast agent implications for rational therapy of restenosis. *Circulation* **106**, 2842–2847 (2002).

Lattin, J. R., Belnap, D. M. & Pitt, W. G. Formation of eLiposomes as a drug delivery vehicle. *Colloids Surf. B Biointerfaces* **89**, 93–100 (2012).

Lawrence, A. J. Palpating breast cancer by magnetic resonance elastography. *Proc. ISMRM* (1999).

Lentacker, I., De Smedt, S. C. & Sanders, N. N. Drug loaded microbubble design for ultrasound triggered delivery. *Soft Matter* **5**, 2161–2170 (2009).

Leong-Poi, H. *et al*. Influence of microbubble shell properties on ultrasound signal: implications for low-power perfusion imaging. *J. Am. Soc. Echocardiogr*. **15**, 1269–1276 (2002).

Letokhov, V. S., & Zharov, V. P. Laser optoacoustic spectroscopy. *Springer Ser. Opt. Sci* **37** (1986).

Liang, H.-D., Tang, J. & Halliwell, M. Sonoporation, drug delivery, and gene therapy. *Proc. Inst. Mech. Eng. [H]* **224**, 343–361 (2010).

Lin, C.-Y. & Pitt, W. G. Acoustic droplet vaporization in biology and medicine. *BioMed Res. Int*. 2013, e404361 (2013).

Lindner, J. R. *et al*. Ultrasound assessment of inflammation and renal tissue injury with microbubbles targeted to p-selectin. *Circulation* **104**, 2107–2112 (2001).

Lo, A. H., Kripfgans, O. D., Carson, P. L., Rothman, E. D. & Fowlkes, J. B. Acoustic droplet vaporization threshold: effects of pulse duration and contrast agent. *IEEE Trans. Ultrason. Ferroelectr. Freq. Control* **54**, 933–946 (2007).

Luke, G. P. *et al*. Silica-coated gold nanoplates as stable photoacoustic contrast agents for sentinel lymph node imaging. *Nanotechnology* **24**, 455101 (2013).

Luke, G. P., Myers, J. N., Emelianov, S. Y. & Sokolov, K. V. Sentinel lymph node biopsy revisited: ultrasound-guided photoacoustic detection of micrometastases using molecularly targeted plasmonic nanosensors. *Cancer Res*. **74**, 5397-5408 (2014).

Luke, G. P., Yeager, D. & Emelianov, S. Y. Biomedical applications of photoacoustic imaging with exogenous contrast agents. *Ann. Biomed. Eng*. **40**, 422–437 (2012).

Magnetto, C. *et al*. Ultrasound-activated decafluoropentane-cored and chitosan-shelled nanodroplets for oxygen delivery to hypoxic cutaneous tissues. *RSC Adv*. **4**, 38433–38441 (2014).

Mallidi, S. *et al*. Multiwavelength photoacoustic imaging and plasmon resonance coupling of gold nanoparticles for selective detection of cancer. *Nano Lett*. **9**, 2825–2831 (2009).

Mandelis, A. Principles and perspectives of photothermal and photoacoustic phenomena. *Elsevier* (1992).

Marsh, J. N. *et al*. Improvements in the ultrasonic contrast of targeted perfluorocarbon nanoparticles using an acoustic transmission line model. *IEEE Trans. Ultrason. Ferroelectr. Freq. Control* **49**, 29–38 (2002).

Marsh, J. N. *et al*. Molecular imaging with targeted perfluorocarbon nanoparticles: quantification of the concentration dependence of contrast enhancement for binding to sparse cellular epitopes. *Ultrasound Med. Biol*. **33**, 950–958 (2007).

Martz, T. D., Bardin, D., Sheeran, P. S., Lee, A. P. & Dayton, P. A. Microfluidic generation of acoustically active nanodroplets. *Small* **8**, 1876–1879 (2012).

Martz, T. D., Sheeran, P. S., Bardin, D., Lee, A. P. & Dayton, P. A. Precision manufacture of phase-change perfluorocarbon droplets using microfluidics. *Ultrasound Med. Biol*. **37**, 1952–1957 (2011).

Mattrey, R. F. & Andre, M. P. Ultrasonic enhancement of myocardial infarction with perfluorocarbon compounds in dogs. *Am. J. Cardiol*. **54**, 206–210 (1984).

Mehrmohammadi, M., Oh, J., Mallidi, S. & Emelianov, S. Y. Pulsed magneto-motive ultrasound imaging using ultrasmall magnetic nanoprobes. *Mol. Imaging* **10**, 102–110 (2011).

Miller, D. L. *et al*. Bioeffects considerations for diagnostic ultrasound contrast agents. *J. Ultrasound Med*. **27**, 611–632 (2008).

Miller, D. L. Ultrasonic detection of resonant cavitation bubbles in a flow tube by their second-harmonic emissions. *Ultrasonics* **19**, 217–224 (1981).

Miller, D. L., Kripfgans, O. D., Fowlkes, J. B. & Carson, P. L. Cavitation nucleation agents for nonthermal ultrasound therapy. *J. Acoust. Soc. Am.* **107**, 3480–3486 (2000).

Miyazaki, M. & Kato, K. measurement of cerebral blood flow by ultrasonic Doppler technique : theory. *Jpn. Circ. J.* **29**, 375–382 (1965).

Moncion, A., Kripfgans, O. D., Carson, P. L., Fowlkes, J. B. & Fabiilli, M. L. Characterization of acoustic droplet vaporization and inertial cavitation thresholds in acoustically-responsive tissue scaffolds. *Ultrasonics Symposium (IUS), 2014 IEEE International* 1646–1649 (2014).

Mourant, J. R., Fuselier, T., Boyer, J., Johnson, T. M. & Bigio, I. J. Predictions and measurements of scattering and absorption over broad wavelength ranges in tissue phantoms. *Appl. Opt.* **36**, 949–957 (1997).

Myers, J. N., Holsinger, F. C., Jasser, S. A., Bekele, B. N. & Fidler, I. J. An orthotopic nude mouse model of oral tongue squamous cell carcinoma. *Clin. Cancer Res.* **8**, 293–298 (2002).

Naito, R. & Yokoyama, K. An improved perfluorodecalin emulsion. Pr*og. Clin. Biol. Res*. **19**, 81–89 (1978).

Needles, A. *et al*. Nonlinear contrast imaging with an array-based micro-ultrasound system. *Ultrasound Med. Biol*. **36**, 2097–2106 (2010).

Newman, P. G. & Rozycki, G. S. The history of ultrasound. *Surg. Clin. North Am.* **78**, 179–195 (1998).

Ntziachristos, V. & Razansky, D. Molecular imaging by means of multispectral optoacoustic tomography (MSOT). *Chem. Rev*. **110**, 2783–2794 (2010).

Nyborg, W. L. Safety of medical diagnostic ultrasound. *Semin. Ultrasound CT MRI* **23**, 377–386 (2002).

Oppelt, A. *Imaging Systems for Medical Diagnostics: Fundamentals, Technical Solutions and Applications for Systems Applying Ionizing Radiation, Nuclear Magnetic Resonance and Ultrasound*. John Wiley & Sons (2011).

Park, H. K., Kim, D., Grigoropoulos, C. P. & Tam, A. C. Pressure generation and measurement in the rapid vaporization of water on a pulsed-laser-heated surface. *J. Appl. Phys*. **80**, 4072–4081 (1996).

Parker, K. J., Huang, S. R., Musulin, R. A. & Lerner, R. M. Tissue response to mechanical vibrations for ‘sonoelasticity imaging’. *Ultrasound Med. Biol*. **16**, 241–246 (1990).

Patel, C. K. N. & Tam, A. C. Pulsed optoacoustic spectroscopy of condensed matter. *Rev. Mod. Phys*. **53**, 517–550 (1981).

Phelps, M. E. *et al*. Application of annihilation coincidence detection to transaxial reconstruction tomography. *J. Nucl. Med. Off. Publ. Soc. Nucl. Med*. **16**, 210–224 (1975).

Podell, S., Golec, B. & Lohrmann, R. Measuring the effects of ultrasound on contrast agents. *1999 IEEE Ultrasonics Symposium, 1999. Proceedings* **2**, 1749–1754 (1999).

Prabhakar, U. *et al*. Challenges and key considerations of the enhanced permeability and retention effect for nanomedicine drug delivery in oncology. *Cancer Res*. **73**, 2412–2417 (2013).

Prince, J. L. & Links, J. *Medical Imaging Signals and Systems*. Prentice Hall (2005).

Rabi, I. I. Space quantization in a gyrating magnetic field. *Phys. Rev*. **51**, 652–654 (1937).

Rabi, I. I., Millman, S., Kusch, P. & Zacharias, J. R. The molecular beam resonance method for measuring nuclear magnetic moments. The magnetic moments of Li63, Li73 and F199. *Phys. Rev*. **55**, 526–535 (1939).

Raisinghani, A. & DeMaria, A. N. Physical principles of microbubble ultrasound contrast agents. *Am. J. Cardiol*. **90**, 3–7 (2002).

Ramaswamy, S., Ross, K. N., Lander, E. S. & Golub, T. R. A molecular signature of metastasis in primary solid tumors. *Nat. Genet*. 33, **49**–54 (2003).

Rapoport, N. *et al*. Ultrasound-mediated tumor imaging and nanotherapy using drug loaded, block copolymer stabilized perfluorocarbon nanoemulsions. *J. Controlled Release* **153**, 4–15 (2011).

Rapoport, N. Y., Efros, A. L., Christensen, D. A., Kennedy, A. M. & Nam, K.-H. Microbubble generation in phase-shift nanoemulsions used as anticancer drug carriers. *Bubble Sci. Eng. Technol*. **1**, 31–39 (2009).

Rapoport, N. Y., Kennedy, A. M., Shea, J. E., Scaife, C. L. & Nam, K.-H. Controlled and targeted tumor chemotherapy by ultrasound-activated nanoemulsions/microbubbles. *J. Controlled Release* **138**, 268–276 (2009).

Rapoport, N., Gao, Z. & Kennedy, A. Multifunctional nanoparticles for combining ultrasonic tumor imaging and targeted chemotherapy. *J. Natl. Cancer Inst*. **99**, 1095–1106 (2007).

Reznik, N. *et al*. On the acoustic properties of vaporized submicron perfluorocarbon droplets. *Ultrasound Med. Biol*. **40**, 1379–1384 (2014).

Reznik, N. *et al*. The efficiency and stability of bubble formation by acoustic vaporization of submicron perfluorocarbon droplets. *Ultrasonics* **53**, 1368–1376 (2013).

Reznik, N., Williams, R. & Burns, P. N. Investigation of vaporized submicron perfluorocarbon droplets as an ultrasound contrast agent. *Ultrasound Med. Biol*. **37**, 1271–1279 (2011).

Riess, J. G. Perfluorocarbon-based oxygen delivery. *Artif. Cells Blood Substit. Biotechnol*. **34**, 567–580 (2006).

Riess, J. G. The design and development of improved fluorocarbon-based products for use in medicine and biology. *Artif. Cells Blood Substit. Biotechnol*. **22**, 215–234 (1994).

Rodriguez, V. B. *et al*. Encapsulation and stabilization of indocyanine green within poly(styrene-alt-maleic anhydride) block-poly(styrene) micelles for near-infrared imaging. *J. Biomed. Opt*. **13**, 014025-1–014025-10 (2008).

Röntgen, W. C. On a New Kind of Rays. *Science* **3**, 227–231 (1896).

Rosencwaig, A. & Gersho, A. Theory of the photoacoustic effect with solids. *J. Appl. Phys*. **47**, 64–69 (1976).

Rosencwaig, A. *Photoacoustics and Photoacoustic Spectroscopy*. Wiley (1980).

Saha, K. *et al*. Surface creasing instability of soft polyacrylamide cell culture substrates. *Biophys. J*. **99**, L94–L96 (2010).

Sboros, V. Response of contrast agents to ultrasound. *Adv. Drug Deliv. Rev*. **60**, 1117–1136 (2008).

Schad, K. C. & Hynynen, K. In vitro characterization of perfluorocarbon droplets for focused ultrasound therapy. *Phys. Med. Biol*. **55**, 4933 (2010).

Senapati, N., Lele, P. P. & Woodin, A. A study of the scattering of sub-millimeter ultrasound from tissues and organs. *1972 Ultrasonics Symposium* 59–63 (1972).

Seo, M., Gorelikov, I., Williams, R. & Matsuura, N. Microfluidic assembly of monodisperse, nanoparticle-incorporated perfluorocarbon microbubbles for medical imaging and therapy. *Langmuir* **26**, 13855–13860 (2010).

Shashkov, E. V., Everts, M., Galanzha, E. I. & Zharov, V. P. Quantum dots as multimodal photoacoustic and photothermal contrast agents. *Nano Lett*. **8**, 3953–3958 (2008).

Sheeran, P. S., Luois, S. H., Mullin, L. B., Matsunaga, T. O. & Dayton, P. A. Design of ultrasonically-activatable nanoparticles using low boiling point perfluorocarbons. *Biomaterials* **33**, 3262–3269 (2012).

Sheeran, P. S., Luois, S., Dayton, P. A. & Matsunaga, T. O. Formulation and acoustic studies of a new phase-shift agent for diagnostic and therapeutic ultrasound. *Langmuir* **27**, 10412–10420 (2011).

Shpak, O. *et al*. Acoustic droplet vaporization is initiated by superharmonic focusing. *Proc. Natl. Acad. Sci*. **111**, 1697–1702 (2014).

Siegel, R., Naishadham, D. & Jemal, A. Cancer statistics, 2013. *CA. Cancer J. Clin*. **63**, 11–30 (2013).

Sigrist, M. W. Laser generation of acoustic waves in liquids and gases. *J. Appl. Phys*. **60**, R83–R122 (1986).

Simons, J. M. M. *et al*. Monodisperse perfluorohexane emulsions for targeted ultrasound contrast imaging. *J. Mater. Chem*. **20**, 3918 (2010).

Simpson, D. H., Chin, C. T. & Burns, P. N. Pulse inversion Doppler: a new method for detecting nonlinear echoes from microbubble contrast agents. *IEEE Trans. Ultrason. Ferroelectr. Freq. Control* **46**, 372–382 (1999).

Singh, V. R. "Safety standards for medical ultrasound systems." *World Congress on Medical Physics and Biomedical Engineering 2006*. Springer Berlin Heidelberg (2007).

Stakutis, V. J., Morse, R. W., Dill, M. & Beyer, R. T. Attenuation of ultrasound in aqueous suspensions. *J. Acoust. Soc. Am*. **27**, 539–546 (1955).

Strohm, E. M., Rui, M., Kolios, M. C., Gorelikov, I. & Matsuura, N. Optical droplet vaporization (ODV): photoacoustic characterization of perfluorocarbon droplets. *2010 IEEE Ultrasonics Symposium (IUS)* 495–498 (2010).

Strohm, E., Rui, M., Gorelikov, I., Matsuura, N. & Kolios, M. Vaporization of perfluorocarbon droplets using optical irradiation. *Biomed. Opt. Express* **2**, 1432–1442 (2011).

Sukhorukov, G. B. *et al*. Nanoengineered polymer capsules: tools for detection, controlled delivery, and site-specific manipulation. *Small* **1**, 194–200 (2005).

Szabo, T. L. *Diagnostic Ultrasound Imaging: Inside Out*. Academic Press (2004).

Takalkar, A. M., Klibanov, A. L., Rychak, J. J., Lindner, J. R. & Ley, K. Binding and detachment dynamics of microbubbles targeted to P-selectin under controlled shear flow. *J. Controlled Release* **96**, 473–482 (2004).

Tam, A. C. Applications of photoacoustic sensing techniques. *Rev. Mod. Phys*. **58**, 381–431 (1986).

Tan, Y. C. & Lee, A. P. Microfluidic separation of satellite droplets as the basis of a monodispersed micron and submicron emulsification system. *Lab on a Chip* **5**, 1178–1183 (2005).

Uhlendorf, V. & Hoffmann, C. Nonlinear acoustical response of coated microbubbles in diagnostic ultrasound. *1994 IEEE Ultrasonics Symposium, 1994. Proceedings* **3**, 1559–1562 (1994).

Vallebona, A. & Maragliano, V. Radiography with great enlargement (microradiography) and a technical method for the radiographic dissociation of the shadow. *Radiology* **17,** 2 (1931).

Villanueva, F. S. *et al*. Microbubbles targeted to intercellular adhesion molecule-1 bind to activated coronary artery endothelial cells. *Circulation* **98**, 1–5 (1998).

Vogel, A., Busch, S. & Parlitz, U. Shock wave emission and cavitation bubble generation by picosecond and nanosecond optical breakdown in water. *J. Acoust. Soc. Am*. **100**, 148–165 (1996).

Wang, L. V. & Hu, S. Photoacoustic tomography: in vivo imaging from organelles to organs. *Science* **335**, 1458–1462 (2012).

Waters, E. A. *et al*. Detection of targeted perfluorocarbon nanoparticle binding using 19F diffusion weighted MR spectroscopy. *Magn. Reson. Med*. **60**, 1232–1236 (2008).

Webb, A. & Kagadis, G. C. Introduction to biomedical imaging. *Med. Phys*. **30**, 2267 (2003).

Weers, J. G. & Arlauskas, R. A. Particle size analysis of perfluorocarbon emulsions in a complex whole blood matrix by sedimentation field-flow fractionation. *Colloids Surf. B Biointerfaces* **33**, 265–269 (2004).

West, G. A., Barrett, J. J., Siebert, D. R. & Reddy, K. V. Photoacoustic spectroscopy. *Rev. Sci. Instrum*. **54**, 797–817 (1983).

Wickramasinghe, H. K., Bray, R. C., Jipson, V., Quate, C. F. & Salcedo, J. R. Photoacoustics on a microscopic scale. *Appl. Phys. Lett*. **33**, 923–925 (1978).

Willmann, J. K. *et al*. US imaging of tumor angiogenesis with microbubbles targeted to vascular endothelial growth factor receptor type 2 in mice. *Radiology* **246**, 508–518 (2008).

Wilson, K., Homan, K. & Emelianov, S. Biomedical photoacoustics beyond thermal expansion using triggered nanodroplet vaporization for contrast-enhanced imaging. *Nat. Commun*. **3**, 618 (2012).

Xu, X., Wang, R. K., Elder, J. B. & Tuchin, V. V. Effect of dextran-induced changes in refractive index and aggregation on optical properties of whole blood. *Phys. Med. Biol*. **48**, 1205 (2003).

Yang, X., Stein, E. W., Ashkenazi, S. & Wang, L. V. Nanoparticles for photoacoustic imaging. *Wiley Interdiscip. Rev. Nanomed. Nanobiotechnol*. **1**, 360–368 (2009).

Sang, Y. Y. *et al*. A microfluidic technique for generating monodisperse submicron drops. *RSC Adv*. **3**, 2330–2335 (2013).

Yeung, T. *et al*. Effects of substrate stiffness on cell morphology, cytoskeletal structure, and adhesion. *Cell Motil. Cytoskeleton* **60**, 24–34 (2005).

Yokoyama, K. *et al*. Preparation of perfluorodecalin emulsion, an approach to the red cells substitute. *Fed. Proc*. **34**, 1478–1483 (1975).

Yoshizawa, S. *et al*. High intensity focused ultrasound lithotripsy with cavitating microbubbles. *Med. Biol. Eng. Comput*. **47**, 851–860 (2009).

Zhang, P. & Porter, T. An in vitro study of a phase-shift nanoemulsion: a potential nucleation agent for bubble-enhanced HIFU tumor ablation. *Ultrasound Med. Biol*. **36**, 1856–1866 (2010).

Vita

Alexander (Alex) Hannah was born in 1986 in Alexandria, Virginia to Charlotte and James Hannah. He grew up in Dayton, Ohio and attended Alter High School in Kettering. Alex attended Vanderbilt University in Nashville, where he received a B.E. in Biomedical Engineering. During this time, he studied instrumentation and nanomaterials for biomedical applications. Alex earned his M.S. in Biomedical Engineering and conducted his PhD research at The University of Texas at Austin, where he developed nanoparticle contrast agents for ultrasound and photoacoustic imaging. His work is published in *ACS Nano* and *Biomedical Optics Express*. In 2014 Alex studied at the Erasmus Medical Center in Rotterdam, Netherlands, as part of the Whitaker International Fellowship. After graduation, Alex plans to continue in biomedical research either through a postdoctoral fellowship or in an industrial setting.

Permanent email: ahannah95@gmail.com

This dissertation was typed by Alexander Hannah.